The operation, stability analysis and active damping of multi-port converter-based DC traction power systems

Yu, Haoyuan

DOI (link to publication from Publisher):
10.54337/aau695988791

Publication date:
2023

Document Version
Publisher's PDF, also known as Version of record

THE OPERATION, STABILITY ANALYSIS AND ACTIVE DAMPING OF MULTI-PORT CONVERTER-BASED DC TRACTION POWER SYSTEMS

BY
HAOYUAN YU

DISSERTATION SUBMITTED 2023

AALBORG UNIVERSITY
DENMARK

THE OPERATION, STABILITY ANALYSIS AND ACTIVE DAMPING OF MULTI-PORT CONVERTER-BASED DC TRACTION POWER SYSTEMS

by

Haoyuan Yu

AALBORG UNIVERSITY
DENMARK

Dissertation submitted

.

Dissertation submitted: December 2023

PhD supervisor: Professor Zhe Chen
Aalborg University

Assistant PhD supervisor: Associate Professor Yanbo Wang
Aalborg University

PhD committee: Associate Professor Sanjay Kumar Chaudhary (chair)
Aalborg University, Denmark

Professor Antonio. J. Marques Cardoso
University of Beira Interior, Portugal

Professor Hasan Komurcugil
Eastern Mediterranean University, Turkey

PhD Series: Faculty of Engineering and Science, Aalborg University

Department: AAU Energy

ISSN (online): 2446-1636
ISBN (online): 978-87-7573-579-2

Published by:
Aalborg University Press
Kroghstræde 3
DK – 9220 Aalborg Ø
Phone: +45 99407140
aauf@forlag.aau.dk
forlag.aau.dk

Printed in Denmark by Stibo Complete, 2023

CV

Haoyuan Yu received B.Sc degree and M.Sc degree in Electrical Engineering at Southwest Jiaotong University, Chengdu, Sichuan, China, in 2016 and 2019. Since 2020, he has been working toward a PhD degree at Aalborg University, Aalborg, Denmark. From October to December 2022, he was a visiting PhD student in DC systems, Energy Conversion and Storage Group of the Department of Electrical Sustainable Energy, Delft University of Technology, Delft, Netherlands. His research interests include the stability analysis of power electronic-based systems, multi-port DC/DC converter and DC traction power supply systems.

ENGLISH SUMMARY

As the population continually grows in many countries, the demand for urban rail transportation such as railway, metro and tram are also increasing. It has intensely attracted attention to the energy consumption reduction of urban rail transit. Since most urban rail transits adopt DC traction power systems (DCTPS), renewable energy sources (RES) and energy storage systems (ESS) can easily access and improve energy saving. However, there are also some challenges to integrating the RESs into the DCTPS. 1) The RESs and ESS are easily subject to voltage fluctuation caused by frequent tractive and braking operations of trains. Thus, the way of connecting RES, ESS and DCTPS, and their operation strategies should be investigated. 2) The stability analysis is extremely important due to the high penetration of power electronics devices when RES and ESS are integrated into DCTPS. 3) A new damping control approach should be proposed to tackle the instability issue of the whole system. Therefore, the objectives of this thesis are to investigate the operation, stability analysis and oscillation suppression methods of DCTPS integrating RES and ESS.

To do this, analyzing current topologies and methods of DCTPS integrating RESs and ESS in state-of-the-art literature has been carried out. It is found that most RESs and ESS are allocated scattered along the rail line and the energy saving effect is limited. In this project, RESs and ESS are combined as a microgrid to integrate with DCTPS through a multi-port converter such as triple active bridge (TAB) converter. The operation strategies of the proposed system are analyzed considering the intermittent feature of RESs and the regenerative braking energy (RBE) of trains.

Furthermore, the stability of two-port DC/DC converter is widely investigated by small signal methods or nonlinear analysis methods. Also, various passive damping methods and active damping methods have been put forward to tackle instability issues. But the stability of multi-port converter is not explored. This thesis develops the extra element theorem to obtain the input and output impedance of TAB converter based on its small signal model. The impact of different types of loads, power-flowing directions and control strategies on the output impedance of TAB converter is also analyzed. Then, impedance-based methods are adopted to analyze the stability of the TAB converter-based system, especially when it connects with constant power loads (CPLs).

Finally, an active damping control is developed to reshape the output impedance of the TAB converter, thereby eliminating the oscillation problem. This active damping control contains four plans corresponding to four different positions of virtual impedance. The virtual impedance damping control is verified by simulation and laboratory platforms.

The main contributions of this thesis are: 1) Propose a new structure and operation strategies of DCTPS connecting with RESs and ESS through a TAB converter. 2) The extra element theorem is used for deriving the terminal impedance of the TAB converter. The impedance-based method is used to explore the stability of the TAB converter-based system. 3) A new active damping control is developed to tackle the potential oscillation of the TAB converter with CPLs. Overall, the results of this thesis provide a promising insight into the solution of impedance derivation and active damping control of the multi-port converter-based systems.

DANSK RESUME

Da befolkningen fortsat vokser i mange lande, stiger efterspørgslen efter bybane-transport som jernbane, metro og sporvogn også. Dette har intensivt fokuseret på at reducere energiforbruget inden for bybane-transport. Da de fleste bybane-transportsystemer anvender DC-trækkraftsystemer (DCTPS), kan vedvarende energikilder (RES) og energilagringsystemer (ESS) nemt tilgås og forbedre energibesparelsen. Dog er der også udfordringer ved at integrere RES'er i DCTPS. 1) RES'er og ESS er følsomme over for spændingsudsving forårsaget af hyppige trækkrafts- og bremseoperationer på tog. Derfor bør metoden til at forbinde RES, ESS og DCTPS samt deres driftsstrategier undersøges. 2) Stabilitetsanalysen er ekstremt vigtig på grund af den høje brug af strømelektronik-enheder, når RES og ESS integreres i DCTPS. 3) Der bør foreslås en ny dæmpningskontroltilgang for at tackle stabilitetsproblemet i hele systemet. Derfor er målene med denne afhandling at undersøge driften, stabilitetsanalysen og metoderne til at undertrykke svingninger i DCTPS, der integrerer RES og ESS.

For at gøre dette er der blevet foretaget en analyse af aktuelle topologier og metoder til DCTPS, der integrerer RES'er og ESS, i den nyeste litteratur. Det er blevet konstateret, at de fleste RES'er og ESS'er er placeret spredt langs jernbanen, og energibesparelseseffekten er begrænset. I dette projekt kombineres RES'er og ESS'er som et mikronet for at integrere med DCTPS gennem en flerportskonverter såsom triple active bridge (TAB) konverteren. Driftsstrategierne for det foreslåede system analyseres med henblik på de intermittente egenskaber hos RES'er og den regenerative bremseenergi (RBE) fra togene.

Desuden undersøges stabiliteten af to-port DC/DC-konverteren bredt ved hjælp af små signalmetoder eller ikke-lineære analysemetoder. Der er også blevet fremsat forskellige passive dæmpningsmetoder og aktive dæmpningsmetoder for at tackle stabilitetsproblemer. Men stabiliteten af flerportskonverteren er kun lidt diskuteret. Denne afhandling udvikler den ekstra element-teorem for at opnå indgangs- og udgangsimpedanserne af TAB-konverteren baseret på dens small signal-model. Virkningen af forskellige typer belastninger, strømretninger og kontrolstrategier på udgangsimpedansen af TAB-konverteren analyseres også. Derefter vedtages impedansbaserede metoder til at analysere stabiliteten af systemet baseret på TAB-konverteren, især når det forbindes med konstanteffektbelastninger (CPLs).

Til sidst udvikles en aktiv dæmpningskontrol for at omforme udgangsimpedansen af TAB-konverteren og dermed eliminere svingningsproblemet. Denne aktive dæmpningskontrol indeholder fire planer, der svarer til fire forskellige positioner af virtuel impedans. Effektiviteten af dæmpningskontrollen med virtuel impedans bekræftes gennem simuleringer og laboratorieplatforme.

Hovedbidragene i denne afhandling er: 1) Forslag til en ny struktur og driftsstrategier for DCTPS, der er forbundet med RES'er og ESS gennem en TAB-konverter. 2) Ekstra element-teoremet anvendes til at udlede terminalimpedansen af TAB-konverteren. Impedansbaserede metoder anvendes til at analysere stabiliteten af systemet baseret på TAB-konverteren. 3) En ny aktiv dæmpningskontrol er udviklet for at håndtere potentiel svingning af TAB-konverteren med CPL'er. Samlet set giver resultaterne af denne afhandling en lovende indsigt i løsningen af stabilitetsanalyse og aktive dæmpningsmetoder for flerportskonverterbaserede systemer.

ACKNOWLEDGEMENTS

I would like to express my gratitude to my supervisors, Professor Zhe Chen and Associate Professor Yanbo Wang. During the three-year Ph.D. period, you have provided me with profound academic guidance and inspiration. Throughout the research process, you have consistently paid attention to my research progress, answered my questions, and guided me in overcoming numerous technical challenges. Without your dedicated guidance and selfless assistance, I would not have been able to complete this thesis.

In addition, I would also like to thank my colleagues, Dr. Wenbin Yuan, Dr. Qi Zhang, Hanwen Zhang, Xing Wei, Zhaoxin Wang, Xuewei Wu, Dr. Kaiqi Ma, Dr. Yi Zhang, and Dr. Zhongting Tang, as well as other colleagues at Aalborg University. Your assistance has made my research work progress more smoothly. Your expertise and work attitude have deeply inspired me.

Furthermore, I would like to express my gratitude to Assistant Professor Qin Zian and Professor Pavol Bauer from Delft University of Technology. I appreciate your assistance and guidance during my three-month overseas study period.

Lastly, I would like to express my gratitude to my parents, my brother and friends. You have consistently supported and encouraged me, allowing me to fully immerse myself in my research. You are the primary motivation to help me finish this three-year journey.

Haoyuan Yu

Aalborg University, December 01, 2023

TABLE OF CONTENTS

LIST OF ACRONYMS

AD	Active damping
DCTPS	DC traction power systems
RB	Regenerative braking
RBE	Regenerative braking energy
EET	Extra element theorem
PM	Phase margin
PV	Photovoltaics
RES	Renewable energy sources
DAB	Dual active bridge
TAB	Triple active bridge
TS	Traction substation

TABLE OF FIGURES

Part I. Report

CHAPTER 1. INTRODUCTION

As environmental problems become increasingly serious, carbon neutrality in energy and electricity field has attracted more and more attention. Renewable energy development is the most important way to achieve carbon neutrality. Take solar energy for instance, the worldwide installed solar energy capacity in 2018 was 483.01GW. By 2021, the worldwide installed solar energy capacity was increased to 843.09GW, where China had installed 306.40GW, the United States had installed 93.71GW and Denmark had installed 1.54GW [1]. For wind energy, The total worldwide installed wind energy capacity had reached 824.87GW [2]. Other renewable energy sources (RESs) such as biomass, hydrogen and geothermal energy have developed significantly.

There are many kinds of literature investigating design and management for RES-based power systems in which the loads mainly contain residential loads and industrial factories. However, special loads such as railway and metro are rarely discussed. Therefore, this dissertation is going to investigate the effect of RES on the DC traction power systems (DCTPS). A new DCTPS integrating RES and hydrogen station by multi-port DC/DC converter is proposed in this dissertation. The stability of multi-port DC/DC converter-based DCTPS is analyzed, and the corresponding active damping methods are developed.

1.1. TRADITIONAL DCTPS OF METRO OR SUBWAY

Fig. 1-1 shows the conventional structure of DCTPS of metro or subway. In general, there are two main power substations to step down the high 220kV or 110kV from the utility grid to a 35kV or 10kV network. The stations are distributed on this network. Each station has a step-down transformer to supply low-voltage AC loads such as lighting, air conditioners and elevators. Some stations have an additional traction transformer and a traction rectifier, called traction substation (TS), to converter the 35kV or 10kV network to a DC 750V or 1500V network.

The 24-pluse diode-based rectifier is widely applied in TS[3],[4]. Fig. 1-2 shows a 24-pluse rectifier in DCTPS. The 24-pluses rectifier is made from two parallel 12-pluse rectifiers and the phase-shifting angles of the diode rectifier1 (DR1), DR2, DR3 and DR4 are +22.5˚, -7.5˚, -22.5˚ and +7.5˚ [5],[6]. The disadvantage of the 24-pluses rectifier is that power is only allowed to be unidirectionally transferred. When trains are operating in the braking state, the regenerative braking energy (RBE) will be feedback to the 1500V DC network and cause the catenary voltage to increase dramatically. The RBE is a tremendous energy that cannot be ignored. For instance, the RBE accounts for 42% of total traction energy of urban rail train (BR 425) [7]. Therefore, how to utilize these RBE has attracted much attention in recent years.

1.2. THE UTILIZATION METHOD OF RBE IN DCTPS

1.2.1. OPERATING TIMETABLE OPTIMIZATION IN DCTPS

One solution to effectively utilizing the RBE is optimizing the train operation. It is also widely applied in railway transportation. It involves two stages: the optimization of train trajectory between successive stations, in which the train trajectory contains accelerating phase, cruising phase, coasting phase and braking phase as shown in Fig. 1-3. [8], [9], and the optimization of timetables of multi-trains among an entire line, which involves arrival time, departure time, dwelling time, trip time [10], [11].

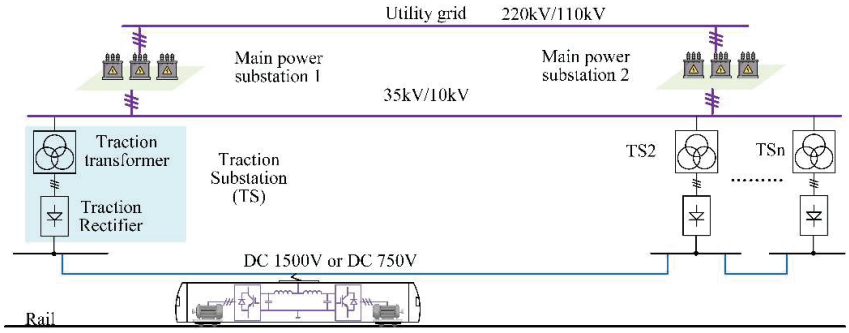

Figure 1-1 The simplified structure of conventional metro TPSS. [J1]

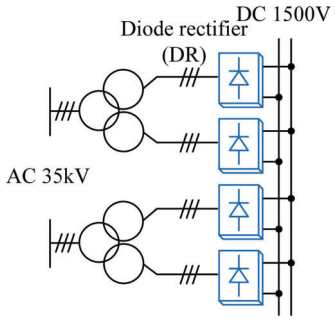

Figure 1-2 The 24-pluses traction rectifier for DC TPSS.

Various optimization methods have been applied to improve energy saving and enlarge economic benefits such as analytic methods [12], dynamic programming [13],[14], intelligent algorithms including genetic algorithms [15] and reinforcement learning approach [16]. However, the improvement of timetable optimization is limited since the RBE cannot be entirely reused by vicinity trains.

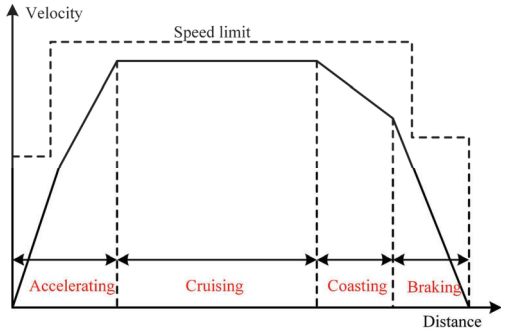

Figure 1-3 Train speed profile between two stations.

1.2.2. REGENERATIVE BRAKING UTILIZATION IN DCTPS BY GRID-FEEDBACK INVERTER

To utilize the RBE more efficiently, grid-feedback inverter is proposed and installed in TS. Fig. 1-4 shows the structure of feedback inverter in DCTPS. The grid-feedback inverter can convert the RBE from catenary to 35kV/10kV network or supply the 400VAC load in the station directly. If the capacity of the grid-feedback inverter is limited, the braking resistor is introduced to deplete the surplus RBE in the form of heat.

In [17], the RBE is converted to substation through a DC-DC chopper and a DC-AC inverter. It shows the grid-feedback inverter can save 8.7% of the substation consumption during the working day, 14.5% during Saturday and 24.25% during Sunday. In [18], the RBE is feedback to 35kV/10kV network through a two-level inverter and an isolation transformer, where a LC filter is added between the two devices. The impact of different startup voltage thresholds of grid-feedback inverter is analyzed and field test demonstrates the significant effect of saving the RBE by grid-feedback inverter. But, the parallel grid-feedback inverter has the potential issue of re-circuiting and brings harmonic problem for upstream AC network. In [19], an optimal control, based on indirect current control method, is proposed and the total harmonic distortion factor is below 2.5%. In addition, an inductance is added at the positive and negative pole of DC connection to avoid re-circulating in [17], and the total harmonic distortion is below 3%.

Furthermore, the system including the diode-based rectifier and the grid-feedback inverter can be substituted by a bidirectional converter. Although it is rarely applied in practical DCTPS, the research on the application of bidirectional converters mainly focuses on medium-voltage DC (MVDC) railways. In [20], the concept of voltage-source converter (VSC) railway electrification system is proposed, where a multi-level converter replaces the traditional diode-based rectifier, converting 15kV AC network to 20-30kV DC network. And a hierarchical control is proposed in [20],

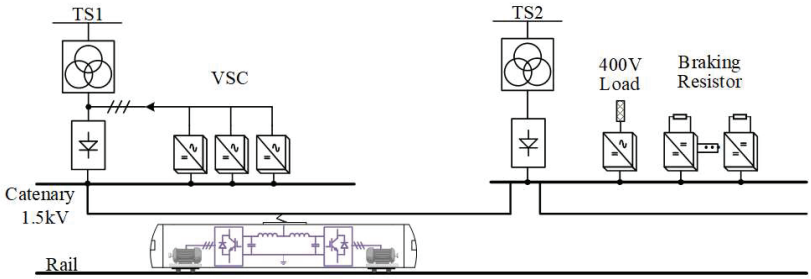

Figure 1-4 The application of grid-feedback inverter in TPSS. [J1],[J2]

where the first layer adopts droop control and the secondary central controller regulates the power management among VSC converters. However, the determination of the droop factor and design of the secondary central controller is not mentioned. In [21], an improved droop control strategy for VSC-based MVDC railway TPSS is proposed. The load current feedforward is added to droop control to improve the effect of DC side fluctuation on controller. In [23], the stability issue of VSC-based MVDC railway TPSS integrating photovoltaic (PV) generation system is analyzed based on their impedance model, and virtual impedance is added to the control loop to suppress the instability issue. In [23], the three-phase modular multilevel converter (MMC) connected in series with single-phase MMC constitutes the MVDC railway TPSS and an electrothermal behavioural model based on Wiener–Hammerstein configuration is presented for the real-time device-level simulation. However, unlike the diode-based rectifier, the application of VSC may increase the potential risk of outage due to the degradation of the semiconductor device.

1.2.3. REGENERATIVE BRAKING UTILIZATION IN DCTPS BY STORAGE DEVICE

Energy storage (ES) device, such as lithium-ion battery, supercapacitor and flywheel [46], is another solution to utilizing the RBE. There are two forms of the application of ES system (ESS) in DCTPS, on-board ESS and off-board ESS.

The on-board ESS is usually installed in the train, which can absorb the RBE when the train is in the braking operation, and the stored energy can be reused when the train starts up and accelerates. There are various types of power converters between ESS and traction system on the train. For example, a compact bidirectional buck-boost chopper is proposed in [24] for light rail vehicles, in which full bride cell connecting with auxiliary device is put closely to the inductor of the cascaded buck–boost inductor in the middle (CBB-IIM) converter [25]. In [26], the power converter for battery consists of a three-level bidirectional converter and a three- level neutral point clamped (NPC) converter. Other power converter prototypes, such as synchronous buck-boost converter [27], dual active bridge converter [28], and

capacitor-inductor-inductor-capacitor (CLLC) resonant converter [29] for train and electrical vehicles. If the rated voltage level lifts, an MMC converter is required for on-board ESS [30].

Furthermore, most work on the on-board ESS of trains is related to the optimization methods. In [31], the author uses mixed integer linear programming (MILP) to optimize the train speed trajectory with onboard ESS, in which the degradation of ESS is considered. Authors in [32] use dynamic programming to optimize the train speed trajectory. Their case study shows the train equipped with on-board ESS can save 14.2% of total energy consumption. Others use various optimization methods to determine the capacity of on-board ESS for train [33]-[35].

Compared with the on-board ESS, the off-board or wayside ESS, as shown in Fig. 1-5, mainly supplies these trains that running in nearby the traction substation. The off-board ESS can absorb the RBE from the braking train and supply the accelerating train in the vicinity. The converter topology of off-board ESS is consistent with on-board ESS. The research on the off-board ESS also mainly focuses on energy consumption reduction and sizing optimization. Authors in [36] establish a DC railway system model and use modified nodal analysis to compare the benefits of on-board ESS, off-board ESS and the traction substation equipped with a grid-feedback inverter. One case study shows that 19.1% of energy consumption is reduced when grid-feedback inverter is added, 29.4% of energy is saved by off-board ESS and 19.7% of energy is saved by on-board ESS. In [37], the model of metro traction equipped with off-board ESS is established and a tri-objective timetable optimization is solved by non-dominant sorting genetic algorithm (NSGA-II). It shows that energy efficiency is improved by 36.72%. In [38], a cooperative control-based multi-agent deep reinforcement learning is proposed to regulate the operation of supercapacitor-based off-board ESS, where the learning network mainly comprise a long short-term memory (LSTM) layer.

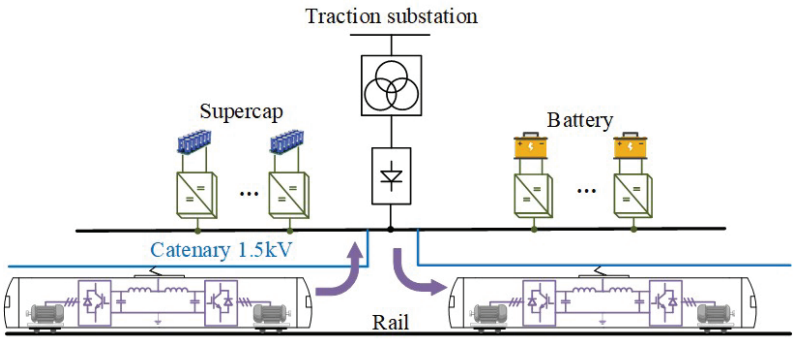

Figure 1-5 The application of ES device in DCTPS.

1.3. THE DCTPS INTEGRATING WITH RES AND HYDROGEN.

Although the application grid-feedback inverter, off-board and on-board is able to improve the RBE saving in DCTPS, the effect is limited due to their capacity. Incorporating renewable energy into DCTPS becomes a promising solution to further reduce energy consumption. For instance, PV panels are installed on the platform roof of Tokyo and Takasaki stations [39] to supply the loads such as lighting, and Li-ion batteries and PV panels are equipped at Hiraizumi station in Japan to achieve a "zero-emission" station [39][40]. The Shenzhen metro company in China established distributed PV system and ESS at stations, producing 2.7 million kWh per year [41].

However, the low voltage load cannot entirely consume the energy produced from RESs. In [42], the PV system and ESS are directly connected with 1500V catenary network. PV system is also integrated into the MVDC railway network [22]. The RESs and ESS are combined as a microgrid and connect with DC TPSS directly [43]-[45] or through a two-port bidirectional interlinking converter [47],[48] as shown in Fig. 1-6.

Apart from the above method for energy saving for urban rail transit, hydrogen (H_2)-driven trains are another promising solution. The investment cost is greatly reduced since the infrastructure of AC or DCTPS is not required [49], [50]. Intensive concerns have been given to investigate operation performance and energy management of H_2-driven train. For instance, in [51], a predictive power flow method is proposed to manage power flow between FC and flywheel ES system in H_2-driven train. The authors in [52] adopts the Lagrange algorithm to minimize hydrogen consumption and improve the braking recovery rate of hydrogen trams equipped with supercapacitors. They also design multimode equivalent energy consumption methods for different operations to improve online control [53]. In

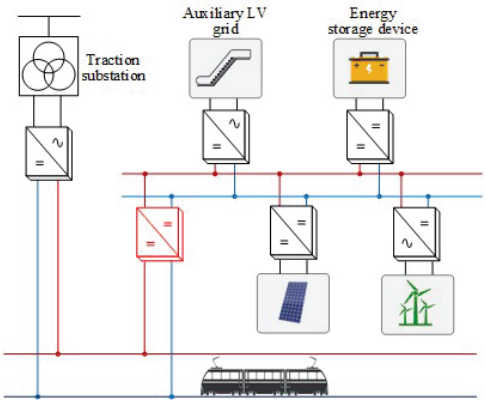

Figure 1-6 The DC microgrid in DCTPS. [J1]

addition, an adaptive droop control-based power management method is adopted to stabilize the DC bus voltage of the hybrid tramway including fuel cell, battery and supercapacitor [54]. However, the capacity of hydrogen tank can only support H_2-driven train for driving a short distance. It is inevitable to increase the volume of hydrogen tanks for long-distance driving or to be refueled at stations [55],[56].

There is a trend for the coexistence of H_2-driven train and traditional train in railway or metro systems in the future. In addition, the large railway station is also a transportation center, which contains bus stations and parking lots for electric and hydrogen vehicles. Therefore, this thesis proposed a multi-port DC/DC converter-based DCTPS, as shown in Figure 1-7, that integrates the renewable microgrid, DCTPS and hydrogen station by a triple active bridge (TAB) converter. The energy from RESs and regenerative braking trains can be better utilized for battery storage or hydrogen stations.

1.4. THE CHALLENGES IN THIS PROJECT

(1) The terminal impedance of multi-port DC/DC converter

With high penetration of power converter in DCTPS, stability is of significance to guarantee safe operation. The stability may exist at the point between catenary wire and the input side of traction inverter when train is in regenerative braking state [57], [58]. In [58], the oscillation is solved by changing the q-axis current reference to change the operation point to stable region.

There also exist instability issue when TS use bidirectional converter. The stability of cascaded converter systems including two-port DC/DC converter widely investigated in which the impedance-based method is especially frequently adopted.

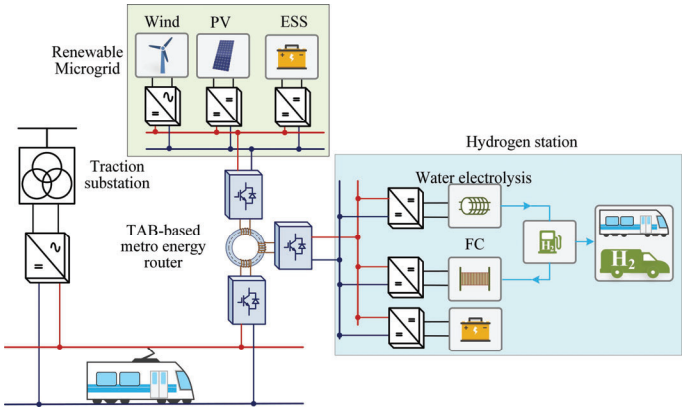

Figure 1-7 The structure of the TAB converter-based DCTPS. [C2]

The stability issue is evaluated by examining the terminal impedance ratio of source and load converter satisfies the Nyquist criterion at coupling points. In [59] and [60], it is used to investigate the stability of an input rectifier with a dual active bridge (DAB) converter. The stability of input filter with DAB converter is discussed in [61]. Besides the cascaded system, it is also applied to analysis of multiple DC systems connected by interlinking DC/DC converters [62]-[64]. In [62], the interlinking converter connects MVDC bus with LVDC bus, and the stability is determined by the equivalent gain loop associated with the output impedance of each converter.

Therefore, the impedance-based method requires an accurate input or output impedance. The feedback theorem [65] is presented for the derivation of input impedance of DAB converter in [59],[66]. However, it is complicated to obtain it in [66] due to the consideration of AC component in state-space model. In [67], different power-flowing directions are considered for the derivation of the output impedance of DAB converter.

There are two types of models of the TAB converter, the frequency domain model in [68] and the time domain model in [69], [70]. In [69],[70], the derivation of input impedance of TAB converter is based on the control block diagram. However, these derivations [68]-[70] are too complicated and the TAB converter usually acted as a source converter or a load converter in literature. Furthermore, when the TAB converter is interlinking, the terminal impedance would be extremely complicated. In [62]-[64], the interlinking converter is modelled as a two-port network [71]. The dimensions of the model would be increased when it comes to multi-port converter, which involves substantial computation. In addition, the effects of different power-flowing directions and loads on impedance are rarely investigated.

Thus, the derivation of terminal impedance of multi-port DC/DC converter is urgent to be solved.

(2) The active damping control of multi-port DC/DC converter

After the terminal impedance derivation and stability analysis, active damping (AD) controls should be researched to tackle the instability issue. Fig. 1-8 shows the impedance of cascaded two-stage systems. The objectives of AD controls are to separate the output impedance curves and input impedance curves or allow the phase margin of intersection section to large than zero degrees.

The virtual impedance is usually utilized to achieve the AD controls. In [72]-[74], the virtual impedance is presented in parallel or series for the load converter to modify the impedance. The AD controls can raise the input impedance of the load converter. Also, it is found in the applications of DAB converter [60], [61]or buck converter [75], [76].

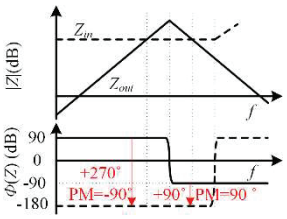

Figure 1-8 Impedance feature of cascaded converter systems. [J3]

The virtual impedance can also lower the output impedance of source converter. For instance, the droop coefficient utilized in droop control within DC systems can be perceived as the virtual impedance, which can effectively change the output impedance[77], [78]. In [79], the virtual impedance originally located at load converter side has been shifted to the source side. In [80], the DC microgrids is stabilized by a virtual RC damper. In addition to adding virtual impedance, the output impedance can be modified by adding a lead-lag controller [81], [82].

However, the active damping method for multi-port DC/DC converter, especially the TAB converter, is rarely investigated.

1.5. THE OBJECTIVES OF THIS THESIS

As the aforementioned challenges, the objectives in this project can be categorized as follows.

(1) The operation of TAB converter-based DCTPS

This thesis develops a TAB converter-based DCTPS as shown in Fig. 1-7. The system operation strategies will be developed considering the operation characteristics of each subsystem.

(2) The stability analysis method for TAB converter-based DCTPS

This thesis presents a general approach using the extra element theorem (EET) to get both the input and output impedance of TAB converters, considering different power-flowing directions and load types. Moreover, this approach can be applied to the multi-port active bridge converter.

(3) AD method for oscillation issue in TAB converter-based DCTPS

This thesis discovers that the oscillation issue exists when the TAB converter connects with CPLs. This thesis develops a virtual impedance control to tackle the oscillation problem, where the virtual impedance has four different placements at the output capacitor.

1.6. THE OUTLINE OF THIS THESIS

The thesis is elaborately written based on the publications in the process of Ph.D. project. It is presented as a collection of publications which contains two parts: report and selected publications. The outline of this thesis is illustrated in Fig. 1-9.

Chapter I is the introduction including background, motivation and objectives. Chapter II investigates the operation of DCTPS integrated RESs by a DAB converter. Based on this, the application of TAB converter in DCTPS integrated with RESs and hydrogen is investigated in Chapter III. In Chapter IV, the impedance derivation process of the TAB converter using EET is elaborated thoroughly. The stability of two CPLs in the TAB converter is explored. In Chapter V, the stability of one CPL is researched. Chapter VI exhibit a virtual impedance strategy to implement the active damping control, aiming to stabilize the TAB

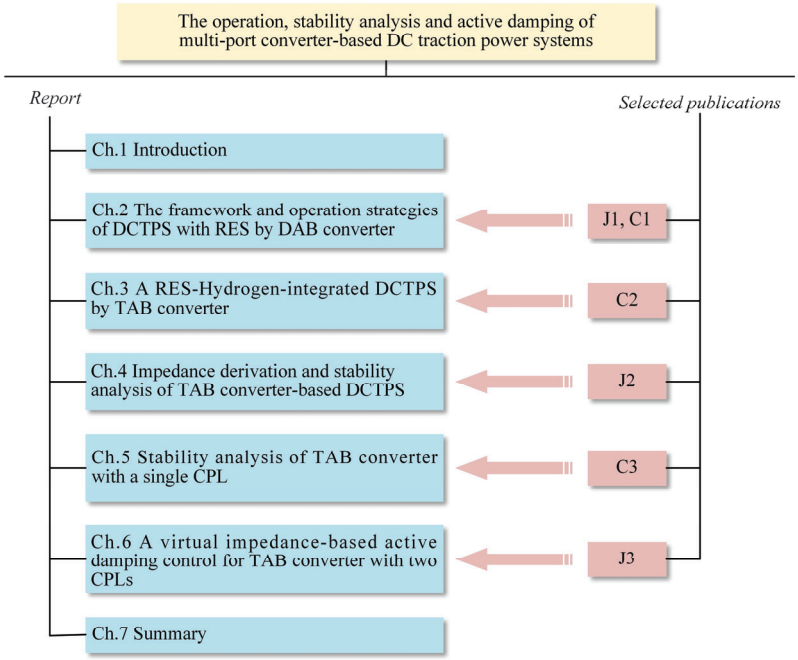

Figure 1-9 The outline of this thesis.

converter with two CPLs. The summary is given in Chapter VII.

1.7. LIST OF PUBLICATIONS

Journal papers

[J1]. **H. Yu**, Y. Wang and Z. Chen, "A Novel Renewable Microgrid-Enabled Metro Traction Power System—Concepts, Framework, and Operation Strategy," *IEEE Trans Transp. Electrific*., vol. 7, no. 3, pp. 1733-1749, Sept. 2021.

[J2]. **H. Yu**, Y. Wang, H. Zhang and Z. Chen, "Impedance Modeling and Stability Analysis of Triple Active Bridge Converter-Based Renewable-Electricity-Hydrogen-Integrated Metro DC Traction Power System," *IEEE Trans Ind. Electron.*, vol. 70, no. 12, pp. 12340-12353, Dec. 2023.

[J3]. **H. Yu**, H. Zhang, Q. Zhang, Y. Wang, Z. Qin, Z. Chen and P. Bauer, "A Virtual Impedance-based Active Damping Control Strategy for Triple Active Bridge Converter," IEEE Trans. Ind. Electron., 2023. (Under reviewing)

Conference papers

[C1]. **H. Yu**, Y. Wang and Z. Chen, "A Novel DC Microgrid-enabled Metro Traction Power System," in Proc. PEDG, 2020, Romania

[C2]. **H. Yu**, Y. Wang and Z. Chen, "A Renewable Electricity-Hydrogen-Integrated Hybrid DC Traction Power System," in Proc. SPEC, 2021, Rwanda

[C3]. **H. Yu**, H. Zhang, Y. Wang, Z. Qin, Z. Chen and P. Bauer, "Stability Analysis of Triple Active Bridge Converter with Hybrid Loads and Different Control Strategies," in Proc. PEDG, 2023, Shanghai.

CHAPTER 2. THE FRAMEWORK AND OPERATION STRATEGIES OF DCTPS WITH RES BY DAB CONVERTER

2.1. INTRODUCTION

Renewable energy access to urban traction power systems can significantly reduce the energy from power grid by supplying low voltage devices in stations or connecting DCTPS directly. However, the connection between RESs and DCTPS may face obstacles in guaranteeing the safe operation of power converter at RESs side, which is attributed to the huge voltage fluctuation [83], [84] caused by frequent tractive and braking operation of trains. In Section 2.2, DAB converters are used to connect RESs and DCTPS [J1], [C1]. The model of the system is established, and three operation strategies are presented to enable power management. In addition, H_2-driven trains are another trend for the future. The simulation is given for verification.

2.2. SYSTEM CONFIGURATION AND OPERATION MODES

A. System configuration

Fig. 2-1 illustrates the structure of DCTPS connected with renewable microgrid, where the DAB converter acts as an interlinking converter. The DAB converter is formed of two H-bridges and one high-frequency transformer. In addition, the renewable microgrid contains small-scale wind power system, PV generation system, ES system and EV charging station, and it connects to the primary side of DAB converter. The secondary side is connected with DCTPS. The renewable microgrid

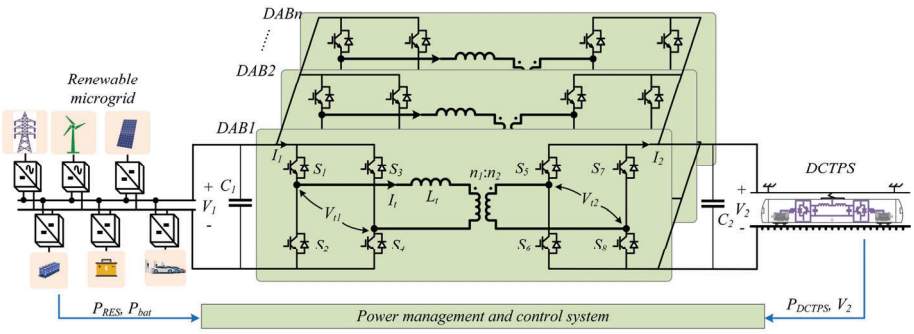

Figure 2-1 The proposed structure of DCTPS with RESs by DAB converter. [J1], [C1]

and DAB converter can be an independent TS or can be installed parallelly with traditional diode-based rectifiers in TS.

B. Operation modes

Three operation modes are proposed, which mainly concern the train traffic conditions in the power supply section. Fig. 2-2 shows the power relationship diagram depicting the three modes.

(1) Operation mode1: Voltage control mode

The operation mode1 is activated when many trains are running in the power supply section, especially in rush hour. Note that the power supply section in this thesis refers to the distance to left and right TS. The DAB adopts voltage control to regulate voltage of catenary or third rail, and the reference voltage value shall be greater than the output voltage of diode-based rectifier under no-load conditions. The DAB converter in this mode can either assist the rectifier to supply the tractive trains in the power supply section or absorb RBE to renewable microgrid.

(2) Operation mode2: Power control mode

The operation mode2 is enabled when a few trains are running in the section. Since the catenary voltage is dominated by diode-based rectifier, the DAB converter is able to regulate its output power or current. The positive value represents that the DAB converter is delivering the energy to DCTPS from renewable microgrid, and negative value represents the opposite power-flowing direction. When the DAB converters absorb energy in this mode, the detected catenary voltage should be higher than a threshold voltage which should be higher than 1500V. In this work, this mode is mainly used to support the tractive train in power supply section.

(3) Operation mode3: Islanded mode

The operation mode3 is activated when there is no trains in operation at night. The renewable microgrid is isolated with DCTPS due to the high-frequency transformer in DAB converter and can support the EV charging station and other loads at night. The power management and voltage regulation can be achieved by droop control [85], [86].

2.3. SYSTEM MODELLING AND CONTROL METHOD

In this section, the model and control of renewable microgrid, DAB converter and DCTPS are elaborated.

(1) The model and control method of DAB converter

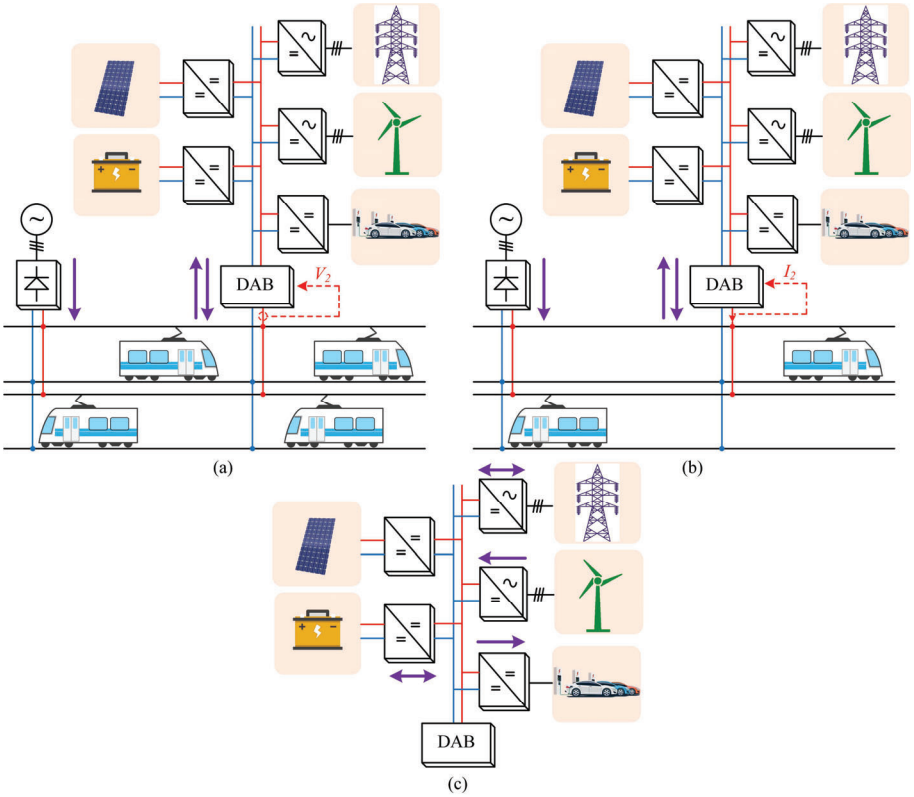

Figure 2-2 The general power relationship in different operation modes. (a) Operation mode1. (b) Operation mode2. (c) Operation mode3. [J1], [C1]

In this work, the magnetic inductance of transformer is omitted, only the leakage inductance is considered. The average power of the DAB converter can be given by (2.1) [87]-[89].

$$P_{DAB} = \frac{n_1 V_1 V_2}{2 n_2 f_s L_t} d\left(1 - |d|\right) \tag{2.1}$$

where the f_s represents the switching frequency. L_t represents the leakage inductance. d represents the phase shift ratio. The range of d is from -0.5 to 0.5 in which a positive phase difference represents that power is delivered to secondary side. A negative value represents the opposite direction of power-flowing.

As illustrated in Fig. 2-3(a), the model of DAB can be established as a two-port gyrator [90]. The DAB current can be given as (2.2)

$$I_1 = \frac{P_{DAB}}{V_1} = \frac{n_1 V_2}{2n_2 f_s L_t} d\left(1-|d|\right) = g_1 V_2, I_2 = \frac{P_{DAB}}{V_2} = \frac{n_1 V_1}{2n_2 f_s L_t} d\left(1-|d|\right) = g_2 V_1 \quad (2.2)$$

By linearization of (2.1) under a given steady operating point, the small signal model of DAB is able to be acquired and it is shown in Fig. 2-3(b). The output current relationship is represented as (2.3) and (2.4).

$$\hat{I}_2 = g_{21}\hat{d} + g_{22}\hat{V}_1 \quad (2.3)$$

$$g_{21} = \frac{\partial I_2}{\partial d} = \frac{n_1 V_1}{2n_2 f_s L_t}\left(1-2|d|\right),\ g_{22} = \frac{\partial I_2}{\partial V_1} = \frac{n_1 d_1}{2n_2 f_s L_t}\left(1-|d|\right) \quad (2.4)$$

Fig. 2-4 shows the control strategies of DAB for operation mode1 and mode2. For operation mode1, the output voltage (V_2) is regulated by a PI controller G_{v_DAB}. For operation mode2, the current reference value (I_{2_ref}) is determined by the train current (I_{train}). The coefficient α determines the power distribution between DAB converts and TS. The limiter is added at both operation modes, and a second-order low pass filter (LPF) is applied to filter out high-frequency parts of the output current. The parameters are given in Table 2-1.

(2) The model and control of renewable microgrid

The RESs in renewable microgrid is emulated by a synchronous boost-buck converter [91], which is illustrated in Fig. 2-5(a). The power generation of RESs can be simulated by controlling the inductance current. In addition, the ES system in renewable microgrids is shown in Fig. 2-5(b), where the battery is replaced by a voltage source and an internal resistor. The ES system is responsible for regulating

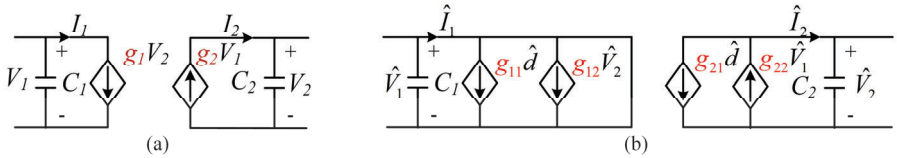

Figure 2-3 The DAB model. (a) gyrator model. (b) small signal model.[J1]

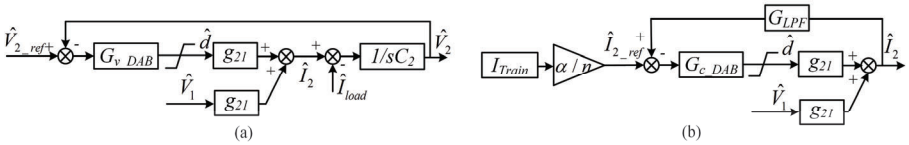

Figure 2-4 Control scheme of DAB converter. (a) voltage control for mode1. (b) current control for mode2.[J1]

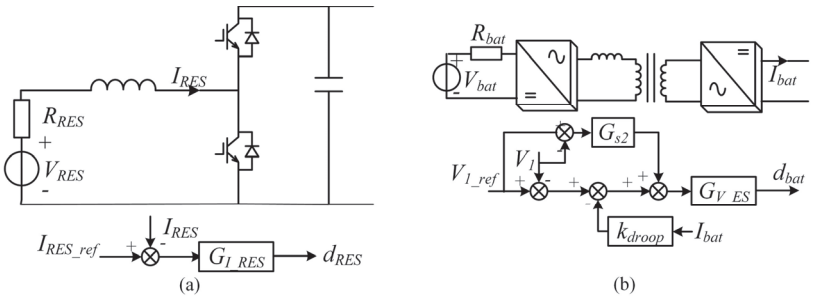

Figure 2-5 The model and control of renewable microgrid. (a) RESs. (b) ES system.[J1]

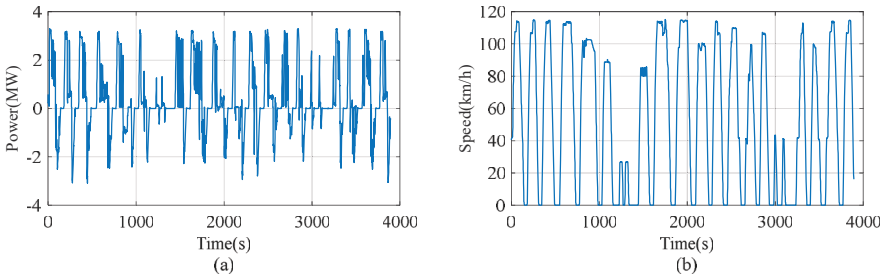

Figure 2-6 The measured power and speed profile of train. (a) Power. (b) Speed.[J1]

terminal voltage through voltage controller G_{V_ES}. The droop factor k_{droop} determines the power distribution among multiple ES devices and secondary regulator G_{s2} is added to eliminate the voltage deviation.

(3) The model of DCTPS

In this thesis, the train operation speed and demand power are obtained from the field test in the one of Guangzhou metro lines. Fig. 2-6 shows the measured train speed and power. The traction network of DCTPS is time-varying [92]. Fig. 2-7 shows the network of one section of DCTPS, where only one train is operating in this section. The traction substation (TS) is substituted by a voltage source connecting with a resistor and a diode. The blue and red lines represent the two directions of the power supply section and the resistor of network is associated with train position that can be given by (2.5).

$$\begin{cases} R_{c1} = \lambda z_1 \\ R_{c2} = \lambda (z - z_1) \\ R_{c3} = \lambda z \end{cases} \tag{2.5}$$

where λ denotes the unit impedance (Ω/km) of the catenary, z_1 denotes the distance from TS to the train, and z denotes the total distance.

2.4. SIMULATION CASES

The system parameters including renewable microgrid and DAB are given in Table 2-1. Four cases are investigated to verify the feasibility of the proposed system, which are shown as follows.

(1) Case one: Operation mode1 when DAB converters are cooperating with the traction substation.

In this case, the output voltage of DAB converters is set as 1520V to avoid the circle current with the diode-based rectifier. Fig. 2-8 shows the simulation results of case one in PLECS. The train is running in tractive status from 3s to 90s and running in

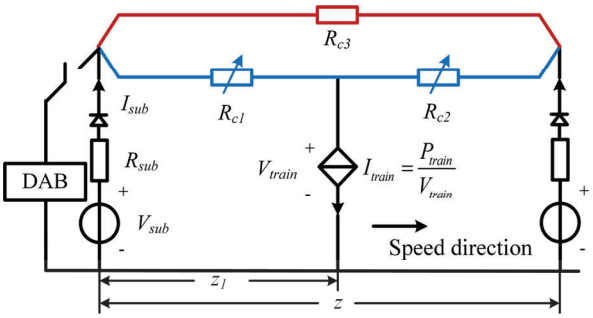

Figure 2-7 The traction network of DCTPS. [J1]

Table 2-1 The parameters of the system [J1]

System	Parameters	Value	Parameters	Value
DAB	L_t leakage inductance (μH)	40	C_1, C_2 Input and output capacitor (F)	1
	n_1:n_2 winding turns ratio	1:1	V_1, V_2 Input and output voltage (V)	1500
	f_s switching frequency (Hz)	10k	n number of parallel DAB converters	12
	ω_c speed of LPF (rad/s)	3.14e3	G_{LPF}: $\omega_c^2/(s^2+1.414\ \omega_c\ s+\ \omega_c^2)$	
	Voltage control G_{v_DAB}: 1.5e-4+0.0225/s		Current control G_{c_DAB}: 1.5e-4+0.0188/s	
RES	V_{bat} battery voltage (V)	395	R_{bat} battery internal resistance (Ω)	0.01
	Voltage control G_{V_ES} :1e-4+0.01/s		Current control G_{s2} :0.1+1/s	
	k_{droop1}: droop factor for ES1	1	k_{droop2}: droop factor for ES2	2
DCTPS	ρ catenary resistance (Ω/km)	0.0178	x distance (km)	2.851
	V_{sub} voltage of TS (V)	1500	R_{sub} internal resistance of TS (V)	0.01

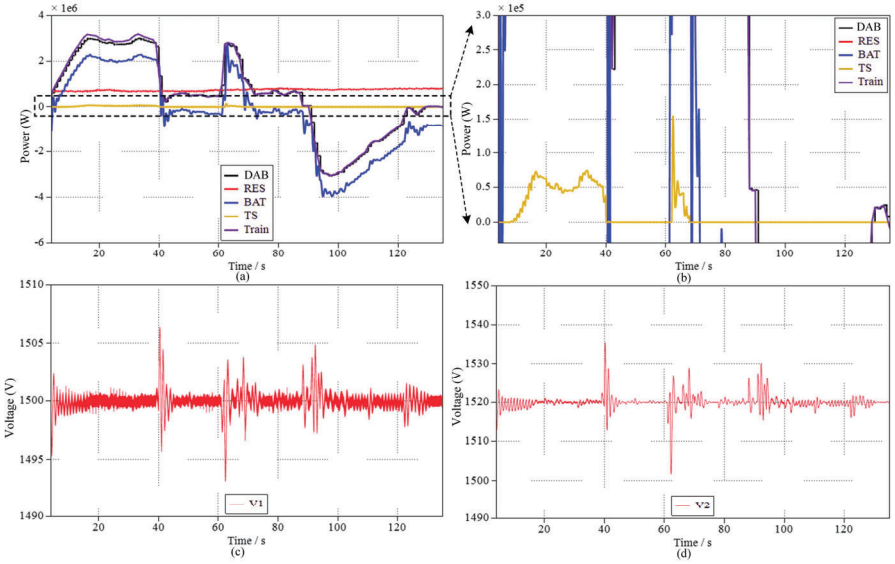

Figure 2-8 The simulation results of case one. (a) Power of each subsystem. (b) Power of TS. (c) voltage of renewable microgrid. (d) catenary voltage of DCTPS. [J1]

braking status from 91s to 135s.

It can be seen from Fig. 2-8(a) and (b) that DAB converters supply most of the energy required by DCTPS. The TS supplies a small portion of power for DCTP. When the power of RES is less than the tractive power of train, the ES system in renewable microgrids discharges to compensate for the power difference. When the train is braking, the ES will absorb the energy from RES and DCTPS.

Fig. 2-8(c) shows the bus voltage of renewable microgrids. It constantly varies during operation. The maximum voltage deviation is 7V which is in a reasonable region. Fig. 2-8(d) shows the catenary voltage of DCTS. Although the voltage fluctuates more serios than the voltage in renewable microgrids, it is still in the allowed range according to the standards [83], [84].

(2) Case two: Operation mode1 when DAB converters work independently.

In this case, the DAB converters and renewable microgrid are operating as an independent TS, and the output voltage V_2 of DAB converters is set as 1500V. Fig. 2-9 shows the simulation results of case two, where Fig. 2-9(a) shows the bus voltage of renewable microgrids, Fig. 2-9(b) shows the catenary voltage of DCTPS and Fig. 2-9(c) shows the power of the whole systems during operation. The DAB converters can provide the majority of energy for the train and others are supplied by TS on other side.

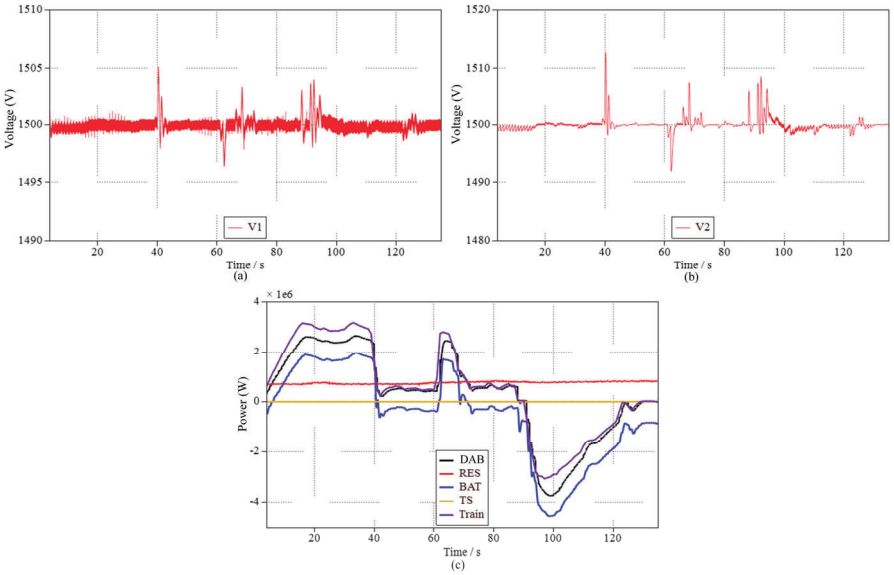

Figure 2-9 The simulation results of case two. (a) voltage of renewable microgrid. (b) voltage of DCTPS. (c) Power variation of each subsystem. [J1]

(3) Case three: Operation mode2

In this case, the DAB converters are installed in TS and adopt the current control to support DCTPS. The power distribution among DAB converters and TS is decided by coefficient α, which is shown in Fig. 2-4(b). Fig. 2-10 shows the simulation results when α are 0.7 and 0.4. It is obvious in Fig. 2-10(a1) and (b1) that the power of DAB converters decreases, and the power of TS increases when α is decreased to 0.4 from 0.7.

In addition, compared with the voltage waveform shown in Fig. 2-10(a3) and (b3), it indicates that the catenary voltage V_2 can remain at 1500V with a higher coefficient α. The voltage fluctuation of renewable microgrid, as shown in Fig. 2-10(a2) and (b2), is within 5% of the nominal voltage.

(4) Case four: Operation mode3

In this case, the DAB converters are out of work. The energy from RES and ES systems is consumed by loads such as EVs and lighting. The energy management of batteries in ES systems is achieved by droop control, where k_{droop1} is 1 and k_{droop2} is 2. Fig. 2-11 shows the simulation results of case four. It can be seen that the power of battery 1 is twice as battery 2 which corresponds to the ratio of droop factor k_{droop1} to k_{droop2}, which equals 0.5. The voltages of renewable microgrids shown in Fig. 2-11 can remain at 1500V.

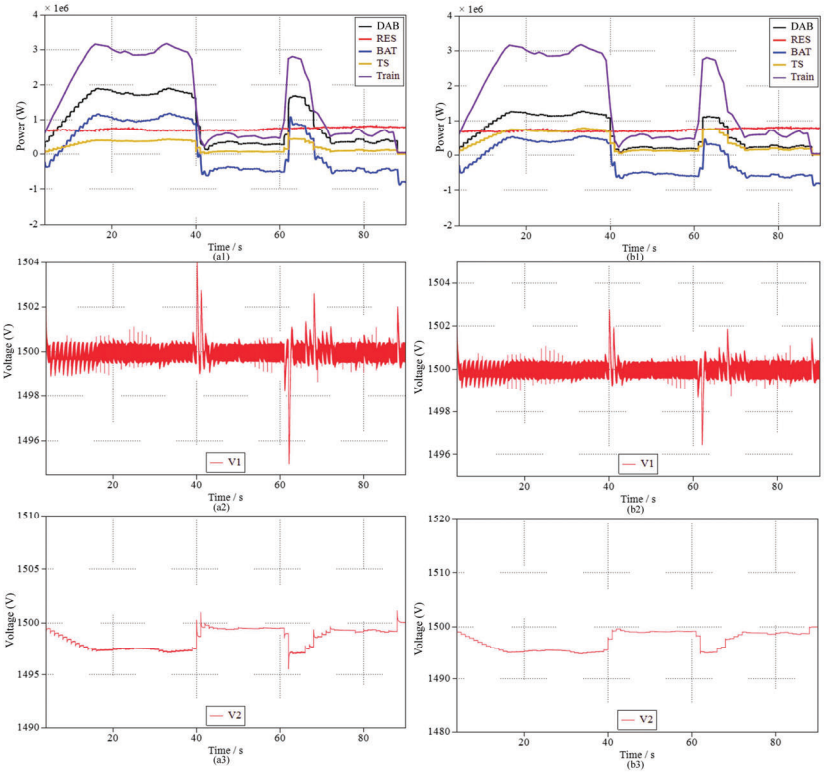

Figure 2-10 The simulation results of case three. (a1) power variation (α=0.7). (a2) V_1 (α=0.7). (a3) V_2 (α=0.7). (b1) power variation (α=0.4). (b2) V_1 (α=0.4). (b3) V_2 (α=0.4)

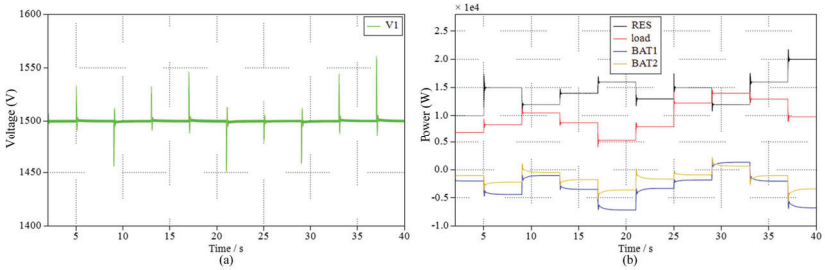

Figure 2-11 The simulation results of case four. (a) voltage waveform. (b) power variation.

2.5. CONCLUSION

In this Chapter, DAB converter is adopted as an interlinking converter to connect with DCTPS and RESs. Three operation strategies are proposed mainly based on the traffic and train operation states. The models of DCTPS, RES and DAB converter are elaborated in this Chapter, and simulation are carried out to demonstrate the effectiveness of the presented structure and operation strategies.

CHAPTER 3. A RES-HYDROGEN-INTEGRATED DCTPS BY TRIPLE ACTIVE BRIDGE CONVERTER

3.1. INTRODUCTION

In this Chapter, the TAB converter is an interlinking converter to integrate the DCTPS, RESs and a hydrogen station. The model of the TAB converter and hydrogen station is established and the control for each subsystem is presented. The simulation is given for verification.

3.2. SYSTEM DESCRIPTION AND OPERATION MODES

A. System description

Since hydrogen vehicles are a trend for energy conservation in transportation, the hydrogen station can be installed near the train station to refuel H_2_driven trains and cars. In this Section, a TAB converter is adopted to connect the renewable microgrid, DCTPS and the hydrogen station. Fig. 3-1 depicts the configuration of the proposed system. It is found that the port1 of TAB converter is interlinked with a renewable microgrid. The port2 of TAB converter is interlinked with DCTPS, and the hydrogen station connects to port3. In the hydrogen station, fuel cell (FC) connects with bus through a boost converter, and water electrolysis connects with bus through a buck converter.

B. Power-flowing relationship

The operation strategies of the TAB converter for DCTPS still obey the operation strategies proposed in previous Chapter 2. In this work, only power control mode is adopted for TAB converter to regulate DCTPS. Since TAB converter is extended from DAB converter, power-flowing directions are various. Four power-flowing directions are specified as follows, which are illustrated in Fig. 3-2.

The first is that power is delivered from the renewable microgrid to the hydrogen station when DCTPS is closed at night. The second is that power is delivered from the renewable microgrid to DCTPS and the hydrogen station when RES power is sufficient. The surplus energy can be employed to produce hydrogen. The third is that power flows from the renewable microgrid and the hydrogen station to DCTPS when RES power is insufficient, the FC in the hydrogen station starts to compensate

for the power difference. The fourth is that power flows from DCTPS to the renewable microgrid and the hydrogen station when DCTPS feedback the RBE.

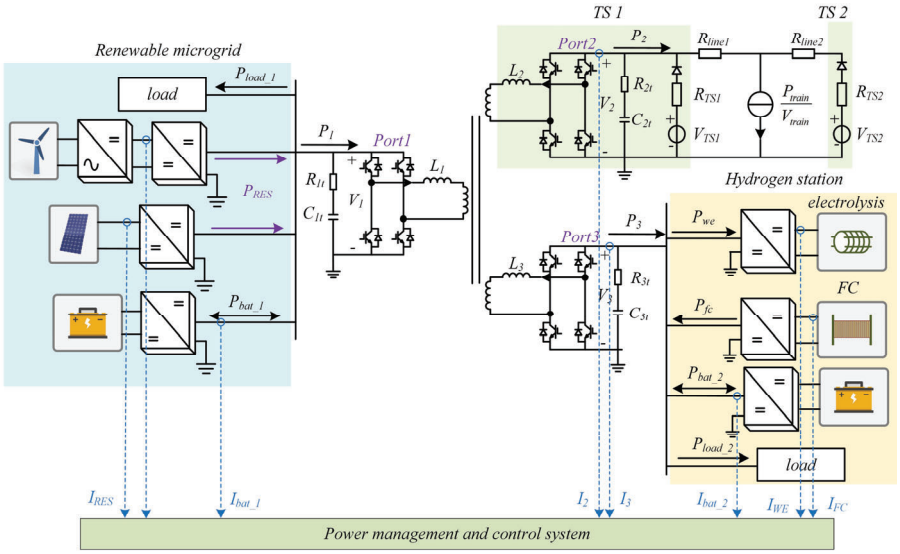

Figure 3-1 The simplified structure of renewable microgrid, DCTPS and hydrogen station integrating TAB converter. [C2]

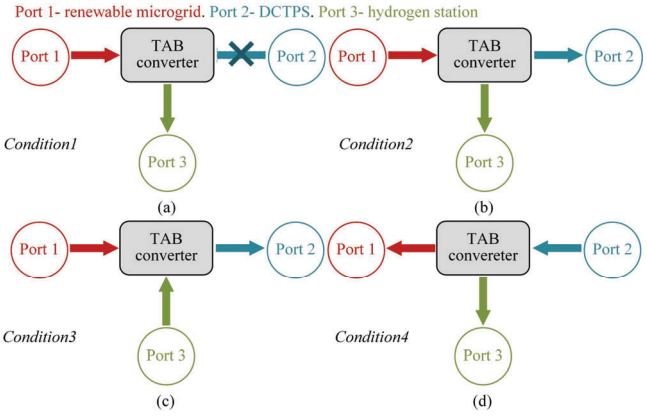

Figure 3-2 Power-flowing relationships of system. [C2]

3.3. SYSTEM MODELLING AND CONTROL METHOD

In this section, the model and control of the TAB converter and hydrogen station are elaborated, and the model of renewable microgrid and traction network is the same as in Chapter 2.

3.3.1. MODEL AND CONTROL OF TAB CONVERTER

In this work, the nominal bus voltage for port 1 and port 2 is set at 1500V, and the port3 voltage is established at 400V. Fig. 3-3(a) illustrates the Δ-connection type of TAB converter. Since the magnetization inductance is much greater than leakage inductance, only the leakage inductance is considered. The power between any two ports is given by (3.1)

$$\begin{cases} P_{12} = \dfrac{n_1 V_1 V_2}{2 n_2 f_s L_{12}} d_{12}\left(1-\left|d_{12}\right|\right) \\ P_{13} = \dfrac{n_1 V_1 V_3}{2 n_3 f_s L_{13}} d_{13}\left(1-\left|d_{13}\right|\right) \\ P_{23} = \dfrac{n_1^2 V_2 V_3}{2 n_2 n_3 f_s L_{23}}\left(d_{13}-d_{12}\right)\left(1-\left|d_{13}-d_{12}\right|\right) \end{cases} \tag{3.1}$$

where V_1, V_2 and V_3 are the bus voltages of each port. The d_{12} and d_{13} represents the phase shift ratio. f_s is the switching frequency. $L_{ij(i\neq j;i,j=1,2,3)}$ are the leakage inductances of equivalent Δ-connection transformers.

According to the superposition principle and power flowing direction shown in Fig. 3-3(a), The power of each power of TAB converter can be given as (3.2).

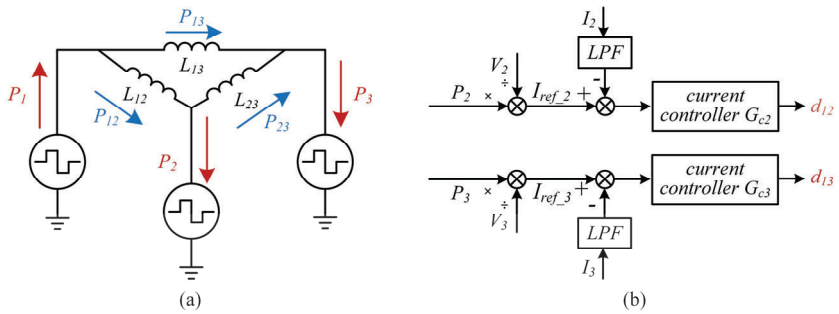

Figure 3-3 The equivalent model of transformer and control of TAB converter. (a) equivalent Δ-connection model of transformer. (b) control strategy of TAB converter. [C2]

$$\begin{cases} P_1 = P_{12} + P_{13} = \dfrac{n_1 V_1 V_2}{2 n_2 f_s L_{12}} d_{12}\left(1-\left|d_{12}\right|\right) + \dfrac{n_1 V_1 V_3}{2 n_3 f_s L_{13}} d_{13}\left(1-\left|d_{13}\right|\right) \\ P_2 = P_{12} - P_{23} = \dfrac{n_1 V_1 V_2}{2 n_2 f_s L_{12}} d_{12}\left(1-\left|d_{12}\right|\right) - \dfrac{n_1^2 V_2 V_3}{2 n_2 n_3 f_s L_{23}}\left(d_{13}-d_{12}\right)\left(1-\left|d_{13}-d_{12}\right|\right) \\ P_3 = P_{13} + P_{23} = \dfrac{n_1 V_1 V_3}{2 n_3 f_s L_{13}} d_{13}\left(1-\left|d_{13}\right|\right) + \dfrac{n_1^2 V_2 V_3}{2 n_2 n_3 f_s L_{23}}\left(d_{13}-d_{12}\right)\left(1-\left|d_{13}-d_{12}\right|\right) \end{cases} \tag{3.2}$$

The controller of the TAB is illustrated in Fig. 3-3(b). The I_{ref_2} and I_{ref_3} is given by dividing P_2 and P_3 by V_2 and V_3. The duty ratio is obtained through a current controller which is given as (3.3).

$$G_{c2,3}(s) = \frac{k_c}{s} \cdot \frac{\left(1+\dfrac{s}{\omega_z}\right)}{\left(1+\dfrac{s}{\omega_p}\right)} \tag{3.3}$$

where ω_z and ω_p are the angular speeds. And k_c denotes the gain. P_{3_ref} is determined by (3.4)

$$P_{3\_ref} = \begin{cases} P_{RES} - P_{load\_1} - P_2, & relation\ 1-3 \\ -P_2/2, & relation\ 4 \end{cases} \tag{3.4}$$

3.3.2. MODEL AND CONTROL OF HYDROGEN STATION

Fig. 3-4(a) and (b) show the model of FC and water electrolysis. They can be substituted by a voltage source with an internal resistor and a diode. The FC model is established based on its polarization curve [93],[94], which is given as (3.5).

$$V_{fc\_cell} = E + \eta_{act} + \eta_{ohmic} \tag{3.5}$$

It is assumed that the oxygen concentration and temperature are constants, and the η_{act} and η_{ohmic} are associated with FC current I_{fc}. The (3.5) can be written as (3.6) [93].

$$V_{fc\_cell} = E - B\ln(CI_{fc}) + R_{fc} I_{fc} \tag{3.6}$$

where B equals to 0.04777V, and C equals to 0.0136A^{-1}. R_{fc} is FC resistant. E is the voltage associated with the pressure of O_2, H_2 and H_2O, which is represented as (3.7).

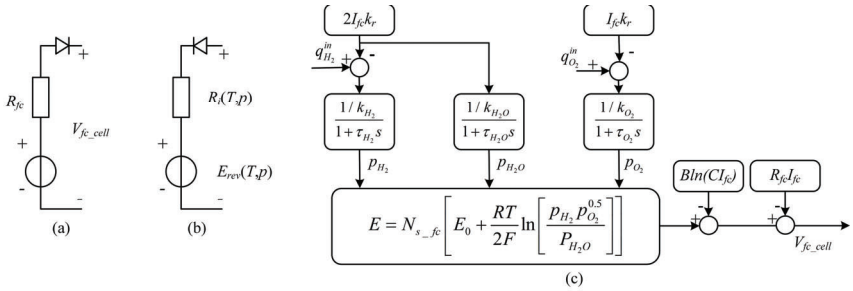

Figure 3-4 The model of FC and water electrolysis. (a) FC. (b) water electrolysis. (c) detail model of FC. [C2]

$$E = N_{s\_fc}\left[E_0 + \frac{RT}{2F}\log\left[\frac{p_{H_2}p_{O_2}^{0.5}}{P_{H_2O}}\right]\right] \tag{3.7}$$

where N_{s_fc} denotes the series number of FC cells, E_0 denotes open voltage of FC cell and R denotes the universal gas constant. The pressure in (3.7) is associated with molar flow, and Fig. 3-4(c) depicts the relationship.

Water electrolysis can decompose water into oxygen at the anode and hydrogen at the cathodic. Fig. 3-4(b) is the simplified model of water electrolysis cell, and the V-I curve can be given by (3.8) [95].

$$V(T,p) = n_s E_{rev}(T,p) + \frac{n_s}{n_p} IR_i(T,p) \tag{3.8}$$

Where n_s denotes series number and n_p denotes the parallel numbers. The reversible voltage E_{rev} and cell resistance R_i can be expressed by (3.9) and (3.10) [95].

$$E_{rev}(T,p) = E_{rev0} + R_{gas}\left(273+T\right)\frac{\ln\left(p/p_0\right)}{2F} \tag{3.9}$$

$$R_i(T,p) = R_{i0} + k\ln\left(\frac{p}{p_0}\right) + dR_t(T-T_0) \tag{3.10}$$

where E_{rev0} denotes the reference reverse voltage. R_{gas} is the ideal gas constant. F is the Faraday constant. k is curve fitting parameter. The value of these specific variables can be found in [95].

Fig. 3-5 shows the control of hydrogen station. The purpose of the outer voltage loop is to regulate and maintain the V_3 at 400V. The outer voltage controller will generate a current reference signal, and a LPF is added to divide the current signal into high-frequency component and low-frequency component. Since the dynamic response of FC and water electrolysis is slower than battery, the high-frequency part of current is distributed for battery control. If the value of I_{ref} exceeds 0V, I_{FC_ref} is set equal to I_{ref}, while I_{WE_ref} is set at 0V. Conversely, if I_{ref} is less than 0, I_{FC_ref} is set at 0V and I_{WE_ref} is minus of I_{ref}. Fig. 3-6 shows the control of renewable microgrids.

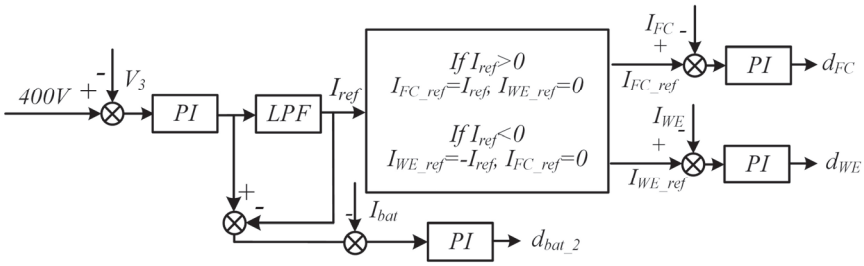

Figure 3-5 The control in hydrogen subsystem. [C2]

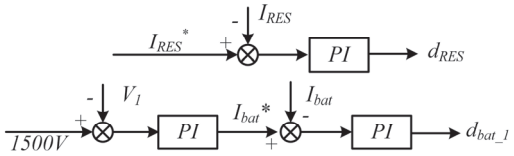

Figure 3-6 The control in renewable microgrid. [C2]

Table 3-1 The system parameters [C2]

System	Parameters	Value	Parameters	Value
DCTPS	Equivalent voltage V_{TS1}, V_{TS2} (V)	1500	Equivalent resistance R_{TS1}, R_{TS2} (Ω)	0.1
	Catenary resistance R_{line1} (Ω)	1e-2	Catenary resistance R_{line2} (Ω)	2e-2
TAB	Output capacitor $C_{1b,2b,3t}$ (mF)	5	Parasitic resistance $R_{1b,2b,3t}$ (mΩ)	1
	Leakage inductor L_1, L_2, L_3 (μH)	1	Switch frequency f_s (kHz)	20
	Controller gain ω_i	2.4	Angular speed of poles ω_p	16000
	Angular speed of zeros ω_z	200		
FC	Controller 0.0435+31.56/s			
WE	Controller 0.0019+10/s			
RES	Controller 0.0005+0.03/s			
Battery	Controller 1+10/s			

3.4. SIMULATION STUDY

The simulation validation is conducted using PLECS. Table 3-1 lists the required parameters for simulation.

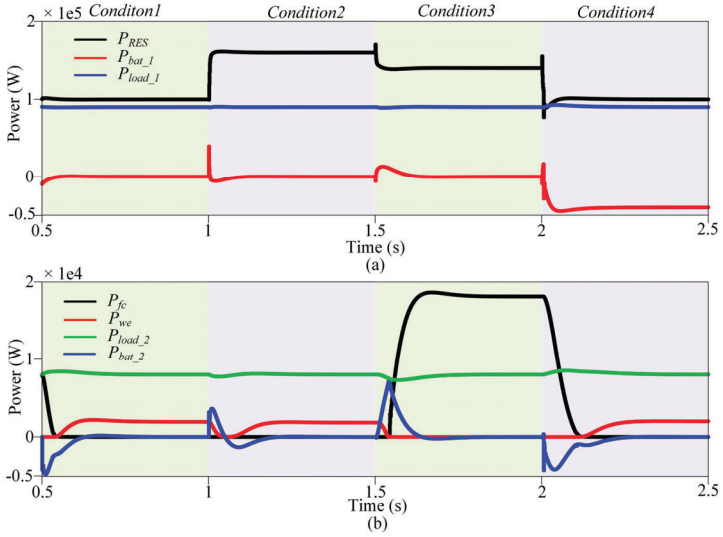

Figure 3-7 The power waveform. (a)renewable microgrid. (b) hydrogen station. [C2]

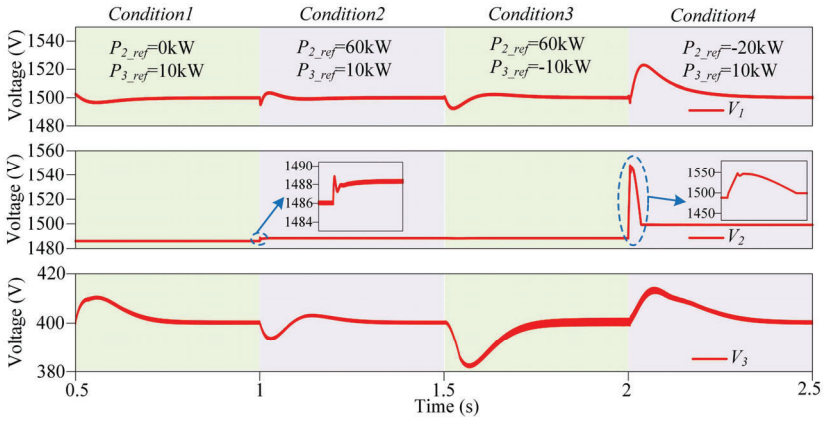

Figure 3-8 The voltage waveform at each port. [C2]

Fig. 3-7 shows the power variation of renewable microgrids and hydrogen station during four conditions corresponding to the four power-flowing relationships. Fig.

3-8 shows the terminal voltage variation of TAB converter during four conditions corresponding.

From 0.5s to 1s, condition 1 is executed. The P_{2_ref} is set to 0kW. P_{RES} is maintained at 100kW, P_{load_1} is 90kW and P_{load_2} is 8kW in this condition. According to (3.4), the P_{3_ref} is 10kW. As depicted in Figure 3-7 (b), it's evident that the surplus 2 kW is utilized by the water electrolysis.

From 1s to 1.5s, condition 2 is performed in which the P_{RES} is increased to 160kW and P_{RES} is sufficient. P_{DCTPS} is 400kW. P_{2_ref} is 60kW. As depicted in Figure 3-8, the catenary voltage shows an increase from 1486V to 1488V.

From 1.5s to 2s, condition 3 is performed. P_{RES} is decreased to 140kW, which is insufficient for DCTPS. P_{3_ref} is -10kW in this condition. As depicted in Figure 3-7(b), the FC provides 18 kW to support the DCTPS during this period.

From 2s to 2.5s, P_{DCTPS} is -20kW. In Fig. 3-8, it is evident that the RBE contributes to an increase in the catenary voltage. The V_2 is increased from 1488V to 1548V at 2.05s. Then, the TAB converter starts absorbing the RBE. P_{3_ref} is -20kW in this condition. As depicted in Figure 3-8, the V_1 and V_3 can be consistently maintained at 1550V and 400V.

3.5. CONCLUSION

This Chapter presents a DCTPS integrated with RESs and hydrogen by TAB converter. The model and control of the TAB converter and hydrogen stations are presented. The simulation results demonstrate that the TAB converter can quickly and effectively manage the power among three ports. Hydrogen stations can efficiently utilize RBE and surplus energy form renewable microgrids.

CHAPTER 4. IMPEDANCE DERIVATION AND STABILITY OF TAB CONVERTER-BASED DCTPS

4.1. INTRODUCTION

In this Chapter, the stability of TAB converter-based DCTPS is to be discussed. Most of stability analysis for two-port DC/DC converters adopts impedance-based method which requires an accurate input or output impedance of two-port DC/DC converter. For TAB converter, it is complicated to obtain the impedance from control block diagram in [70]. In this work, the extra element theorem (EET) [65], [96] is used to obtain the input and output impedance of TAB converter. One or two elements such as resistors can be removed firstly to simplify the circuit and then add them back into the circuit by EET. In this chapter, the terminal impedance of renewable microgrids, DCTPS and hydrogen station are regarded as the extra element. Three cases with different power-flowing directions are considered. The stability of the system corresponding to the three cases is analyzed by impedance-based method. Finally, Simulation and experiment are given for verification.

4.2. SYSTEM CONFIGURATION

Fig. 4-1 shows the structure of the systems, where the renewable microgrids are substituted by a synchronous buck-boost converter to maintain the bus voltage of port1 (V_1). DCTPS is simulated as a CPL when it absorbs power and a constant power source when it feedbacks RBE. In addition, only water electrolyzer is considered so that hydrogen station can only absorb power from TAB converter.

Thus, the power-flowing relationship in the systems can be categorized as the following three cases, which are shown in Fig. 4-2.

1) In this case, renewable microgrids primarily support DCTPS and the excessive energy is delivered to the hydrogen station.
2) In this case, the power of renewable energy and RB energy from the braking train in DCTPS is utilized for hydrogen production in hydrogen station.
3) In this case, the RB energy is feedback to renewable microgrids and hydrogen stations.

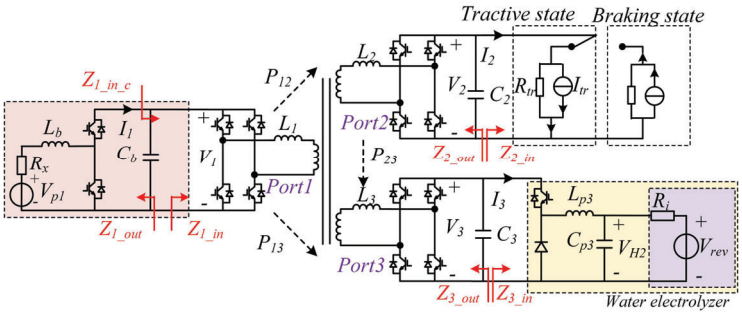

Figure 4-1 The proposed structure of TAB converter-based DCTPS. [J2]

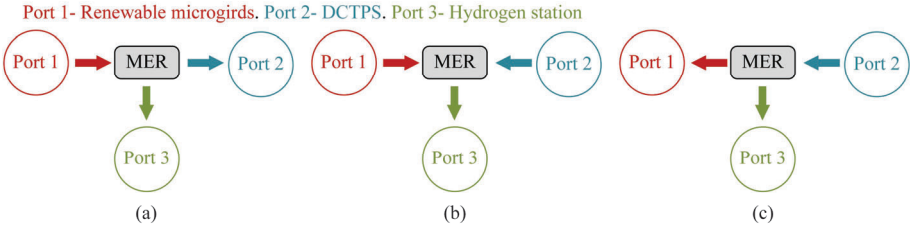

Figure 4-2 The power relationship of three different cases. (a) case1. (b) case2. (c) case3.

4.3. TERMINAL IMPEDANCE OF SYSTEM

4.3.1. TERMINAL IMPEDANCE OF RENEWABLE MICROGRID, HYDROGEN STATION AND DCTPS

A. Output impedance of renewable microgrid

In this work, the renewable microgrid is responsible for supporting the port1 voltage (V_1). The synchronous converter is operated in boost mode. Fig. 4-3 shows its small signal model. The variables at steady state are marked by superscript "-", and the small signal disturbance of variable is marked by the superscript "^". The Z_{1_out} represents the unterminated output impedance of synchronous buck-boost converter, which is defined as the impedance that the load is not considered. To obtain the Z_{1_out}, the load is substituted by ideal current source [96]. But the transfer function is also associated with load R_{DC}, which equals V_1/i_{load}. The open-loop output impedance of the converter is given by (4.1)

$$Z_{1\_out}^{open} = \frac{s^2 L_b C_b R_b + s\left(L_b + C_b R_b R_x\right) + R_x}{s^2 L_b C_b + sC_b R_x + \left(1-\bar{D}\right)^2 sC_b R_b + \left(1-\bar{D}\right)^2} \tag{4.1}$$

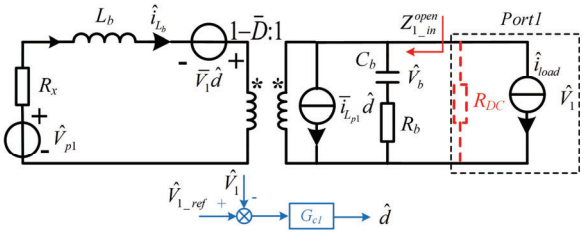

Figure 4-3 The small signal model of synchronous converter in boost mode. [J2]

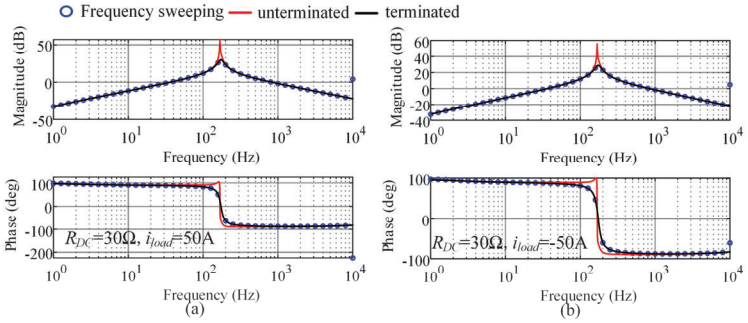

Figure 4-4 Comparison of analytical results and AC sweeping. (a) I_{load}=50A. (b) I_{load}=-50A. [J2]

Table 4-1 The systems parameters in Simulation [J2]

Parameters	value	Parameters	value	Parameters	value
Voltage $V_{1,2,3}$ (V)	1500	Inductor $L_{1,2,3}$ (μH)	20	Inductor L_{p3}(μH)	2000
Capacitor $C_{2,3}$ (μF)	200	Cap *ESR* $R_{c2,c3}$ (Ω)	0.01	Input voltage V_{p1} (V)	1000
Winding turn n_1:n_2:n_3	1:1:1	Switching frequency	10kHz	Capacitor C_{p3}(μF)	100
Inductor L_b (μH)	2000	Capacitor C_b (μF)	200	Internal resistor R_x (Ω)	0.01
Capacitor ESR R_b (Ω)	0.01	G_c: 0.01+1/s		G_{c1}: 3e-5+3e-3/s	
$G_{con2,3}$: 1e-5+0.01/s					

When the voltage control is implemented, the output impedance can be given as (4.2).

$$Z_{1\_out} = Z_{1\_out}^{open} / \left(1+T_1\right) \tag{4.2}$$

$$T_1 = G_{c1}G_{vd1} \tag{4.3}$$

where the T_1 is the loop gain, G_{c1} denotes the voltage controller and G_{vd1} denotes the transfer function of duty ratio to output voltage. It can be obtained by (4.4).

$$G_{vd1}=\frac{\left(sC_bR_b+1\right)R_{DC}\left[\bar{V}_1\left(1-\bar{D}\right)-\frac{i_{load}\left(sL_b+R_x\right)}{1-\bar{D}}\right]}{\left(sC_bR_b+1\right)R_{DC}\left(1-\bar{D}\right)^2+\left(sL_b+R_x\right)\left[sC_b\left(R_b+R_{DC}\right)+1\right]} \tag{4.4}$$

Fig. 4-4 illustrated the AC sweeping results in PLECS when R_{DC} is 30Ω and i_{load} is ±50A. The parameters are given in Table 3-1. The analytical results match well with terminated impedance.

B. Input impedance buck converter in hydrogen station

The water electrolyzer is simulated by voltage V_{rev} with resistance R_i [97]. When the voltage of buck converter is set at 200V, V_{rev} is 169.7V and R_i is 0.187Ω.

Its small signal model is illustrated in Fig. 4-5. The closed-loop admittance Y_{3_in} can be obtained by the feedback theorem [65], which is given as (4.5)

$$Y_{3\_in}=\frac{1}{Z_{3\_in}}=Y_{i\infty}\frac{T}{1+T}+Y_{i0}\frac{1}{1+T} \tag{4.5}$$

where $Y_{i\infty}$ and Y_{i0} are represented as (4.6). The loop gain T and the transfer function G_{vd} are given as (4.7), and system parameters including PI controller are given in Table 4-1.

$$Y_{i\infty}=-\frac{\bar{V}_3^2}{\bar{D}\bar{V}_3\left(\bar{D}\bar{V}_3-\bar{V}_{rev}\right)}R_i \tag{4.6}$$

$$Y_{i0}=\frac{sC_{p3}R_i\bar{D}^2+R_i\bar{D}^2}{s^2LC_{p3}R_i+sLR_i+R_i} \tag{4.7}$$

$$T=G_cG_{vd} \tag{4.8}$$

$$G_{vd}=\bar{V}_3\frac{R_i}{s^2L_{p3}C_{p3}R_i+sL_{p3}+R_i} \tag{4.9}$$

Fig. 4-6 shows the comparison of impedance characteristics of analytical results and AC sweeping. It is evident that the derivation of input impedance of buck converter is accurate.

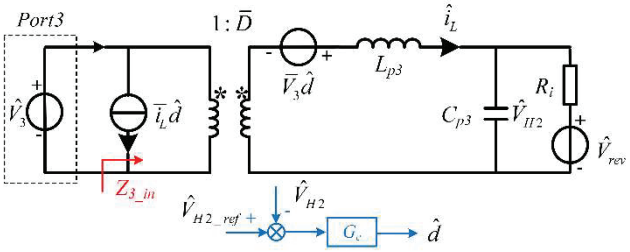

Figure 4-5 The small signal model of buck converter. [J2]

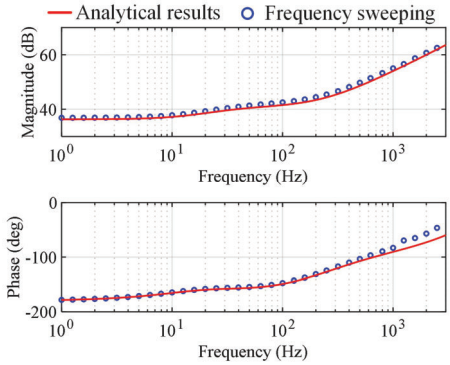

Figure 4-6 The comparison of analytical results and AC sweeping. [J2]

C. Impedance model of DCTPS

The DCTPS is simulated as a CPL when most trains are tractive in power supply section and a power source when most trains are in braking state. The linearization function of CPL is given by (4.10).

$$I_{tr} = -\frac{P_{tr}}{\bar{V}_2^2} V_2 + 2\frac{P_{tr}}{\bar{V}_2} \tag{4.10}$$

where P_{tr} represents the power of DCTPS. $\bar{V}_2$ represents the steady voltage of port2 which is 1500V in this work. The impedance of DCTPS is given as (4.11). P_{tr} is negative and R_{tr} is positive when the power of DCTPS is absorbed by TAB converter.

$$R_{tr} = -\bar{V}_2^2 / P_{tr} \tag{4.11}$$

4.3.2. TERMINAL IMPEDANCE OF TAB CONVERTER

As mentioned in Chapter 3, the small signal model of TAB converter is established by a three-port gyrator [98], [99]. It can be represented as (4.12).

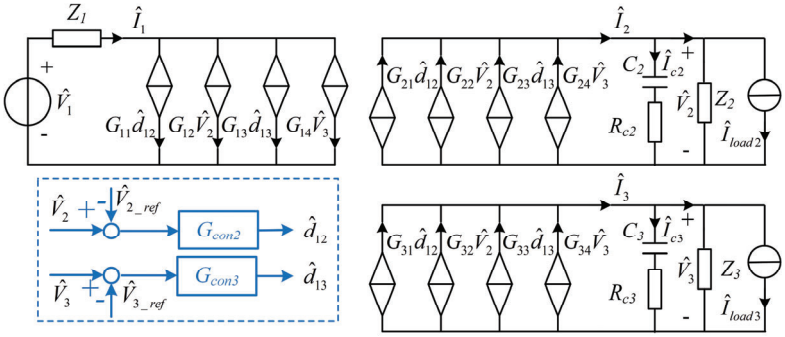

Figure 4-7 The small signal model of TAB converter. [J2]

$$\begin{bmatrix}\hat{I}_1\\ \hat{I}_2\\ \hat{I}_3\end{bmatrix}=\begin{bmatrix}0 & G_{12} & G_{14}\\ G_{22} & 0 & G_{24}\\ G_{32} & G_{34} & 0\end{bmatrix}\begin{bmatrix}\hat{V}_1\\ \hat{V}_2\\ \hat{V}_3\end{bmatrix}+\begin{bmatrix}G_{11} & G_{13}\\ G_{21} & G_{23}\\ G_{31} & G_{33}\end{bmatrix}\begin{bmatrix}\hat{d}_{12}\\ \hat{d}_{13}\end{bmatrix} \tag{4.12}$$

where the coefficients in the matrix are listed in Appendix.

According to the Fig. 4-7, The representation of voltage and current at each port can be expressed as (4.13).

$$\begin{aligned}
&\hat{I}_2-\frac{\hat{V}_2}{Z_2}-\hat{I}_{load2}=\frac{sC_2\hat{V}_2}{sR_{c2}C_2+1}\\
&\hat{I}_3-\frac{\hat{V}_3}{Z_3}-\hat{I}_{load3}=\frac{sC_3\hat{V}_3}{sR_{c3}C_3+1}\\
&\hat{I}_1=G_{11}\hat{d}_{12}+G_{12}\hat{V}_2+G_{13}\hat{d}_{13}+G_{14}\hat{V}_3\\
&\hat{I}_2=G_{21}\hat{d}_{12}+G_{22}\hat{V}_1+G_{23}\hat{d}_{13}+G_{24}\hat{V}_3\\
&\hat{I}_3=G_{31}\hat{d}_{12}+G_{32}\hat{V}_1+G_{33}\hat{d}_{13}+G_{34}\hat{V}_2\\
&\hat{d}_{12}=\left(\hat{V}_{2_ref}-\hat{V}_2\right)G_{con2}\ ,\ \hat{d}_{13}=\left(\hat{V}_{3_ref}-\hat{V}_3\right)G_{con3}
\end{aligned} \tag{4.13}$$

where R_{c2} and R_{c3} are the ESR of capacitors C_2 and C_3. G_{con2} and G_{con3} are voltage controller.

A. Unterminated output impedance of TAB converter

The impedance Z_1, Z_2 and Z_3 are the extra element. According to the principle of EET [65], [96], the unterminated output impedance (Z_{2_out}) disregarding Z_2 can be given by (4.14)

$$Z_{2\_out}(s)=\frac{-\hat{V}_2(s)}{\hat{I}_{load2}(s)}=H_r(s)\left(\frac{1+\dfrac{Z_N^3(s)}{Z_3(s)}}{1+\dfrac{Z_D^3(s)}{Z_3(s)}}\right)\left(\frac{1+\dfrac{Z_1(s)}{Z_N^1(s)}}{1+\dfrac{Z_1(s)}{Z_D^1(s)}}\right) \tag{4.14}$$

where the H_r(s) denotes the unterminated output impedance disregarding the Z_3 and the Z_1. Therefore, by exchanging Z_1=0, Z_2=∞, Z_3=∞, $\hat{V}_1$ =0 and $\hat{I}_{load3}$=0 into (4.13), the H_r(s) is obtained by (4.15).

$$H_r(s)=\frac{-\hat{V}_2(s)}{\hat{I}_{load2}(s)}=\frac{1}{\dfrac{sC_2}{sC_2R_{c2}+1}+G_{21}G_{con2}+(G_{23}-G_{24})\alpha_1} \tag{4.15}$$

$$\alpha_1=\frac{(sR_{c3}C_3+1)(G_{34}-G_{31}G_{con2})}{sC_3+G_{33}G_{con3}(sR_{c3}C_3+1)} \tag{4.16}$$

Then, Z_3 is put in the circuit. The effect of Z_3 is reflected by the term (1+ Z_N^3/ Z_3)/(1+ Z_D^3/ Z_3). The Z_D^3(s) denotes the driving point impedance when the $\hat{I}_{load2}$ is set at zero. Fig. 4-8(a) is illustration of Z_D^3(s), where a current source substitutes the Z_3 and I_{load3}. The Z_D^3(s) can be obtained as (4.17) by replacing Z_1=0, Z_2=∞, $\hat{V}_1$ =0, $\hat{I}_{load2}$=0 and $\hat{I}_{load3}$ =0 into (4.13).

$$Z_D^3(s)=\frac{\hat{V}_T}{\hat{I}_T}=\frac{1}{\dfrac{sC_3}{sR_{c3}C_3+1}+(G_{31}G_{con2}-G_{34})\alpha_2+G_{33}G_{con3}} \tag{4.17}$$

$$\alpha_2=\frac{(G_{24}-G_{23}G_{con3})(sR_{c2}C_2+1)}{sC_2+G_{21}G_{con2}(sR_{c2}C_2+1)} \tag{4.18}$$

As depicted in Fig. 4-8(b), Z_N^3(s) refers to the null driving point impedance when $\hat{V}_2$ is set at zero. Consequently, the phase shift ratio d_{12} is forced to zero. Z_N^3(s) can be derived as (4.19).

$$Z_N^3(s)=\frac{\hat{V}_T}{\hat{I}_T}=\frac{sC_3R_{c3}+1}{sC_3+G_{33}G_{con3}(sC_3R_{c3}+1)} \tag{4.19}$$

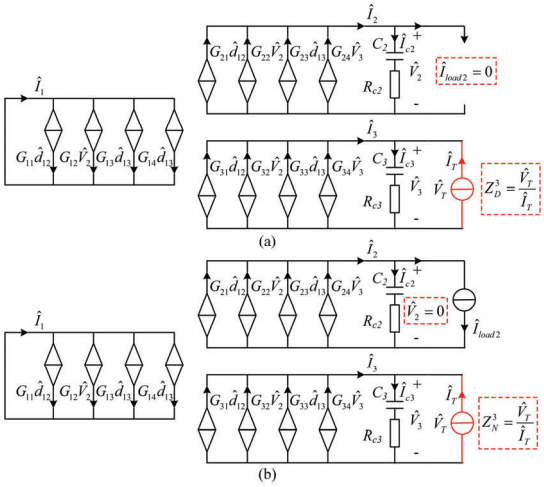

Figure 4-8 The illustration of $Z_D^3(s)$ and $Z_N^3(s)$. (a) $Z_D^3(s)$. (b) $Z_N^3(s)$. [J2]

Next, Z_1 is put in the circuit. The effect of Z_1 is reflected by the term $(1+ Z_1/ Z_N^1)/(1+ Z_1/ Z_D^1)$. Similarly, the derivation of $Z_D^1(s)$ and $Z_N^1(s)$ are illustrated in Fig. 4-9. The $Z_D^1(s)$ denotes the driving point impedance when $\hat{I}_{load2}$ is set at zero. The $Z_D^1(s)$ can be obtained as (4.20) by substituting $Z_2=\infty$, $\hat{I}_{load2}=0$ and $\hat{I}_{load3}=0$ into (4.13).

$$Z_D^1(s)=\frac{\hat{V}_T}{\hat{I}_T}=\frac{1}{G_{12}M_2-G_{11}G_{con2}M_2-G_{13}G_{con3}M_1+G_{14}M_1} \tag{4.20}$$

$$\begin{cases} M_1=\dfrac{G_{22}K_4-G_{32}K_2}{K_1K_4-K_3K_2} \\ M_2=\dfrac{G_{22}K_3-G_{32}K_1}{K_2K_3-K_1K_4} \end{cases}, \begin{cases} K_1=\dfrac{sC_2}{sC_2R_{c2}+1}+G_{21}G_{con2}, K_2=G_{23}G_{con3}-G_{24} \\ K_3=G_{31}G_{con2}-G_{34}, K_4=\dfrac{sC_3}{sC_3R_{c3}+1}+\dfrac{1}{Z_3}+G_{33}G_{con3} \end{cases} \tag{4.21}$$

The $Z_N^1(s)$ refers to the null driving point impedance when $\hat{V}_2$ is set at zero. Also, the phase shifting ratio d_{12} is forced to zero. The $Z_D^1(s)$ is be derived by (4.22) when $Z_2=\infty$, $\hat{d}_{12}=0$, $\hat{V}_2=0$ and $\hat{I}_{load3}=0$ are replaced into (4.13).

$$Z_N^1(s)=\frac{\hat{V}_T}{\hat{I}_T}=\frac{\dfrac{sC_3}{sR_{c3}C_3+1}+\dfrac{1}{Z_3}+G_{33}G_{con3}}{\left(G_{14}-G_{13}G_{con3}\right)G_{32}} \tag{4.22}$$

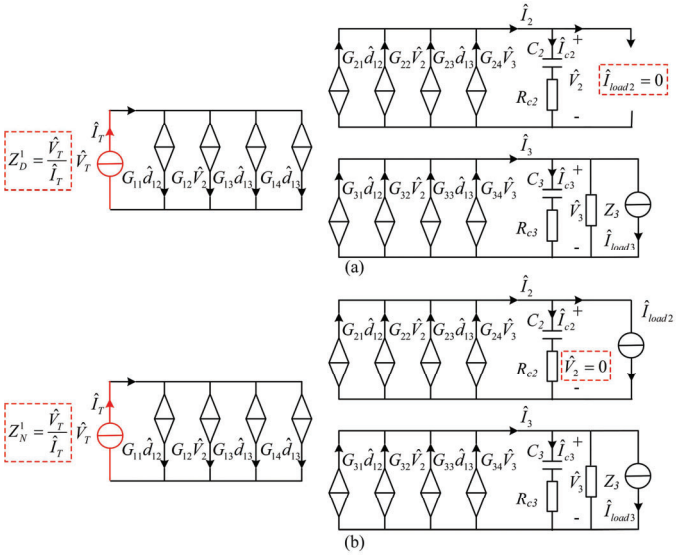

Figure 4-9 The illustration of $Z_D^1(s)$ and $Z_N^1(s)$. (a) $Z_D^1(s)$. (b) $Z_N^1(s)$. [J2]

B. Terminated output impedance of TAB converter

Now, Z_2 is put in the circuit. The terminated output impedance of port2 $Z_{2\_out\_c}(s)$ is given by (4.23).

$$Z_{2\_out\_c}(s) = Z_{2\_out}(s)\frac{\left(1+\frac{Z_N^2(s)}{Z_2(s)}\right)}{\left(1+\frac{Z_D^2(s)}{Z_2(s)}\right)} \tag{4.23}$$

For the $Z_N^2(s)$, because $\hat{V}_2$ is set to zero, V_T is zero, thereby $Z_N^2(s)$ is also zero. For the $Z_D^2(s)$, since $\hat{I}_{load2}$ is zero, the equals to unterminated output impedance $Z_{2\_out}(s)$. Thus, (4.23) can be rewritten as (4.24).

$$Z_{2\_out\_c}(s) = \frac{Z_{2\_out}(s)}{1+\frac{Z_{2\_out}(s)}{Z_2(s)}} \tag{4.24}$$

Also, the unterminated and terminated output impedance of port3 can be derived in the same way.

C. *Input impedance of TAB converter*

The input impedance Z_{1_in}(s) is given by (4.25).

$$Z_{1\_in}(s)=H_{in}(s)\left(\frac{1+\frac{Z^3_{N\_in}(s)}{Z_3(s)}}{1+\frac{Z^3_{D\_in}(s)}{Z_3(s)}}\right)\left(\frac{1+\frac{Z^2_{N\_in}(s)}{Z_2(s)}}{1+\frac{Z^2_{D\_in}(s)}{Z_2(s)}}\right) \tag{4.25}$$

where H_{in}(s) denotes the input impedance disregarding Z_2 and Z_3. Therefore, H_{in}(s) is given by (4.26) when replacing $Z_2=\infty$, $Z_3=\infty$, $\hat{I}_{load2}=0$ and $\hat{I}_{load3}=0$ are replaced into (4.13).

$$H_{in}(s)=\frac{\hat{V}_1}{\hat{I}_1}=\frac{1}{(G_{12}-G_{11}G_{con2})M_3+(G_{14}-G_{13}G_{con3})M_4} \tag{4.26}$$

$$\begin{cases} M_3=\dfrac{G_{22}b_2-G_{32}b_1}{a_1b_2-a_2b_1} \\ M_4=\dfrac{G_{22}a_2-G_{32}a_1}{b_1a_2-b_2a_1} \end{cases},\quad \begin{cases} a_1=\dfrac{sC_2}{sC_2R_{c2}+1}+G_{21}G_{con2}\ ,\ b_1=G_{23}G_{con3}-G_{24} \\ a_2=G_{31}G_{con2}-G_{34}\ ,\ b_2=\dfrac{sC_3}{sC_3R_{c3}+1}+G_{33}G_{con3} \end{cases} \tag{4.27}$$

Then, Z_3 is put in the circuit. The $Z_{D\_in}{}^3$(s) is driving point impedance at port1. Thus, $Z_{D\_in}{}^3$(s) is given by (4.28) when $Z_2=\infty$, $\hat{I}_1=0$, $\hat{I}_{load2}=0$ and $\hat{I}_{load3}=0$ are replaced into (4.13).

$$Z^3_{D\_in}(s)=\frac{1}{\frac{sC_3}{sC_3R_{c3}+1}+G_{33}G_{con3}-G_{32}Q_2+(G_{31}G_{con2}-G_{34})Q_1} \tag{4.28}$$

$$Q_1=\frac{G_{13}G_{con3}-G_{14}}{G_{12}-G_{11}G_{con2}},\quad Q_2=\frac{\left(\frac{sC_2}{sC_2R_{c2}+1}+G_{21}G_{con2}\right)Q_1+G_{23}G_{con3}-G_{24}}{G_{22}} \tag{4.29}$$

By substituting $Z_2=\infty$, $\hat{V}_1=0$, $\hat{I}_{load2}=0$ and $\hat{I}_{load3}=0$ into (4.13), $Z_{N\_in}{}^3$(s) can be obtained as (4.30).

$$Z_{N\_in}^{3}(s)=\frac{1}{\frac{sC_3}{sC_3R_{c3}+1}+G_{33}G_{con3}+\left(G_{31}G_{con2}-G_{34}\right)b_3} \tag{4.30}$$

$$b_3=\frac{G_{24}-G_{23}G_{con3}}{\frac{sC_2}{sC_2R_{c2}+1}+G_{21}G_{con2}} \tag{4.31}$$

Then, Z_2 is put in the circuit. Replacing $\hat{V}_1$ =0, $\hat{I}_{load2}$=0 and $\hat{I}_{load3}$ =0 into (4.13), the $Z_{N\_in}^{2}$ can be obtained as (4.32)

$$Z_{N\_in}^{2}(s)=\frac{1}{\frac{sC_2}{sC_2R_{c2}+1}+G_{21}G_{con2}+\left(G_{24}-G_{23}G_{con3}\right)K_{40}} \tag{4.32}$$

$$K_{40}=\frac{G_{34}-G_{31}G_{con2}}{\frac{sC_3}{sC_3R_{c3}+1}+G_{33}G_{con3}+\frac{1}{Z_3}} \tag{4.33}$$

$Z_{D\_in}^{2}$ can be represented as (4.34) when $\hat{I}_1$ =0, $\hat{I}_{load2}$=0 and $\hat{I}_{load3}$ =0 are replaced into (4.13) .

$$Z_{D\_in}^{2}(s)=\frac{1}{G_{21}G_{con2}+\left(G_{24}-G_{23}G_{con2}\right)K_{10}+G_{22}K_{20}+\frac{sC_3}{sC_3R_{c3}+1}} \tag{4.34}$$

$$K_{10}=\frac{G_{11}G_{con2}-G_{12}}{G_{14}-G_{13}G_{con3}},K_{20}=\frac{\left(\frac{sC_3}{sC_3R_{c3}+1}+\frac{1}{Z_3}+G_{33}G_{con3}\right)K_{10}+G_{31}G_{con2}-G_{34}}{G_{32}} \tag{4.35}$$

To do AC sweeping for input impedance of port1, the input capacitor should be considered [66], [70]. Thus, the input impedance of port1 is represented as (4.36).

$$Z_{1\_in\_c}=\frac{sC_bR_bZ_{1\_in}+Z_{1\_in}}{sC_b\left(R_b+Z_{1\_in}\right)+1} \tag{4.36}$$

Table 4-1 lists the system parameters. Table 4-2 illustrate the analytical curve and AC sweeping points. It is obvious that the AC sweeping results are consistent with the analytical results in different power-flowing directions.

D. The effect of controller parameters on the terminal impedance

Fig. 4-10 displays the loop gain characteristics where a 50Ω resistor is terminated to port2 and a 100Ω resistor is terminated to port3. The phase margin (PM) is 55.6 degrees for port2 and 48.4 degrees for port3. Both phase margins in port2 and port3 are larger than 45 degrees, which means the voltage control loop is stable.

Fig. 4-11 shows the input and output impedance when the parameters in controller is shifted. It can be found that the output impedance of TAB rises when k_p is reduced. Also, the resonant frequency of output impedance is increased when the k_i is increased.

4.4. STABILITY ANALYSIS OF DIFFERENT CASES

In this section, the stability of the systems of these three cases is examined by the

Table 4-2 The unterminated and terminated impedance in different cases[J2]

	Port2	Port3	Port1
Case1	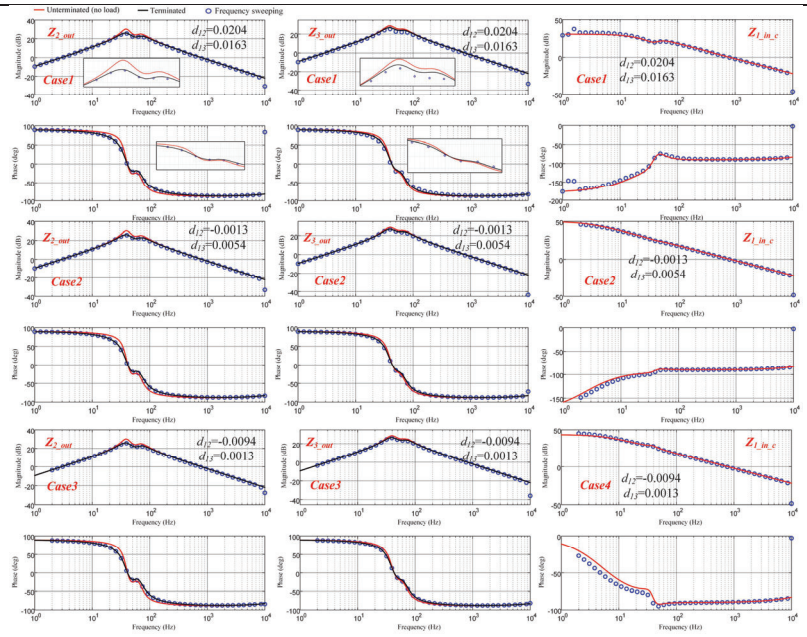		
Case2			
Case3			

impedance-based method.

A. Case1: Renewable microgrid supports DCTPS and hydrogen station

There are two situations under this case. Fig. 4-12(a)-(c) displays the unterminated impedance at each port as P_{tr} increases and output voltage of buck converter V_{H2} is kept at 203V. As depicted in Fig. 4-12(b), two intersection points are observed when P_{tr} is shifted to 32kW. The left intersection occurs at a frequency of 37.8Hz, with a corresponding PM of -18.7 degrees. It signifies that the port 2 will exhibit instability issues by a 37.8Hz fluctuation. As illustrated in Fig. 4-12(a), the intersection occurs at a frequency of 37.6Hz, with a corresponding PM of -74 degrees. Moreover, as illustrated in Fig. 4-12(c), the intersection point occurs at a frequency of 37.6Hz, with a corresponding PM of -17.3 degrees. It signifies that port 1 and port 3 will exhibit instability issues by a 37.6Hz fluctuation.

In Fig. 4-12(d) to Fig. 4-12(f), the impedance at each port is displayed when V_{H2} raises from 180V to 204V while maintaining P_{tr} at 32kW. As depicted in Fig. 4-12(f), it is noticeable that no intersection point is presented when V_{H2} is 180V. But the intersection points are presented when V_{H2} boost to 204V. The intersection occurs at a frequency of 37.4Hz, with a corresponding PM of -25.9 degrees. It signifies that port 3 will exhibit instability issues by a 37.4Hz fluctuation. As illustrated in Fig. 4-12(e), the intersection occurs at a frequency of 37.1Hz, with a

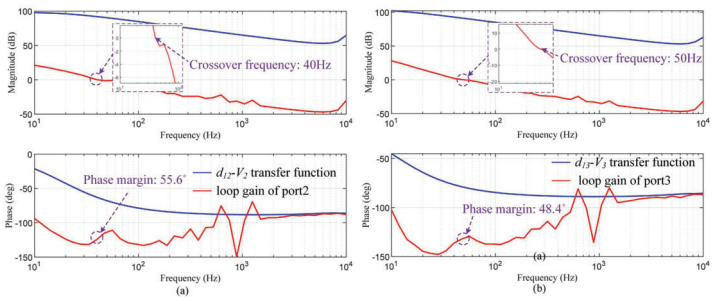

Figure 4-10 The loop gain of TAB converter. (a)port2. (b)port3. [J2]

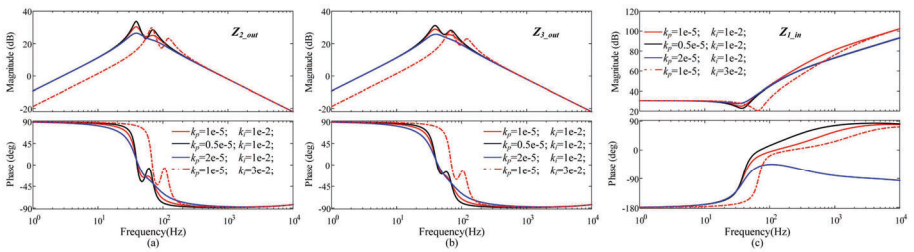

Figure 4-11 The terminal impedance when parameters in controller is changed. (a) Port2. (b) Port3. (c) Port11. [J2]

corresponding PM of -25.5 degrees. Meanwhile, as illustrated in Fig. 4-12(d), the intersection occurs at a frequency of 37.6Hz, with a corresponding PM of -83 degrees. It signifies that port 1 and port 2 will exhibit instability issues by a 37.6Hz fluctuation and a 37.1Hz fluctuation. Therefore, when the TAB converter connects with two CPLs, increasing the power of one CPL will trigger issues.

B. Case2: Hydrogen station supplied by renewable microgrid and DCTPS

The impedance at each port in case 2 is illustrated in Fig. 4-13(a)-(c). Fig. 4-13(a)

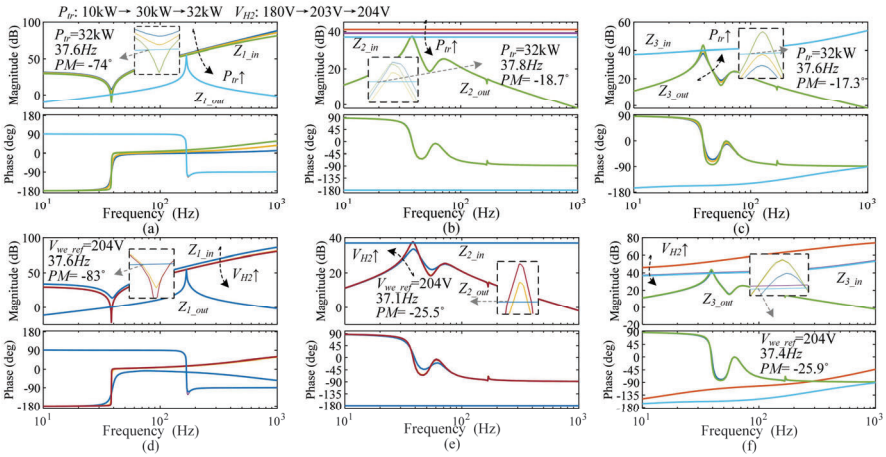

Figure 4-12 The Impedance of two situations for case1. (a) Z_{1_in} in situation one. (b) Z_{2_out} in situation one. (c) Z_{3_out} in situation one. (d) Z_{1_in} in situation two. (e) Z_{2_out} in situation two. (f) Z_{3_out} in situation two. [J2]

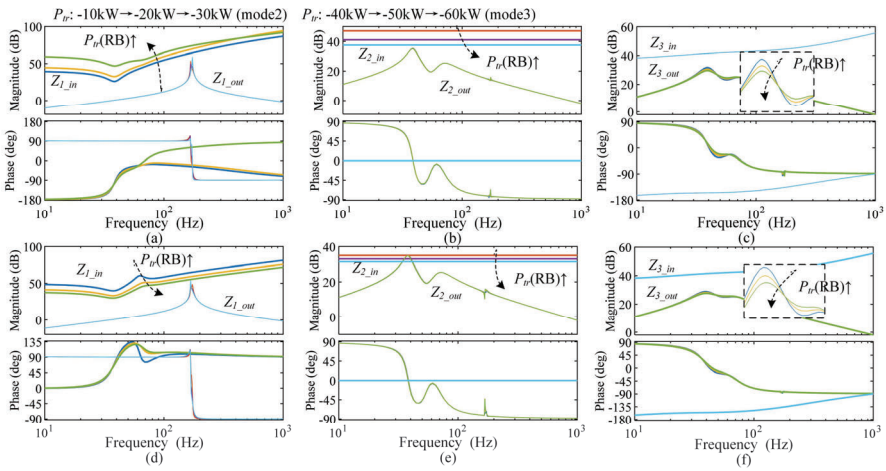

Figure 4-13 The Impedance of case2 and case3. (a) Z_{1_in} in case two. (b) Z_{2_out} in case two. (c) Z_{3_out} in case two. (d) Z_{1_in} in case three. (e) Z_{2_out} in case three. (f) Z_{3_out} in case three. [J2]

reveals that there is no intersection point between between Z_{1_in} and Z_{1_out} when P_{tr} increases. Also, no intersection points are presented in Fig. 4-13(c). Although there are intersection points in Fig. 4-13(b), the PM exceeds zero degrees. Therefore, It signifies that the system is stable in this case.

C. Case3: RB energy of DCTPS is feedback to renewable microgrid and hydrogen station

The impedance at each port in case 3 is illustrated in Fig. 4-13(d)-(f). As depicted in Fig. 4-13(d), it is evident that the Z_{1_in} is decreased when P_{tr} increases. However, no intersection point is presented at port1. Furthermore, as illustrated in Fig. 4-13(f), the Z_{3_out} is far away from the Z_{3_in} as P_{tr} increases. Fig. 4-13(d) and Fig. 4-13(f) indicate that port1 and port 3 would not fluctuate in this cases3. As illustrated in Fig. 4-13(e), two intersection points are presented. While the PM exceeds zero degress. Thus, port 2 would not fluctuate in the cases3.

The impedance analysis in this section reveals that (1) the voltage fluctuation exists at three port when TAB converter adopts the voltage control, and DCTPS and hydrogen station absorb energy from TAB converter simultaneously. (2) reversing power flowing at a specific port can effectively resolve the instability issue occurring at the remaining ports.

4.5. SIMULATION AND EXPERIMENTAL TEST

A. Simulation test

In order to validate of the stability analysis, simulation verification has been carried out by using PLECS. The system parameters for simulation verification are listed in Table 4-1.

Fig. 4-14(a) illustrates the voltage waveform of case1. At 1.5s, P_{tr} is boosted from 10 kW to 32kW, and the voltage at port1, port2 and port3 fluctuates. The oscillation frequency at port1- 3 is 38.05Hz, 37.95Hz and 37.95Hz, respectively. It is evident that the simulation outcomes conform to the stability analysis of situation one in case1 shown in Fig. 4-12(a)-(c).

Fig. 4-14(b) illustrates the voltage waveform of case2. The V_{H2} is boosted to 203V at 1.5s, the voltage at port1, port2 and port3 fluctuates. The fluctuation frequency observed at these three ports are approximately 37Hz. Furthermore, the amplitude of voltage waveform would be increased when V_{H2} is boosted to 204V. Therefore, the simulation outcomes conform to the stability analysis of situation two in case1 shown in Fig. 4-12(d)-(f).

Fig. 4-14(c) illustrates the voltage waveform of case2 and case3. It is evident that the oscillation is suppressed when DCTPS starts feeding RB energy to TAB converter, which conforms to the analysis of case2 and case3 as shown in Fig. 4-13.

B. Experimental test

The experiment has been conducted in a scale-down prototype to further substantiate the stability analysis. The prototype is shown in Fig. 4-15. An load (EA-EL 9160-100) operating in constant power mode simulates the DCTPS in case1 and hydrogen production in case2 and case3. The buck-boost converter is used to simulate hydrogen production in case1 and RBE of DCTPS in case2 and case3. The control of all power stages is implemented by PLECS RTbox. A grid emulator (CA instruments MX30) is used to emulate the renewable microgrid. The experimental parameters are listed in Table 4-3.

Fig. 4-16(a) illustrates the impedance of situation one in cases1. As depicted in Fig. 4-16(a) where V_{H2} is maintained at 40V, intersection points are presented at port2 as P_{tr} is boosted from 60W to 100W, and the PM is smaller than zero degrees. It signifies that the whole system will exhibit instability issues.

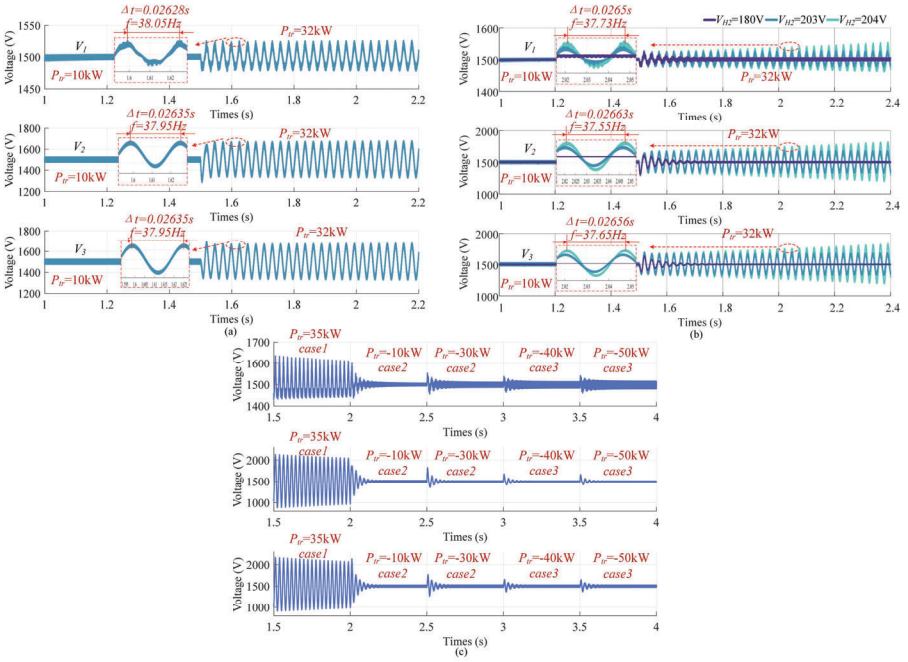

Figure 4-14 The voltage waveform. (a) Situation one of Case1. (b) Situation two of Case1. (c) Case2 and Case3. [J2]

Fig. 4-16(b) illustrates the impedance of situation two in cases1. As depicted in Fig. 4-16(b), Z_{3_out} and Z_{3_in} tend to intersect as V_{H2} increases. And the phase difference is larger than 180 degrees. It signifies that the whole system will exhibit instability issues when V_{H2} is increased from 40V to 49V.

Fig. 4-17(a) and (b) shows the voltage and current waveform of each port at situation one of case1. The original power of P_{tr} at port2 is 20W. the voltage and current fluctuate at each port as P_{tr} is increased to 60W. When P_{tr} is reduced, the fluctuation is tackled. The phenomenon at this situation conform to the analysis in Fig. 4-16(a).

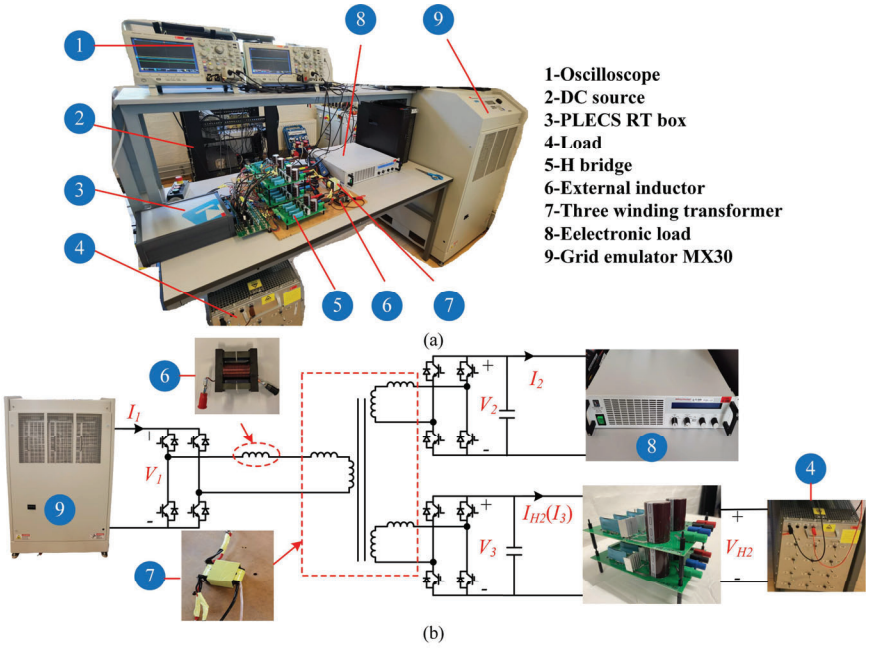

Figure 4-15 Lab prototype. [J2]

Table 4-3 The parameters of the experiment

Parameters	Value	Parameters	Value
Nominal voltage V_1 (V)	100	Nominal voltage $V_{2,3}$ (V)	50
External inductor (μH)	130	Leakage inductor L_{12} (μH)	5.27
Leakage inductor L_{13} (μH)	5.52	Leakage inductor L_{23}(μH)	3.31
System discrete step	1e-5	Winding turns ratio n_1:n_2:n_3	2:1:1
K_p in G_{con2} of TAB converter	4e-3	K_i in G_{con2} of TAB converter	1
K_p in G_{con3} of TAB converter	4e-3	K_i in G_{con3} of TAB converter	1
K_p in buck converter control	6e-4	K_i in buck converter control	0.5
K_p in boost converter control	6e-4	K_i in boost converter control	0.7

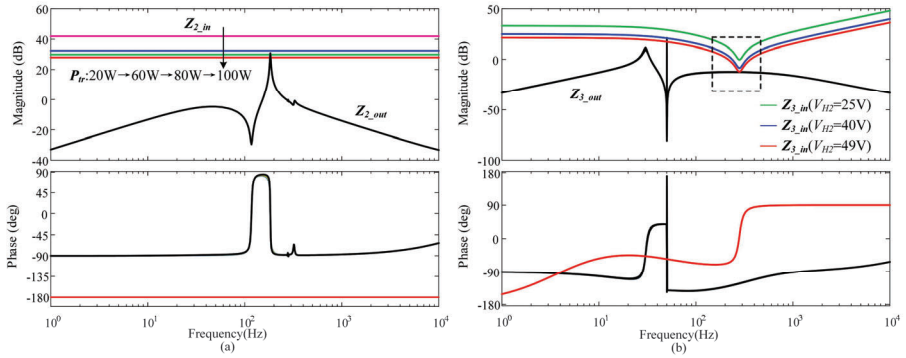

Figure 4-16 Impedance of case one. (a) Z_{2_in} as P_{tr} increases. (b) Z_{2_in} as V_{H2} increases. [J2]

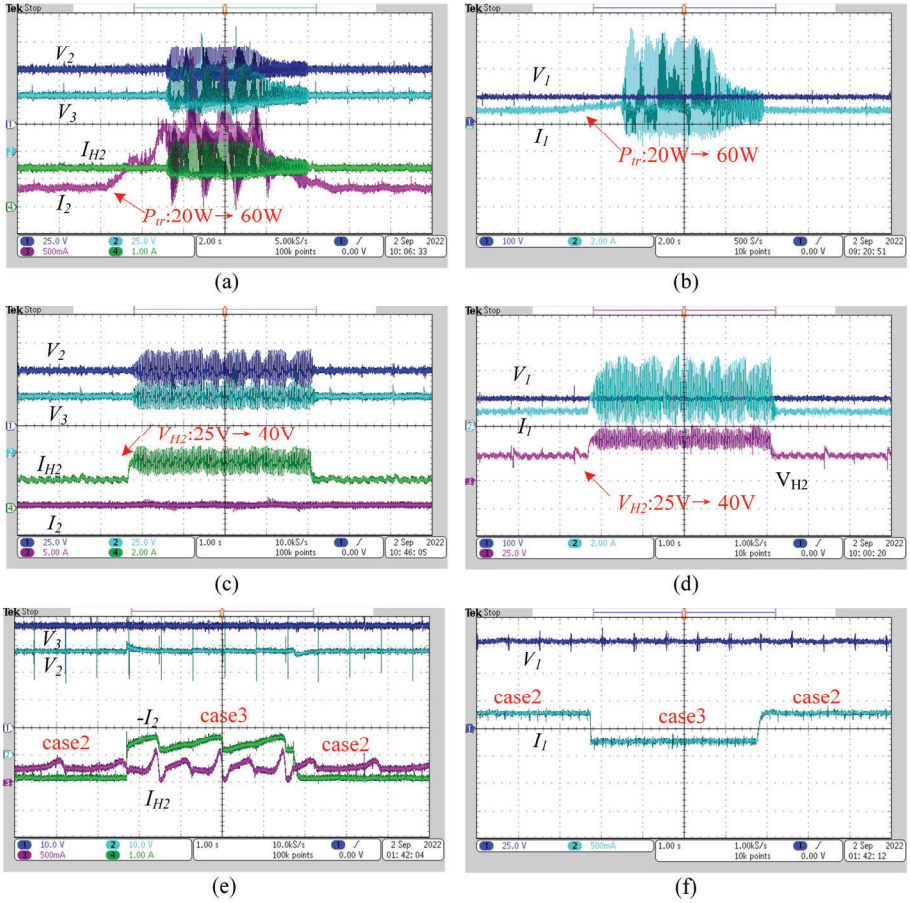

Figure 4-17 Experimental results. (a) Port2 and Port3 of situation one in case1. (b) Port1 of situation one in case1. (c) Port2 and Port3 of situation one in case1. (d) Port1 of situation one in case1. (e) Port2 and port3 in case2 and case3. (f) Port1 in case2 and case3. [J2]

Fig. 4-17(c) and (d) shows the voltage and current waveform of each port at situation two of case1. It is evident that the system operates stably when V_{H2} is set at 25V. The voltage and current at each port fluctuate as V_{H2} is boosted to 40V. The phenomenon in this situation conforms to the analysis in Fig. 4-14(c).

4.6. CONCLUSION

In this Chapter, the extra element theorem is novelty presented to derive the input and output impedance of the TAB converter. The progress of the derivation using EET is intuitive and concise. This method can also be applied for to the multi-port DC-DC converter including more than four ports. Furthermore, the stability of the system in this Chapter is evaluated by the impedance-based method. The DCTPS in traction state and hydrogen production systems are regarded as two CPLs. The simulation and experiment reveal the existence of voltage oscillation when two CPLs are connected. However, when DCTPS acting as constant power source feedbacks energy, the systems are stable.

CHAPTER 5. STABILITY ANALYSIS OF TAB CONVERTER WITH A SINGLE CPL

5.1. INTRODUCTION

In Chapter 4, the stability of the TAB converter connecting two CPLs is investigated. However, the situation that one load is CPL and another load is not CPL is not involved. In this Chapter, two situations are to be researched. One situation is that a resistor is connected to port3 and the TAB converter regulates the port3 voltage. Another situation is that a battery is connected to port3 and the TAB converter regulates the output current of port3. CPL is connected to port2 in both situations and the TAB converter regulates the port2 voltage. The stability of the two situations is evaluated by impedance method, where the EET is utilized to get the output impedance. Simulation and experiment have been conducted for validation.

5.2. SYSTEM DESCRIPTION

The structure of the systems is illustrated in Fig. 5-1, where a voltage source V_{bat} and resistor Z_{bat} are used to establish battery model at situation two. The small signal model is depicted in Fig. 5-2. G_{v2} is the voltage controller to maintain the port2 bus voltage. G_{v3} is the voltage controller to maintain the port3 bus voltage at situation one. G_{i3} is current controller to regulate the output current of port3. G_{L3} is the low pass filter for output current I_3.

5.3. OUTPUT IMPEDANCE OF SYSTEM OF DIFFERENT SITUATIONS

5.3.1. OUTPUT IMPEDANCE OF SITUATION ONE

It is necessary to obtain the unterminated output impedance of port2 before investigating the stability. For the situation one, according to the principle of KVL and KCL, the representation of voltage and current at port2 and port3 can be expressed by (5.1) and (5.2).

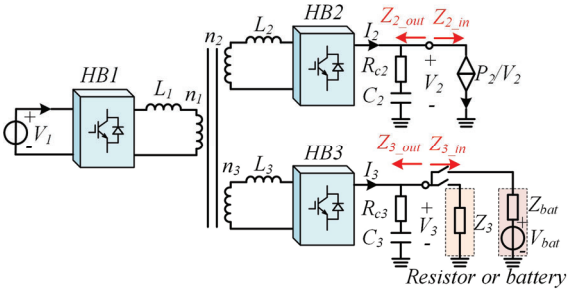

Figure 5-1 The structure of the systems. [C3]

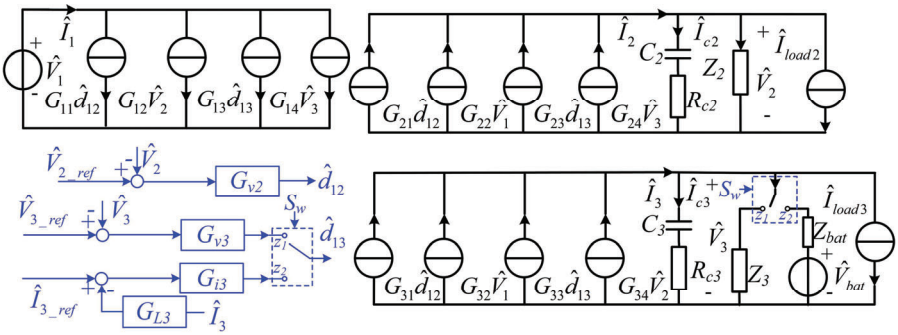

Figure 5-2 The small signal modelling of two situations. [C3]

$$\begin{cases} \hat{I}_2 = G_{21}\hat{d}_{12} + G_{22}\hat{V}_1 + G_{23}\hat{d}_{13} + G_{24}\hat{V}_3 \\ \left(\hat{I}_2 - \dfrac{\hat{V}_2}{Z_2} - \hat{I}_{load2}\right)\left(R_{c2} + \dfrac{1}{sC_2}\right) = \hat{V}_2 \\ \hat{d}_{12} = \left(\hat{V}_{2\_ref} - \hat{V}_2\right)G_{v2} = -\hat{V}_2 G_{v2} \end{cases} \tag{5.1}$$

$$\begin{cases} \hat{I}_3 = G_{31}\hat{d}_{12} + G_{32}\hat{V}_1 + G_{33}\hat{d}_{13} + G_{34}\hat{V}_2 \\ \left(\hat{I}_3 - \dfrac{\hat{V}_3}{Z_3} - \hat{I}_{load3}\right)\left(R_{c3} + \dfrac{1}{sC_3}\right) = \hat{V}_3 \\ \hat{d}_{13} = \left(\hat{V}_{3\_ref} - \hat{V}_3\right)G_{v3} = -\hat{V}_3 G_{v3} \end{cases} \tag{5.2}$$

The unterminated output impedance at port2 in situation one is given by (5.3).

$$Z_{2\_out}(s)=H_r(s)\frac{\left(1+\frac{Z_N^3(s)}{Z_3(s)}\right)}{\left(1+\frac{Z_D^3(s)}{Z_3(s)}\right)} \tag{5.3}$$

where the H_r(s) denotes the unterminated impedance disregarding the Z_2 and Z_3. H_r(s), Z_N^3(s) and Z_D^3(s) can be represented as (5.4)-(5.6), respectively.

$$\frac{1}{H_r(s)}=\frac{sC_2}{sC_2R_{c2}+1}+\frac{(G_{23}-G_{24})(G_{34}-G_{31}G_{v2})}{\frac{sC_3}{sR_{c3}C_3+1}+G_{33}G_{v3}}+G_{21}G_{v2} \tag{5.4}$$

$$\frac{1}{Z_D^3(s)}=\frac{sC_3}{sR_{c3}C_3+1}+\frac{(G_{31}G_{v2}-G_{34})(G_{24}-G_{23}G_{v3})}{\frac{sC_2}{sR_{c2}C_2+1}+G_{21}G_{v2}}+G_{33}G_{v3} \tag{5.5}$$

$$Z_N^3(s)=\frac{sC_3R_{c3}+1}{sC_3+G_{33}G_{v3}(sC_3R_{c3}+1)} \tag{5.6}$$

The terminated output impedance of port2 is represented as (5.7).

$$Z_{2\_out\_c}=Z_{2\_out}/(1+Z_{2\_out}/Z_2) \tag{5.7}$$

5.3.2. OUTPUT IMPEDANCE OF SITUATION TWO

In this situation, the voltage and current relationship at port3 formulated in (5.2) are changed to (5.8).

$$\begin{cases}\hat{I}_3=G_{31}\hat{d}_{12}+G_{32}\hat{V}_1+G_{33}\hat{d}_{13}+G_{34}\hat{V}_2\\ \left(\hat{I}_3-\frac{\hat{V}_3-\hat{V}_{bat}}{Z_{bat}}-\hat{I}_{load3}\right)\left(R_{c3}+\frac{1}{sC_3}\right)=\hat{V}_3\\ \hat{d}_{13}=\left(\hat{I}_{3\_ref}-G_{L3}\hat{I}_3\right)G_{i3}=-\hat{I}_3G_{L3}G_{i3}\end{cases} \tag{5.8}$$

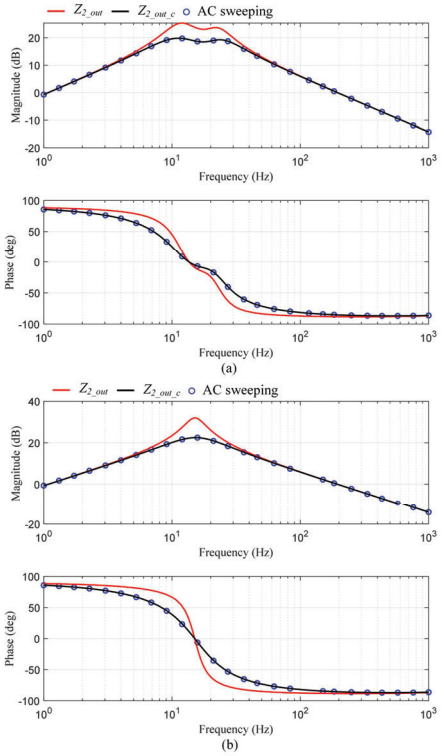

Figure 5-3 The unterminated and terminated impedance of port2. (a) Situation one. (b) Situation two. [C3]

Table 5-1 The systems parameters [C3]

Parameters	value	Parameters	value	Parameters	value
Bus voltage $V_{1\text{-}3}$ *(V)*	200	Inductor $L_{1,2,3}$ (μH)	50	Battery voltage V_{bat}(V)	195
Capacitor $C_{2,3}$ (μF)	820	Cap *ESR* $R_{c2,c3}$ (Ω)	0.01	Battery resistorZ_{bat} (Ω)	0.05
Winding turn n_1:n_2:n_3	1:1:1	Switching frequency	10kHz	Damping factor ζ	0.707
Current filter ω_c (rad/*s*)	0.01	Voltage controller $G_{v2,v3}$: 2e-4+0.1005/s			
Current controller G_{i3}: 0.01+2.5133/s					
Current filter: G_{L3}: $\omega_c^2/(s^2+2\omega_c\zeta s+\omega_c^2)$					

The unterminated output impedance of port2 at situation two is given by (5.9)

$$Z_{2\_out1}(s)=H_{r1}(s)\frac{\left(1+\frac{Z_{N1}^{3}(s)}{Z_{bat}(s)}\right)}{\left(1+\frac{Z_{D1}^{3}(s)}{Z_{bat}(s)}\right)} \tag{5.9}$$

The H_r(s), Z_N^3(s) and Z_D^3(s) can be represented as (5.10)-(5.12), respectively.

$$\begin{aligned}\frac{1}{H_{r1}(s)}=&\frac{sC_2}{sC_2R_{c2}+1}+G_{21}G_{v2}+G_{23}G_{L3}G_{i3}\cdot\frac{G_{34}-G_{31}G_{v2}}{1+G_{33}G_{L3}G_{i3}}\\&-G_{24}\left(\frac{G_{34}-G_{31}G_{v2}}{1+G_{33}G_{L3}G_{i3}}\right)/\left(\frac{sC_3}{sC_3R_{c3}+1}+\frac{1}{Z_{bat}}\right)\end{aligned} \tag{5.10}$$

$$\frac{1}{Z_{D1}^{3}(s)}=\frac{sC_3}{sR_{c3}C_3+1}+\frac{1}{Z_{bat}}-\frac{\frac{-G_{23}G_{L3}G_{i3}\left(G_{34}-G_{31}G_{v2}\right)}{\frac{sC_2}{sC_2R_{c2}+1}+G_{21}G_{v2}}}{1+G_{33}G_{L3}G_{i3}-\frac{G_{24}\left(G_{34}-G_{31}G_{v2}\right)}{\frac{sC_2}{sC_2R_{c2}+1}+G_{21}G_{v2}}} \tag{5.11}$$

$$Z_{N1}^{3}(s)=\frac{sC_3R_{c3}Z_{bat}+Z_{bat}}{sC_3\left(R_{c3}+Z_{bat}\right)+1} \tag{5.12}$$

Fig. 5-3(a) illustrates the comparison of unterminated impedance, terminated impedance and AC sweeping results of situation one, where Z_2 and Z_3 are 20Ω. Fig. 5-3(b) illustrates the comparison of situation two, the battery parameters are listed in Table 5-1. It is evident that the terminated output impedance is consistent with the AC sweeping results under these two situations.

5.4. STABILITY ANALYSIS OF DIFFERENT SITUATIONS

A. Situation one

The unterminated impedance of port2 of situation one is illustrated in Fig. 5-4(a). Two intersection points are presented when P_2 is 1050W and Z_3 is 500Ω. The left intersection occurs at a frequency of 13Hz, with a corresponding PM of -28 degrees. It signifies that the port 2 will exhibit instability issues by a 13Hz fluctuation under this situation.

.

While Z_3 is decreased from 500Ω to 20Ω, the amplitude of unterminated output impedance as depicted in Fig. 5-4(b) is significantly decreased. Thus, no intersection points are present, and the system would not oscillate.

Therefore, increasing the power dissipation of the resistor at port 3 can help eliminate oscillations that caused by the CPL at port2.

B. Situation two

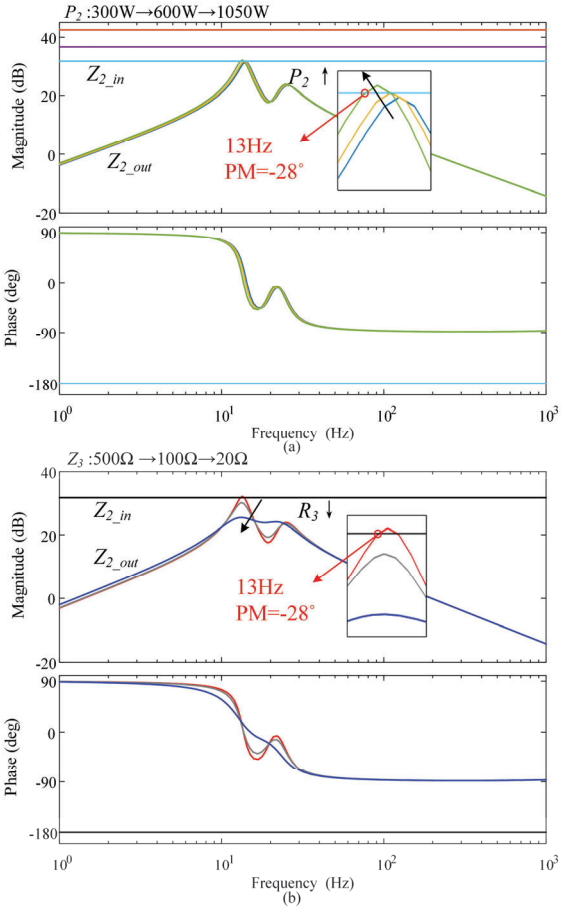

Figure 5-4 The impedance variation of situation one. (a) Z_{2_out} as P_2 increases. (b) Z_{2_out} as Z_3 decreases. [C3]

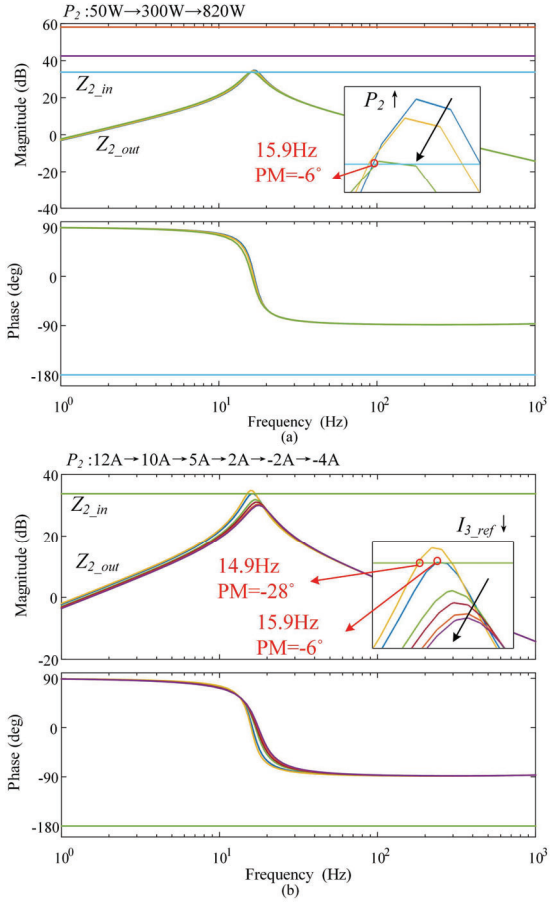

Figure 5-5 The impedance variation of situation two. (a) Z_{2_out} as P_2 increases. (b) Z_{2_out} as I_{3_ref} decreases. [C3]

Fig. 5-5(a) shows the impedance of Z_{2_out} and Z_{2_in} when I_{3_ref} is 10A. Two intersection points are presented when P_2 is 820W. The left intersection occurs at a frequency of 15.9Hz, with a corresponding PM of -6 degrees. It signifies that port 2 will exhibit instability issues by a 15.9Hz fluctuation under this situation. While the I_{3_ref} is gradually reduced to -4A, the amplitude of the unterminated output impedance as depicted in Fig. 5-5(b) is gradually decreased. No intersection points are presented. Thus, the system would be stable.

Therefore, decreasing the charging current of battery at port 3 or allowing battery to discharge can help eliminate oscillations that caused by the CPL at port2.

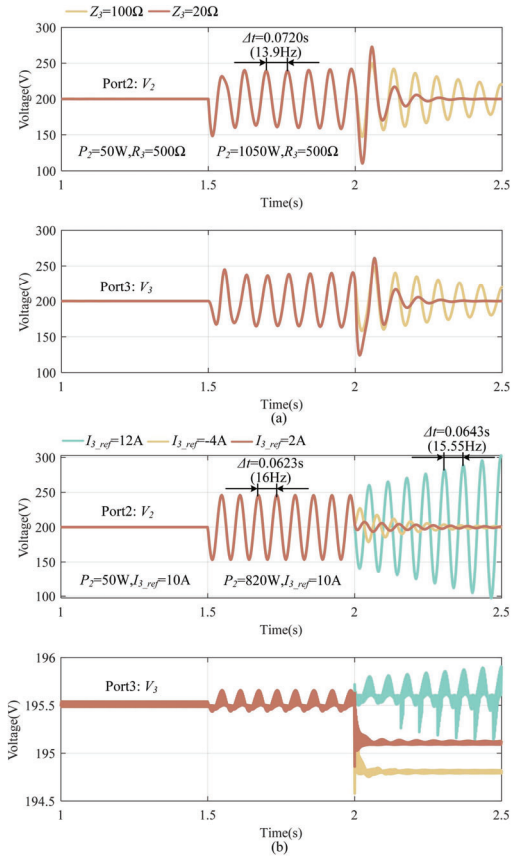

Figure 5-6 The simulation results. (a) situation one. (b) situation two. [C3]

5.5. SIMULATION AND EXPERIMENT TEST

A. Simulation verification

Fig. 5-6(a) illustrates the voltage waveform of situation one. At 1.5s, P_2 is changed to 1050W, and the voltage at port2 and port3 fluctuates with 13.9Hz, which is consistent with the theoretical analysis. While the Z_3 is changed to 100Ω and 20Ω at 2s, it is evident that the voltage at port2 and port3 restores stability.

Fig. 5-6(b) illustrates the voltage waveform of situation two. At 1.5s, P_2 is changed to 820W and I_{3_ref} is set at 10A. The voltage at port2 and port3 fluctuates with 16Hz, which is consistent with the theoretical analysis. While the I_{3_ref} is changed to 2A and -4A at 2s, it is evident that the voltage at port2 and port3 restores stability.

B. Experiment verification

The laboratory setup is shown in Fig. 5-7. A buck converter substitutes the CPL at port2 and a grid emulator substitutes the battery at port3. Table 5-2 gives the system parameters.

Fig. 5-8 illustrates the voltage and current waveform of the systems in situation one. The systems are stable at first, and the V_2 and V_3 are maintained at 50V. Also, the V_{buck_out} is kept at 40V. Once the power of buck converter is increased that I_{buck_out} found in Fig. 5-8(b) increases significantly, an observable low-frequency oscillation phenomenon occurs. Then, an additional resistor is added to port3 resulting in output current of port3 (I_{30}) increasing. It can be found that the oscillation disappears. The

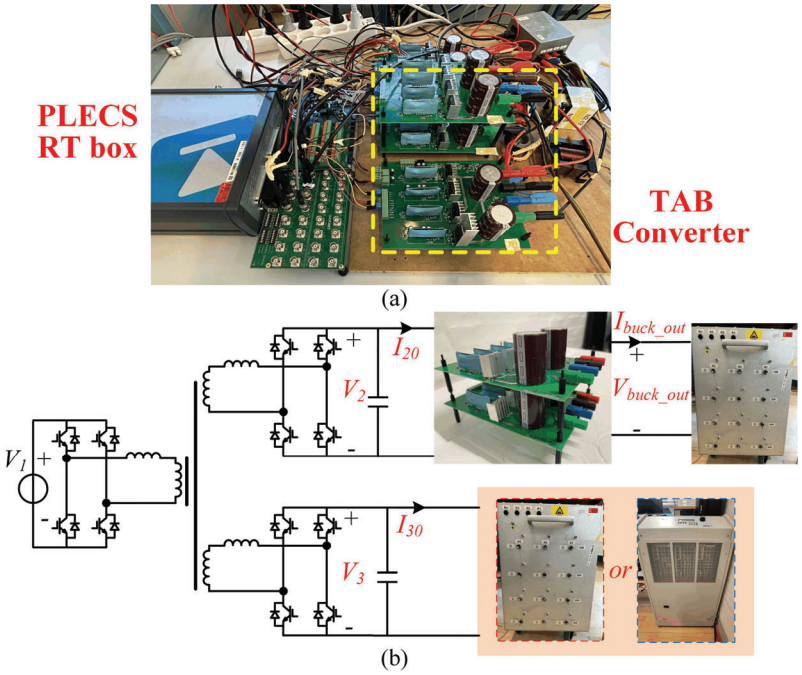

Figure 5-7 The laboratory prototypes. [C3]

Table 5-2 The parameters of the experimental prototype [C3]

Parameters	value	Parameters	value	Parameters	value
Bus voltage $V_{1\text{-}3}$ (V)	100	Inductor L_{12} (μH)	5.27	Inductor L_{12} (μH)	5.52
Inductor L_{12} (μH)	3.31	Bus voltage $V_{2,3}$ (V)	50	Capacitor (μF)	410
Winding turn n_1:n_2:n_3	1:1:1	Switching frequency	10kHz		
Current controller: G_{i3}: 1e-3+0.32/s					
Voltage controller: $G_{v2,v3}$: 2e-3+0.63/s					

results conform to the analysis in Fig. 5-4 and the simulation in Fig. 5-6(a).

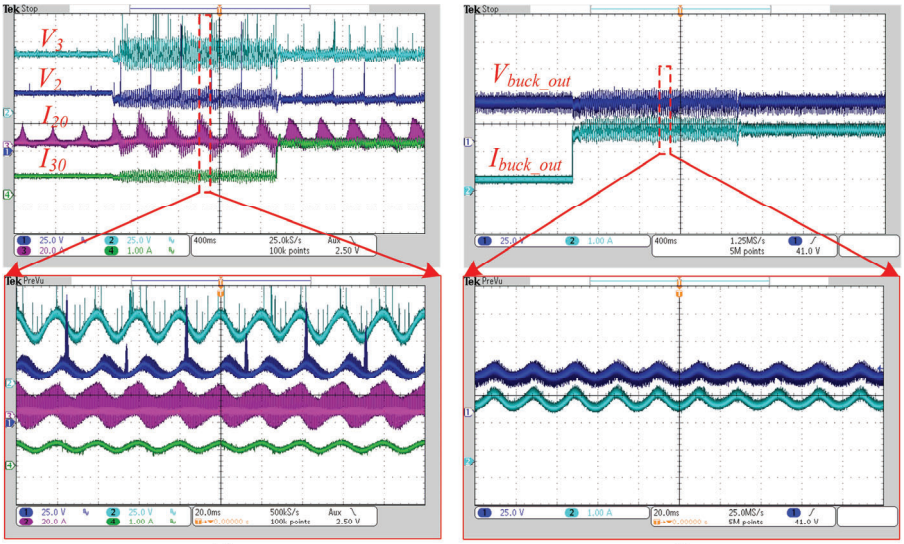

Figure 5-8 The voltage and current waveform of situation one. (a) The TAB converter. (b) The buck converter. [C3]

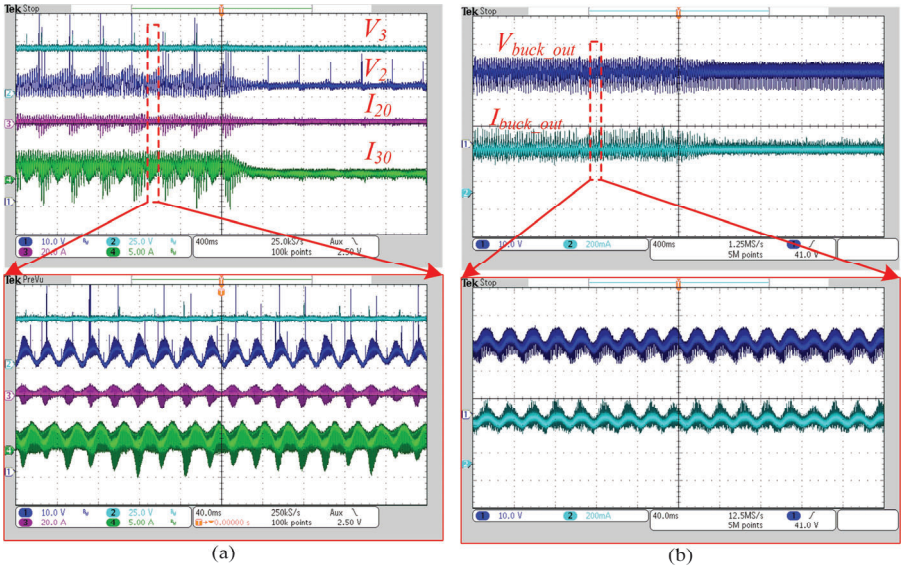

Figure 5-9 The voltage current waveform of situation two. (a) The TAB converter. (b) The buck converter. [C3]

Fig. 5-9 illustrates the voltage and current waveform of the systems in situation two. An observable low-frequency oscillation phenomenon occurs when I_{30} is 3A. Once the I_{30} is reduced to 1A, the oscillation disappears. The results conform to the analysis in Fig. 5-5 and the simulation in Fig. 5-6(b).

5.6. CONCLUSION

In this Chapter, the unterminated output impedance of TAB converter of two situations is derived by EET method. The impedance method is applied for theoretical stability analysis. By simulation and experiment test, it is found that increasing the power dissipation of the resistor in situation one can tackle the oscillation. Furthermore, it is found that decreasing battery charging current or allowing battery to discharge in situation two can tackle the oscillation.

CHAPTER 6. A VIRTUAL IMPEDANCE-BASED ACTIVE DAMPING CONTROL FOR TRIPLE ACTIVE BRIDGE CONVERTER WITH TWO CPLS

6.1. INTRODUCTION

In previous Chapters 4 and 5, the stability of the TAB converter with various types of loads and control is investigated. For the situation that the TAB converter connects with one CPL in Chapter 5, the stability can be improved by changing the operation state at another port. However, the solution to the situation that the TAB converter connects with two CPLs is not explored in Chapter 4. Virtual impedance (VI) control is the most widely applied form of active damping (AD) control. In this Chapter, a virtual impedance control is presented to tackle the oscillation issue, and the VI in this control has four different postions.

6.2. OUTPUT IMPEDANCE OF TAB CONVERTER WITH DUAL-LOOPS CONTROL

Fig. 6-1 and Fig. 6-2 show the circuit and small signal model of the TAB converter with two CPLs. A dual-loop control is executed to maintain the voltage of port2 and port3, which is illustrated in Fig. 6-3. The outer is a voltage loop and the inner is a current loop. The unterminated and terminated output impedance of TAB with this control method are given by (6.1) and (6.2).

$$Z_{2\_out}(s) = H_r(s)\frac{\left(1+\frac{Z_N^3(s)}{Z_3(s)}\right)}{\left(1+\frac{Z_D^3(s)}{Z_3(s)}\right)} \tag{6.1}$$

$$Z_{2\_out\_c}(s) = Z_{2\_out}(s)/\left(1+Z_{2\_out}(s)/Z_2(s)\right) \tag{6.2}$$

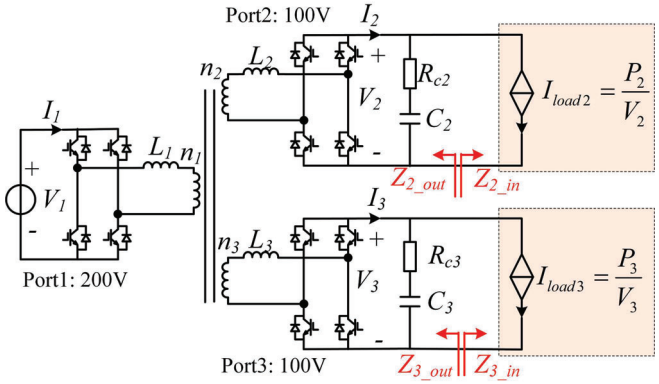

Figure 6-1 The circuit of TAB converter with two CPLs. [J3]

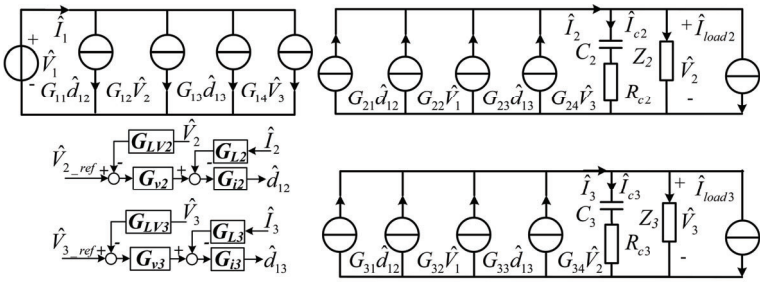

Figure 6-2 The small signal model of TAB converter with two CPLs. [J3]

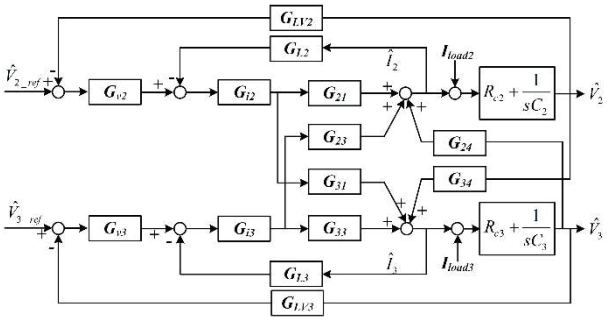

Figure 6-3 The dual-loops control diagram of TAB converter with two CPLs. [J3]

where Z_2 and Z_3 denotes the input impedance of loads. H_r(s) represents the inherent output impedance of port2 disregarding Z_2 and Z_3. It can be given by (6.3).

$$H_r(s) = 1/\left[\frac{sC_2}{sC_2R_{c2}+1} - \frac{a_3}{1-b_3}\right] \tag{6.3}$$

$$\begin{aligned} a_3 &= G_{24}a_1 - G_{21}G_{LV2}G_{v2}G_{i2} - G_{23}G_{LV3}G_{v3}G_{i3}a_1 - G_{23}G_{L3}G_{i3}a_2 \\ b_3 &= G_{24}b_1 - G_{21}G_{L2}G_{i2} - G_{23}G_{LV3}G_{v3}G_{i3}b_1 - G_{23}G_{L3}G_{i3}b_2 \end{aligned} \tag{6.4}$$

$$a_2 = \frac{sC_3}{sC_3R_{c3}+1}a_1; b_2 = \frac{sC_3}{sC_3R_{c3}+1}b_1 \tag{6.5}$$

$$a_1 = \frac{\frac{G_{34} - G_{31}G_{LV2}G_{v2}G_{i2}}{1+G_{33}G_{L3}G_{i3}}}{\frac{sC_3}{sC_3R_{c3}+1} + \frac{G_{33}G_{LV3}G_{v3}G_{i3}}{1+G_{33}G_{L3}G_{i3}}}; b_1 = \frac{\frac{-G_{31}G_{L2}G_{i2}}{1+G_{33}G_{L3}G_{i3}}}{\frac{sC_3}{sC_3R_{c3}+1} + \frac{G_{33}G_{LV3}G_{v3}G_{i3}}{1+G_{33}G_{L3}G_{i3}}} \tag{6.6}$$

Z_N^3 and Z_D^3 are null driving point impedance and driving point impedance at port3. Z_N^3 can be given by (6.7)

$$Z_N^3 = 1/\left(\frac{sC_3}{sC_3R_{c3}+1} + \frac{G_{33}G_{LV3}G_{v3}G_{i3}}{1+G_{33}G_{L3}G_{i3}}\right) \tag{6.7}$$

Z_D^3 can be given by (6.8).

$$Z_D^3 = 1/\left(\frac{sC_3}{sC_3R_{c3}+1} - \frac{e_5}{1-g_5}\right) \tag{6.8}$$

$$\begin{aligned} e_5 &= G_{34}e_3 - G_{31}G_{LV2}G_{v2}G_{i2}e_3 - G_{31}G_{L2}G_{i2}e_4 - G_{33}G_{LV3}G_{v3}G_{i3} \\ g_5 &= G_{34}g_3 - G_{31}G_{LV2}G_{v2}G_{i2}g_3 - G_{31}G_{L2}G_{i2}g_4 - G_{33}G_{L3}G_{i3} \end{aligned} \tag{6.9}$$

$$e_4 = \frac{sC_2}{sC_2R_{c2}+1}e_3; g_4 = \frac{sC_2}{sC_2R_{c2}+1}g_3 \tag{6.10}$$

$$e_3 = \frac{\frac{G_{24} - G_{23}G_{LV3}G_{v3}G_{i3}}{1+G_{21}G_{L2}G_{i2}}}{\frac{sC_2}{sC_2R_{c2}+1} + \frac{G_{21}G_{LV2}G_{v2}G_{i2}}{1+G_{21}G_{L2}G_{i2}}}; g_3 = \frac{\frac{-G_{23}G_{L3}G_{i3}}{1+G_{21}G_{L2}G_{i2}}}{\frac{sC_2}{sC_2R_{c2}+1} + \frac{G_{21}G_{LV3}G_{v2}G_{i2}}{1+G_{21}G_{L2}G_{i2}}} \tag{6.11}$$

The unterminated output impedance (Z_{3_out}) and terminated output impedance ($Z_{3\_out\_c}$) at port3 can also be derived by EET.

The AC sweeping results is shown in Fig. 6-4 where the load at port2 is a 20Ω resistor and the load at port3 is a 40Ω resistor. The AC sweeping results match well

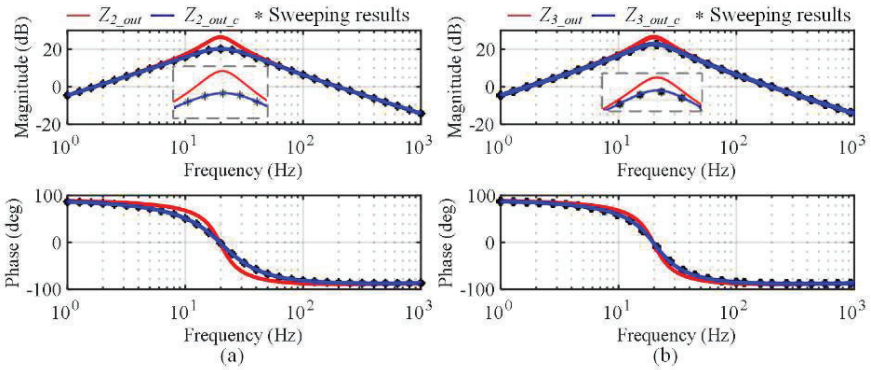

Figure 6-4 The unterminated and terminated impedance. (a) Port2. (b) Port3. [J3]

Table 6-1 The simulation parameters of the tab converter [J3]

Symbol	Quantity	Value
V_1	Nominal voltage of port1 (V)	200
$V_{2,3}$	Nominal voltage of port2 and port3 (V)	100
$L_{1,2,3}$	Leakage inductor of TAB converter (μH)	50
n_1:n_2:n_3	Windings turn ratio	2:1:1
$C_{2,3}$	Output capacitor (μF)	820
$R_{c2,c3}$	ESR of the output capacitor (Ω)	0.01
f_s	Switching frequency (kHz)	10
ω_c	Cut-off angular speed of current LPF (rad/s)	2π*1000
ω_{c1}	Cut-off angular speed of voltage LPF (rad/s)	2π*100
$G_{v2,3}$	Voltage controller	0.0806+10.63/s
$G_{i2,3}$	Current controller	0.0195+12.25/s
$G_{L2,3}$	Current LPF	$\omega_c^2/(s^2+2*s*0.707*\omega_c+\omega_c^2)$
$G_{LV2,3}$	Voltage LPF	$\omega_{c1}/(s+\omega_{c1})$

with the terminated output impedance, which demonstrates the accurancy of the output impedance.

6.3. THE VI CONTROL FOR THE TAB CONVERTER

The purpose of the VI control is to shift the unterminated output impedance. Four distinct plans are outlined, each corresponding to the different placements of virtual resistors. Fig. 6-5 shows the concept of different plans. In addition, the derivation of VI control is based on the H_r in (6.3).

A. Plan one of the VI control

Fig. 6-6 shows the control block diagram of plan one. The introduction of the virtual resistor Z_{vir1} brings an additional current. Thus, H_r in (6.3) can be given by (6.12).

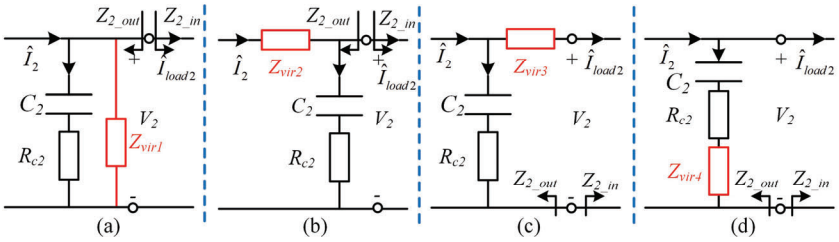

Figure 6-5 The different positions of VI. (a) Plan 1. (b) Plan 2. (c) Plan 3. (d) Plan 4. [J3]

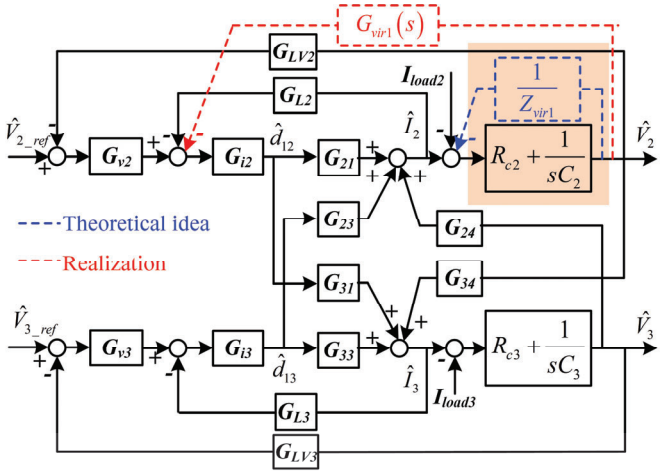

Figure 6-6 The VI control of plan one. [J3]

$$H_r^1(s)=1/\left[\frac{sC_2}{sC_2R_{c2}+1}+\frac{1}{Z_{vir1}}-\frac{a_3}{1-b_3}\right] \tag{6.12}$$

However, the theoretical idea illustrated as the blue dash line in Fig. 6-6 is not able to be achieved. Thus, the transfer function G_{vir1} serves to equivalently replace the theoretical idea, wherein the voltage is feedback to inner current loop, depicted as the red dashed line in Fig. 6-6. Then, the phase shifting ratio d_{12} and d_{13} can be given by (6.13).

$$\begin{aligned}\hat{d}_{12}&=\left(\left(\hat{V}_{2\_ref}-G_{LV2}\hat{V}_2\right)G_{v2}-G_{vir1}\hat{V}_2-G_{L2}\hat{I}_2\right)G_{i2}\\ \hat{d}_{13}&=\left(\left(\hat{V}_{3\_ref}-G_{LV3}\hat{V}_3\right)G_{v3}-G_{L3}\hat{I}_3\right)G_{i3}\end{aligned} \tag{6.13}$$

The expression for H_r^1(s) can be given by (6.14).

$$H_r^1(s)=1/\left[\frac{sC_2}{sC_2R_{c2}+1}-\frac{a_3^1}{1-b_3^1}\right] \tag{6.14}$$

where the $a_3{}^1$ and $b_3{}^1$ are represented as (6.15).

$$\begin{aligned} a_3^1 &= G_{24}a_1^1-G_{21}\left(G_{vir1}+G_{LV2}G_{v2}\right)G_{i2}-G_{23}G_{LV3}G_{v3}G_{i3}a_1^1-G_{23}G_{L3}G_{i3}a_2^1 \\ b_3^1 &= G_{24}b_1^1-G_{21}G_{L2}G_{i2}-G_{23}G_{LV3}G_{v3}G_{i3}b_1^1-G_{23}G_{L3}G_{i3}b_2^1 \end{aligned} \tag{6.15}$$

$$a_2^1=\frac{sC_3}{sC_3R_{c3}+1}a_1^1;b_2^1=\frac{sC_3}{sC_3R_{c3}+1}b_2^1 \tag{6.16}$$

$$a_1^1=\frac{\dfrac{G_{34}-G_{31}\left(G_{vir1}+G_{LV2}G_{v2}\right)G_{i2}}{1+G_{33}G_{L3}G_{i3}}}{\dfrac{sC_3}{sC_3R_{c3}+1}+\dfrac{G_{33}G_{LV3}G_{v3}G_{i3}}{1+G_{33}G_{L3}G_{i3}}};b_1^1=\frac{\dfrac{-G_{31}G_{L2}G_{i2}}{1+G_{33}G_{L3}G_{i3}}}{\dfrac{sC_3}{sC_3R_{c3}+1}+\dfrac{G_{33}G_{LV3}G_{v3}G_{i3}}{1+G_{33}G_{L3}G_{i3}}} \tag{6.17}$$

The denominator of (6.12) and (6.14) must be the same. Thus, the G_{vir1} can be obtained as (6.18).

$$G_{vir1}(s)=\frac{1-b_3^1}{Z_{vir1}\left[\left(G_{24}-G_{23}G_{LV3}G_{v3}G_{i3}-\dfrac{sC_3G_{23}G_{L3}G_{i3}}{sC_3R_{c3}+1}\right)\Delta n_1+G_{21}G_{i2}\right]} \tag{6.18}$$

where Δn_1 is given by (6.19).

$$\Delta n_1=\frac{G_{31}G_{i2}}{1+G_{33}G_{L3}G_{i3}}/\left(\frac{sC_3}{sC_3R_{c3}+1}+\frac{G_{33}G_{LV3}G_{v3}G_{i3}}{1+G_{33}G_{L3}G_{i3}}\right) \tag{6.19}$$

B. Plan two of the VI control

Fig. 6-7 shows the control block diagram of plan two. With the introduction of Z_{vir2}, the H_r in (6.3) can be modified as (6.20).

$$H_r^2(s)=1/\left[\frac{sC_2}{sC_2R_{c2}+1}-\frac{a_3}{1-b_3}\left(1+\frac{sC_2Z_{vir2}}{sC_2R_{c2}+1}\right)\right] \tag{6.20}$$

Similarly, the G_{vir2} can equivalently replace the theoretical idea. The output current I_2 is feedback to the current loop through G_{vir2}. Therefore, the $H_r{}^2$(s) can be given by (6.21).

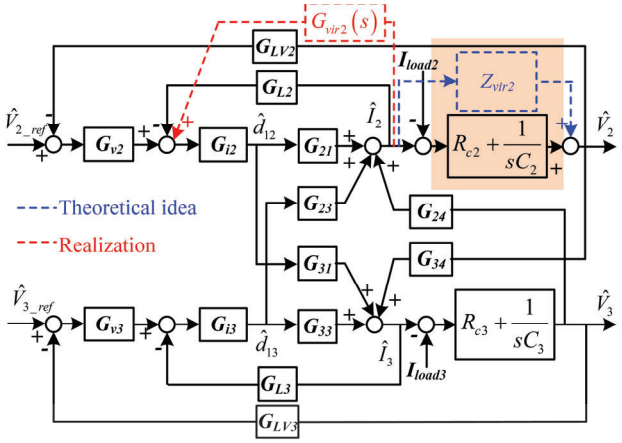

Figure 6-7 The VI control of plan two. [J3]

$$H_r^2(s)=1/\left[\frac{sC_2}{sC_2R_{c2}+1}-\frac{a_3^2}{1-b_3^2}\right] \tag{6.21}$$

$$\begin{aligned} a_3^2 &= G_{24}a_1^2-G_{23}G_{LV3}G_{v3}G_{i3}a_1^2-G_{23}G_{L3}G_{i3}a_2^2-G_{21}G_{LV2}G_{v2}G_{i2} \\ b_3^2 &= G_{24}b_1^2-G_{23}G_{LV3}G_{v3}G_{i3}b_1^2-G_{23}G_{L3}G_{i3}b_2^2-G_{21}(G_{L2}-G_{vir2})G_{i2} \end{aligned} \tag{6.22}$$

$$a_2^2=\frac{sC_3}{sC_3R_{c3}+1}a_1^2;b_2^2=\frac{sC_3}{sC_3R_{c3}+1}b_1^2 \tag{6.23}$$

$$a_1^2=\frac{\dfrac{G_{34}-G_{31}G_{LV2}G_{v2}G_{i2}}{1+G_{33}G_{L3}G_{i3}}}{\dfrac{sC_3}{sC_3R_{c3}+1}+\dfrac{G_{33}G_{LV3}G_{v3}G_{i3}}{1+G_{33}G_{L3}G_{i3}}};b_1^2=\frac{\dfrac{-G_{31}(G_{L2}-G_{vir2})G_{i2}}{1+G_{33}G_{L3}G_{i3}}}{\dfrac{sC_3}{sC_3R_{c3}+1}+\dfrac{G_{33}G_{LV3}G_{v3}G_{i3}}{1+G_{33}G_{L3}G_{i3}}} \tag{6.24}$$

The denominator of H_r^2 in (6.20) and (6.21) must be the same. Therefore, the G_{vir2} can be given by (6.25).

$$G_{vir2}(s)=(1-b_3)\cdot Z_{vir2}/\left[(Z_{vir2}+R_{c2}+1/sC_2)\cdot m_2\right] \tag{6.25}$$

$$m_2=\left(G_{24}-G_{23}G_{LV3}G_{v3}G_{i3}-G_{23}G_{L3}G_{i3}\frac{sC_2}{sC_2R_{c2}+1}\right)\Delta b_2+G_{21}G_{i2} \tag{6.26}$$

where Δn_2 is given by (6.27).

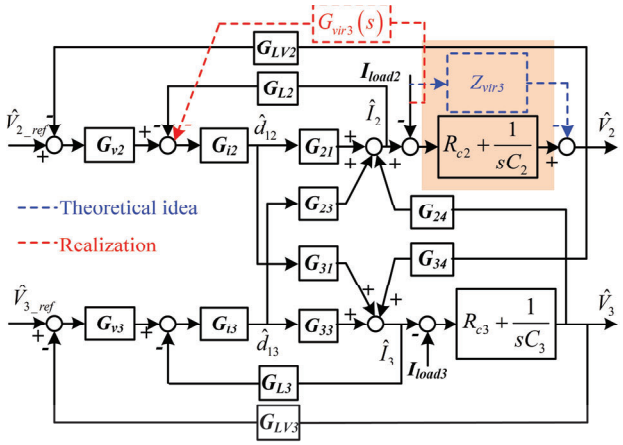

Figure 6-8 The VI control of plan three. [J3]

$$\Delta n_2 = \frac{-G_{31}G_{i2}}{1+G_{33}G_{L3}G_{i3}} \Big/ \left(\frac{sC_3}{sC_3R_{c3}+1} + \frac{G_{33}G_{LV3}G_{v3}G_{i3}}{1+G_{33}G_{L3}G_{i3}} \right) \tag{6.27}$$

C. *Plan three of the VI control*

Fig. 6-8 shows the control block diagram of plan three. With the introduction of Z_{vir3}, the H_r in (6.3) can be modified as (6.29).

$$H_r^3(s) = 1 \Big/ \left[\frac{sC_2R_{c2}+1}{sC_2\left(R_{c2}-Z_{vir3}\right)+1} \left(\frac{sC_2}{sC_2R_{c2}+1} - \frac{a_3}{1-b_3} \right) \right] \tag{6.29}$$

The transfer function G_{vir3} is used to equivalently replace the theoretical idea. The load current at port2 is feedback to the current loop through G_{vir3}, which is depicted as the red line in Fig. 6-8. Therefore, the H_r^3(s) can be given by (6.30).

$$H_r^3(s) = 1 \Big/ \left[\frac{1-b_3^3}{1-b_3^3-c_3^3} \left(\frac{sC_2}{sC_2R_{c2}+1} - \frac{a_3^3}{1-b_3^3} \right) \right] \tag{6.30}$$

$$\begin{cases} a_3^3 = G_{24}a_1^3 - G_{23}G_{LV3}G_{v3}G_{i3}a_1^3 - G_{23}G_{L3}G_{i3}a_2^3 - G_{21}G_{LV2}G_{v2}G_{i2} \\ b_3^3 = G_{24}b_1^3 - G_{23}G_{LV3}G_{v3}G_{i3}b_1^3 - G_{23}G_{L3}G_{i3}b_2^3 - G_{21}G_{L2}G_{i2} \\ c_3^3 = G_{24}c_1^3 - G_{23}G_{LV3}G_{v3}G_{i3}c_1^3 - G_{23}G_{L3}G_{i3}c_2^3 + G_{21}G_{vir3}G_{i2} \end{cases} \tag{6.31}$$

$$a_2^3 = \frac{sC_3}{sC_3R_{c3}+1}a_1^3; b_2^3 = \frac{sC_3}{sC_3R_{c3}+1}b_1^3; c_2^3 = \frac{sC_3}{sC_3R_{c3}+1}c_1^3 \tag{6.32}$$

$$
\begin{aligned}
a_1^3 &= \frac{G_{34}-G_{31}G_{LV2}G_{v2}G_{i2}}{1+G_{33}G_{L3}G_{i3}} \Big/ \left(\frac{sC_3}{sC_3R_{c3}+1}+\frac{G_{33}G_{LV3}G_{v3}G_{i3}}{1+G_{33}G_{L3}G_{i3}}\right) \\
b_1^3 &= \frac{-G_{31}G_{L2}G_{i2}}{1+G_{33}G_{L3}G_{i3}} \Big/ \left(\frac{sC_3}{sC_3R_{c3}+1}+\frac{G_{33}G_{LV3}G_{v3}G_{i3}}{1+G_{33}G_{L3}G_{i3}}\right) \\
c_1^3 &= \frac{G_{31}G_{vir3}G_{i2}}{1+G_{33}G_{L3}G_{i3}} \Big/ \left(\frac{sC_3}{sC_3R_{c3}+1}+\frac{G_{33}G_{LV3}G_{v3}G_{i3}}{1+G_{33}G_{L3}G_{i3}}\right)
\end{aligned}
\tag{6.33}
$$

Compared with the coefficient in (6.3) and (6.30), the a_1-a_3 and a_1^3-a_3^3 are identical. b_1-b_3 and b_1^3-b_3^3 are identical. The denominator of H_r^3 in (6.29) and (6.30) should be the same. Therefore, the G_{vir3} can be given by (6.34).

$$
G_{vir3}(s) = (1-b_3)\cdot Z_{vir3}\cdot sC_2 \Big/ \left[(sC_2R_{c2}+1)m_3\right] \tag{6.34}
$$

$$
m_3 = \left(G_{24}-G_{23}G_{LV3}G_{v3}G_{i3}-G_{23}G_{L3}G_{i3}\frac{sC_2}{sC_2R_{c2}+1}\right)\Delta n_3 + G_{21}G_{i2} \tag{6.35}
$$

where Δn_3 is represented as (6.36).

$$
\Delta n_3 = \frac{G_{31}G_{i2}}{1+G_{33}G_{L3}G_{i3}} \Big/ \left(\frac{sC_3}{sC_3R_{c3}+1}+\frac{G_{33}G_{LV3}G_{v3}G_{i3}}{1+G_{33}G_{L3}G_{i3}}\right) \tag{6.36}
$$

D. Plan four of the VI control

Fig. 6-9 shows the control block diagram of plan four. With the introduction of Z_{vir4}, which is depicted as the blue line in Fig. 6-9, the H_r in (6.3) can be modified as (6.37).

$$
H_r^4(s) = 1\Big/\left(\frac{sC_2}{sC_2\left(R_{c2}+Z_{vir\_c}\right)+1}-\frac{a_3}{1-b_3}\right) \tag{6.37}
$$

The G_{vir4} is used to equivalently replace the theoretical idea. The capacitor current at port2 is feedback to the current loop through G_{vir4}, which is depicted as the red dash line in Fig. 6-9. Therefore, the H_r^4(s) can be obtained as (6.38).

$$
H_r^3(s) = 1\Big/\left[\frac{1-b_3^4}{1-b_3^4-c_3^4}\left(\frac{sC_2}{sC_2R_{c2}+1}-\frac{a_3^4}{1-b_3^4}\right)\right] \tag{6.38}
$$

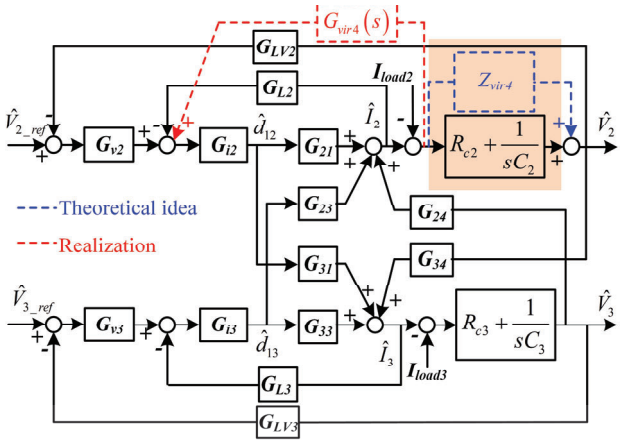

Figure 6-9 The VI control of plan four. [J3]

$$\begin{cases} a_3^4 = \left(G_{24} - G_{23}G_{LV3}G_{v3}G_{i3}\right)a_1^4 - G_{23}G_{L3}G_{i3}a_2^4 - G_{21}G_{LV2}G_{v2}G_{i2} \\ b_3^4 = \left(G_{24} - G_{23}G_{LV3}G_{v3}G_{i3}\right)b_1^4 - G_{23}G_{L3}G_{i3}b_2^4 - G_{21}\left(G_{L2} - G_{vir4}\right)G_{i2} \\ c_3^4 = \left(G_{24} - G_{23}G_{LV3}G_{v3}G_{i3}\right)c_1^4 - G_{23}G_{L3}G_{i3}c_2^4 - G_{21}G_{vir4}G_{i2} \end{cases} \quad (6.39)$$

$$a_2^4 = \frac{sC_3}{sC_3R_{c3}+1}a_1^4; b_2^4 = \frac{sC_3}{sC_3R_{c3}+1}b_1^4; c_2^4 = \frac{sC_3}{sC_3R_{c3}+1}c_1^4 \quad (6.40)$$

$$\begin{aligned} a_1^4 &= \frac{G_{34} - G_{31}G_{LV2}G_{v2}G_{i2}}{1+G_{33}G_{L3}G_{i3}} \Big/ \left(\frac{sC_3}{sC_3R_{c3}+1} + \frac{G_{33}G_{LV3}G_{v3}G_{i3}}{1+G_{33}G_{L3}G_{i3}}\right) \\ b_1^4 &= \frac{-G_{31}\left(G_{L2} - G_{vir4}\right)G_{i2}}{1+G_{33}G_{L3}G_{i3}} \Big/ \left(\frac{sC_3}{sC_3R_{c3}+1} + \frac{G_{33}G_{LV3}G_{v3}G_{i3}}{1+G_{33}G_{L3}G_{i3}}\right) \end{aligned} \quad (6.41)$$

$$c_1^4 = \frac{-G_{31}G_{vir4}G_{i2}}{1+G_{33}G_{L3}G_{i3}} \Big/ \left(\frac{sC_3}{sC_3R_{c3}+1} + \frac{G_{33}G_{LV3}G_{v3}G_{i3}}{1+G_{33}G_{L3}G_{i3}}\right) \quad (6.42)$$

Compared with the coefficient of H_r in (6.3)-(6.6) and the coefficient of H_r^4 in (6.38)-(6.42), the G_{vir4} can be obtained as (6.43).

$$G_{vir3}(s) = \left(1-b_3\right)sC_2Z_{vir4} \Big/ \left[\left(sC_2R_{c2} + sC_2Z_{vir4} + 1\right)m_4\right] \quad (6.43)$$

$$m_4 = \left(G_{24} - G_{23}G_{LV3}G_{v3}G_{i3} - G_{23}G_{L3}G_{i3}\frac{sC_2}{sC_2R_{c2}+1}\right)\Delta n_4 + G_{21}G_{i2} \quad (6.44)$$

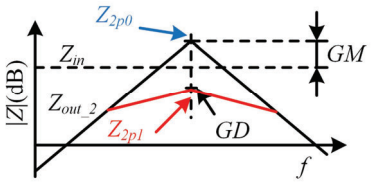

Figure 6-10 The output impedance with plan one of the AD controls. [J3]

where Δn_4 is given by (6.45).

$$\Delta n_4 = \frac{G_{31}G_{i2}}{1+G_{33}G_{L3}G_{i3}} \Big/ \left(\frac{sC_3}{sC_3R_{c3}+1} + \frac{G_{33}G_{LV3}G_{v3}G_{i3}}{1+G_{33}G_{L3}G_{i3}} \right) \tag{6.45}$$

E. The region of VI

Fig. 6-10 shows the unterminated output impedance of plan one of VI control. Z_{2p0} denotes the maximum value of initial output impedance and Z_{2p1} denotes the maximum value of output impedance with plan one. GD denotes the gain difference between Z_{2p0} and Z_{2p1}. GM denotes the gain margin. The Z_{2p1} must be lower than Z_{in}. Thus, Z_{vir1} can be given by (6.46).

$$\frac{V_2^2}{P_{2m}} < Z_{vir1} < \left(\frac{V_2^2}{P_2} \right) \Big/ \left(1 - \frac{1}{10^{\frac{GM}{20}}} \right) \tag{6.46}$$

where P_{2m} denotes the maximum power of port2.

For plan three, the Z_{vir3} should satisfy the following inequality (6.48).

$$Z_{2p0} - |Z_{vir3}| < |Z_{in}| \Rightarrow |Z_{vir3}| > \frac{V_2^2}{P_2} \left(10^{\frac{GM}{10}} - 1 \right) \tag{6.47}$$

$$\frac{V_2^2}{P_{2m}} > |Z_{vir3}| > \frac{V_2^2}{P_2} \left(10^{\frac{GM}{20}} - 1 \right) \tag{6.48}$$

Furthermore, the right item of the inequality (6.48) should be greater than the left item.

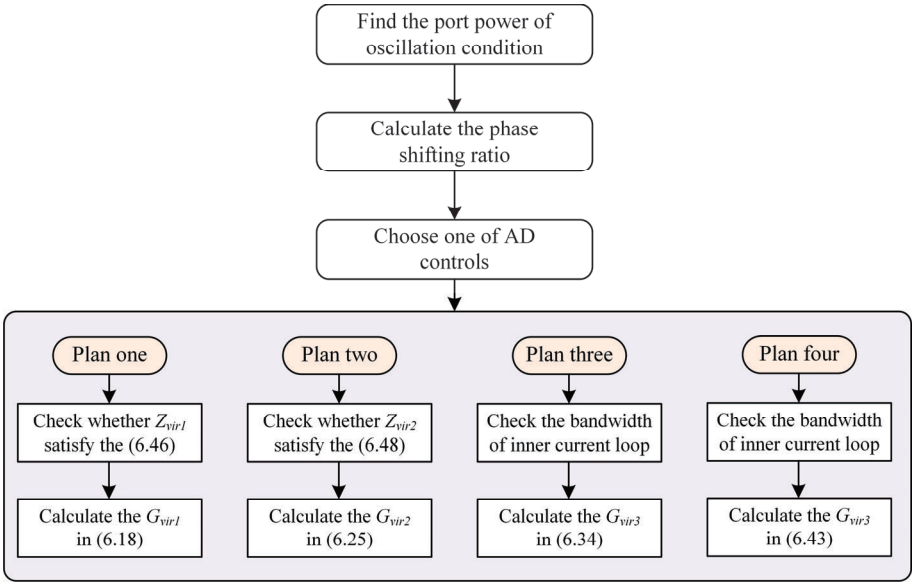

Figure 6-11 The flowing of the proposed AD control.

For plan two and four, the derivation of G_{vir2} and G_{vir4} are both determined by the current I_2. The increasing of the Z_{vir2} and Z_{vir4} would reduce the bandwidth of the inner current loop. When it is reduced to 100Hz that equals the cut-off frequency of voltage LPF in Table 6-1, the system would be unstable.

Fig. 6-11 shows the flow of VI control design. The step is to know the transfer power of each port when oscillation happens. Then, the phase shifting ratio of TAB converter under steady state can be calculated. Next, choose one of the proposed plans of VI controls. Then, the equivalent transfer function G_{vir} can be obtained.

6.4. SIMULATION VERIFICATION

In this section, simulation is given for validation. Table 6-2 shows the $G_{vir1\text{-}4}$ in different plans, which is reduced to a second-order transfer function.

Fig. 6-12(a1) shows the unterminated output impedance with different virtual resistor values when plan one of the VI controls is implemented. Two intersection points are observed when P_2 is set at 480W and P_3 is 400W. The left intersection occurs at a frequency of 19.5 Hz, with a corresponding PM of -2 degrees. It signifies that the systems will exhibit instability issues by a 37.8Hz fluctuation. While plan one is enabled and Z_{vir1} is decreased from 50Ω to 10Ω, the amplitude of unterminated output impedance is reduced, thereby restoring the system stability. The voltage waveform of plan one is illustrated in Fig. 6-12(a2). P_2 is increased to 480W at 2s and the voltage at port2 and port3 fluctuates. The oscillation frequency

Table 6-2 The $G_{vir}(s)$ of different plans in simulation [J3]

	$G_{vir}(s)$
1	$G_{vir1}\|_{Z=100} = \frac{1.957e^{-4}s^2 + 58.26s + 3.617e^4}{s^2 + 4127s + 3.617e^6}$; $G_{vir1}\|_{Z=50} = \frac{3.915e^{-4}s^2 + 116.5s + 7.235e^4}{s^2 + 4127s + 3.617e^6}$
	$G_{vir1}\|_{Z=20} = \frac{9.787e^{-4}s^2 + 291.3s + 1.809e^5}{s^2 + 4127s + 3.617e^6}$; $G_{vir1}\|_{Z=10} = \frac{1.957e^{-3}s^2 + 582.6s + 3.617e^5}{s^2 + 4127s + 3.617e^6}$
2	$G_{vir2}\|_{Z=1} = \frac{0.05514s^2 + 5207s + 3.001e^{-6}}{s^2 + 4016s + 5.786e^6}$; $G_{vir2}\|_{Z=4} = \frac{-0.07888s^2 + 7182s + 9.172e^{-9}}{s^2 + 5224s + 2.336e^6}$
	$G_{vir2}\|_{Z=7} = \frac{-0.1668s^2 + 8581s + 2.217e^{-7}}{s^2 + 6547s + 1.664e^6}$; $G_{vir2}\|_{Z=9} = \frac{-0.2089s^2 + 9324s + 2.306e^{-7}}{s^2 + 6943s + 1.531e^6}$
3	$G_{vir3}\|_{Z=-1} = \frac{-23.17s^2 - 1.036e^6s + 0.07368}{s^2 + 2.137e^5s + 9.331e^8}$; $G_{vir3}\|_{Z=-5} = \frac{-115.8s^2 - 5.181e^6s + 0.4805}{s^2 + 2.137e^5s + 9.331e^8}$
	$G_{vir3}\|_{Z=-7} = \frac{-162.2s^2 - 7.254e^6s + 0.6781}{s^2 + 2.137e^5s + 9.331e^8}$; $G_{vir3}\|_{Z=-10} = \frac{-231.7s^2 - 1.036e^7s + 0.9612}{s^2 + 2.137e^5s + 9.331e^8}$
4	$G_{vir4}\|_{Z=1} = \frac{0.0552s^2 + 5207s + 8.642e^{6}}{s^2 + 4015s + 5.786e^6}$; $G_{vir4}\|_{Z=3} = \frac{-0.04044s^2 + 6621s - 5.768e^{6}}{s^2 + 4756s + 2.787e^6}$
	$G_{vir4}\|_{Z=5} = \frac{-0.1122s^2 + 7692s + 5.946e^{-8}}{s^2 + 5684s + 2.041e^6}$; $G_{vir4}\|_{Z=7} = \frac{-0.1668s^2 + 8582s - 7.195e^{-8}}{s^2 + 6546s + 1.664e^6}$

is 19.6Hz which is consistent with the analysis. When different virtual resistors of plan one is implemented, it is evident that the oscillation can be effectively tackled. The step response considering the effect of plan one is illustrated in Fig. 6-12(a3). It reflects that as Z_{vir1} decreases, the rising time of port2 increases. But the overshoot of port2 voltage is reduced. When Z_{vir1} is 5Ω, port2 voltage cannot recover to 100V. Meanwhile, G_{vir1} has no impact on port3.

Fig. 6-12(b1) shows the unterminated output impedance with different virtual resistor values when plan two of the VI controls is implemented. When plan two is enabled and Z_{vir2} is increased from 1Ω to 4Ω, the amplitude of unterminated output impedance is reduced, thereby restoring the system stability. The voltage waveform is shown in Fig. 6-12(b2). When different virtual resistors of plan two is implemented at 3s, it is evident that the oscillation can be effectively tackled. However, the voltage oscillates again when Z_{vir2} is 7Ω and 9Ω. The step response considering the effect of plan two is illustrated in Fig. 6-12(b3). It shows that the overshoot of port2 voltage is improved when Z_{vir2} is 1Ω and 4Ω. When Z_{vir2} is 7Ω and 9Ω, the voltage oscillates again, consequently causing oscillations at port3 as well.

Fig. 6-12(c1) the unterminated output impedance with different virtual resistor values when plan three of the VI controls is implemented. When plan three is implemented and the Z_{vir3} is decreased from -1Ω to -5Ω, the amplitude of unterminated output impedance is reduced, which indicates that the system restore stability. The voltage waveform is shown in Fig. 6-12(c2). When different virtual resistors of plan three is implemented at 3s, it is evident that the oscillation can be effectively tackled. However, it oscillates again when Z_{vir2} is -7Ω and -10Ω. The

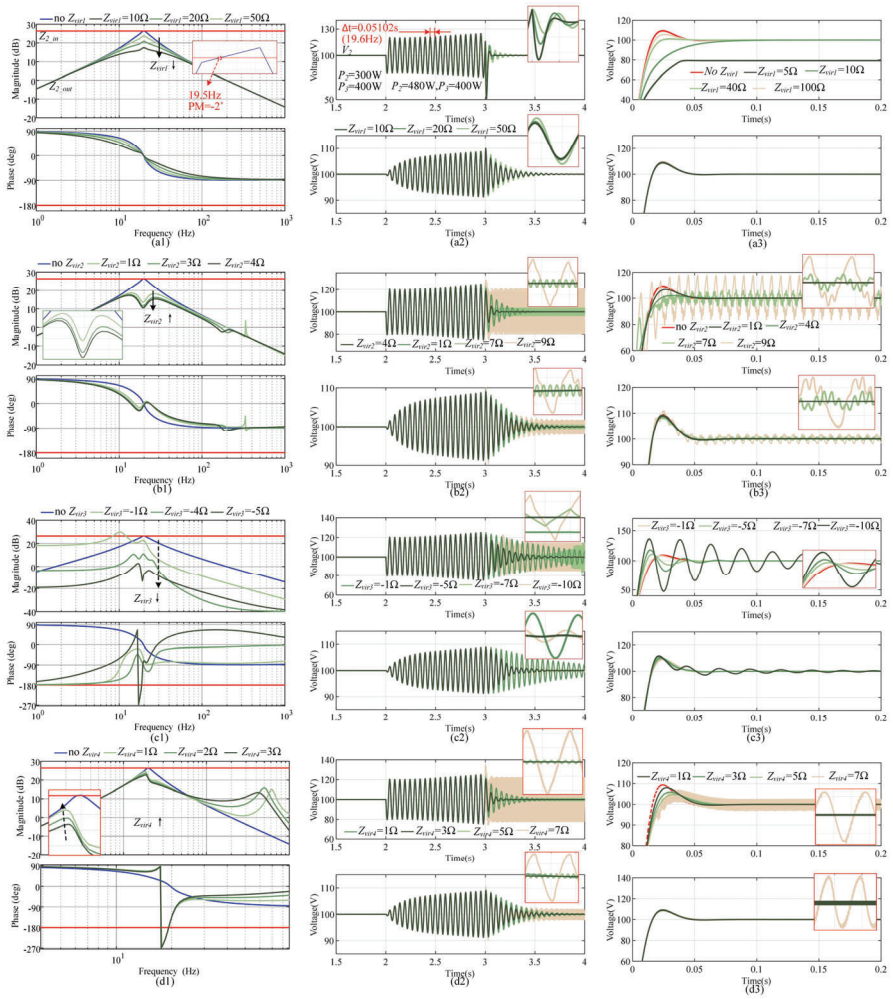

Figure 6-12 The simulation of VI control. (a1) impedance of plan one. (a2) Voltage of plan one. (a3) Step response of plan one. (b1) impedance of plan two. (b2) voltage of plan two. (b3) Step response of plan two. (c1) impedance of plan three. (c2) Voltage of plan three. (c3) Step response of plan three. (d1) impedance of plan four. (d2) voltage of plan four. (d3) Step response of plan four [J3]

amplitude of oscillation when Z_{vir2} is -10Ω is much higher than when Z_{vir2} is -7Ω. The step response considering the effect of plan three is illustrated in Fig. 6-12(c3). The rising time of step response decreases when Z_{vir3} is decreased from -1Ω to -10Ω. But overshoot of port2 voltage increases. Also, the step response of port3 voltage has the same trend as port2 voltage.

Fig. 6-12(d1) shows the unterminated output impedance with different virtual resistor values when plan four of the VI controls is implemented. The amplitude of output impedance increases when the Z_{vir4} is increased from 1Ω to 3Ω. But no intersection points are presented. The voltage waveform is shown in Fig. 6-12(d2). When different virtual resistors of plan four is implemented at 3s, it is evident that the oscillation can be effectively tackled. However, the voltage oscillates again when Z_{vir4} is 5Ω and 7Ω. The amplitude of oscillation when Z_{vir2} is 7Ω is much higher than when Z_{vir2} is 5Ω. The step response considering the effect of plan four is illustrated in Fig. 6-12(d3). The rising time of step response of port2 increases as Z_{vir4} is increased from1Ω to 3Ω. When Z_{vir4} is 5Ω and 7Ω, the voltage will oscillate, consequently causing oscillations at port3 as well.

6.5. EXPERIMENT VERIFICATION

Fig. 6-13 shows the laboratory setup and equivalent circuit. The CPL at port2 and port3 is emulated by a buck converter. Table 6-3 lists the systems parameters. Fig. 6-14 illustrates the voltage and current information of at each port. An 80Ω resistor is connected to the buck converter at port2 and port3, and the system is stable. While

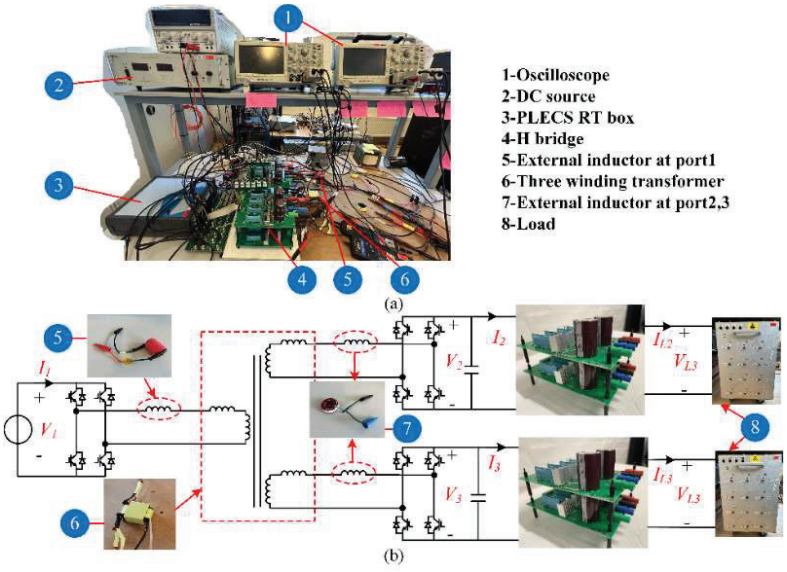

Figure 6-13 The laboratory setup. (a) laboratory prototype. (b) equivalent circuit. [J3]

Table 6-3 Main parameters of laboratory setup [J3]

Parameters	Value	Parameters	Value
Nominal voltage V_1 (V)	100	Nominal voltage $V_{2,3}$ (V)	50
External inductor L_{e1} (μH)	40	External inductor $L_{e2,3}$ (μH)	120
Leakage inductor L_{12} (μH)	5.27	Leakage inductor L_{13} (μH)	5.52
Leakage inductor L_{23}(μH)	3.31	Output capacitor $C_{2,3}$ (μF)	2000
System discrete step	1e-5	Winding turns ratio n_1:n_2:n_3	2:1:1
$G_{v2,3}$ voltage controller of TAB			0.1+5.024/s
$G_{i2,3}$ voltage controller of TAB			0.01+0.314/s
G_{buck2} voltage controller of buck converter at port2			0.005+0.5652/s
G_{buck3} voltage controller of buck converter at port2			0.0005+0.05652/s

Table 6-4 The G_{vir}(s) of different plans of VI control [J3]

	G_{vir}(s)
1	$G_{vir1}\big\|_{Z=66.7}=\dfrac{0.02089s^2+2.884s+67.34}{s^2+53.2s+4489}$; $G_{vir1}\big\|_{Z=46.5}=\dfrac{0.02995s^2+5.566s+96.5}{s^2+53.2s+4489}$ $G_{vir1}\big\|_{Z=40}=\dfrac{0.03483s^2+6.473s+112.2}{s^2+53.2s+4489}$
2	$G_{vir2}\big\|_{Z=3}=\dfrac{1.05s^2+576.2s-4.239e^{-7}}{s^2+199.7s+3.644e^4}$; $G_{vir2}\big\|_{Z=10}=\dfrac{1.39s^2+411.1s-1.796e^{-7}}{s^2+100.4s+1.138e^4}$ $G_{vir2}\big\|_{Z=80}=\dfrac{0.8999s^2+530.3s-4.954e^{-8}}{s^2+121.8s+5541}$
3	$G_{vir3}\big\|_{Z=-5}=\dfrac{-292.7s^2-8.462e^5s+0.0252}{s^2+5.387e^4s+2.647e^7}$; $G_{vir3}\big\|_{Z=-20}=\dfrac{-1171s^2-3.385e^6s-0.1009}{s^2+5.387e^4s+2.647e^7}$ $G_{vir3}\big\|_{Z=-60}=\dfrac{-3512s^2-1.015e^7s+0.2058}{s^2+5.387e^4s+2.647e^7}$;
4	$G_{vir4}\big\|_{Z=3}=\dfrac{1.05s^2+576.2s-3.761e^{-8}}{s^2+199.7s+3.644e^4}$; $G_{vir4}\big\|_{Z=10}=\dfrac{1.39s^2+411.1s+6.726e^{-7}}{s^2+100.4s+1.138e^4}$ $G_{vir4}\big\|_{Z=100}=\dfrac{0.823s^2+557.7s-2.741e^{-7}}{s^2+129.9s+5483}$

the resistor at port2 is changed to 26.7 Ω, the low-frequency oscillation occurs, and the frequency is 3Hz.

Fig. 6-15 (a1)-(a3) illustrate the voltage and current waveform of plan one. The G_{vir}(s) of different plans are given in Table 6-4. The oscillation cases when Z_{vir1} of 66.7Ω is implemented. The oscillation will disappear faster when Z_{vir1} is 46.5Ω. However, the port2 voltage cannot be kept at 50V when the Z_{vir1} is changed to 40Ω. It consistent with the analysis in Fig. 6-12.

Fig. 6-15 (b1)-(b3) illustrate the voltage and current waveform of plan two. It is evident that the oscillation cases when Z_{vir1} of 3Ω and 10Ω is implemented. While the Z_{vir2} is increased to 80Ω, the port2 voltage will oscillate again. It consistent with the analysis in Fig. 6-12.

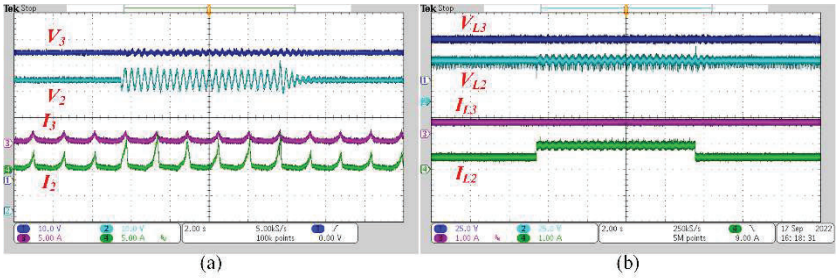

Figure 6-14. Oscillation analysis in experiment. (a) voltage and current of TAB converter. (b) voltage and current of buck converter. (c) impedance characteristics of port2. [J3]

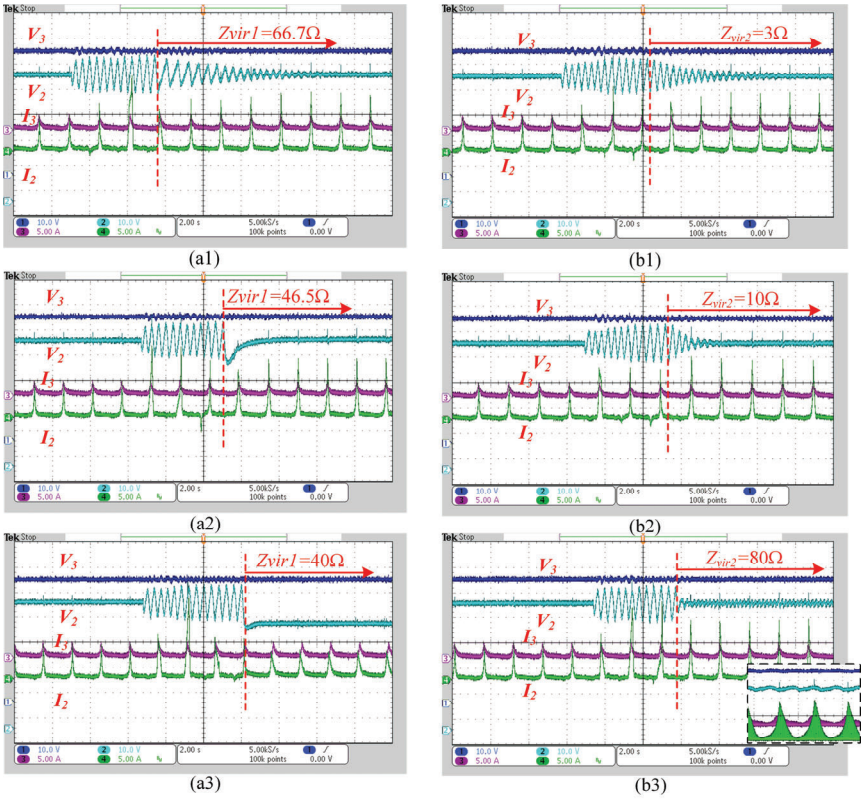

Figure 6-15 The voltage and current waveform of plan one and plan two. (a1) Z_{vir1}=66.7Ω. (a2) Z_{vir1}=46.5Ω. (a3) Z_{vir1}=40Ω. (b1) Z_{vir2}=3Ω. (b2) Z_{vir2}=10Ω. (b3) Z_{vir2}=80Ω. [J3]

Fig. 6-16 (a1)-(a3) illustrate the voltage and current waveform of plan three. It is evident that the oscillation issue disappears when Z_{vir2} is set at -5Ω. However, when Z_{vir3} is decreased to -20Ω that exceeds the region of (6.48), the port2 voltage will

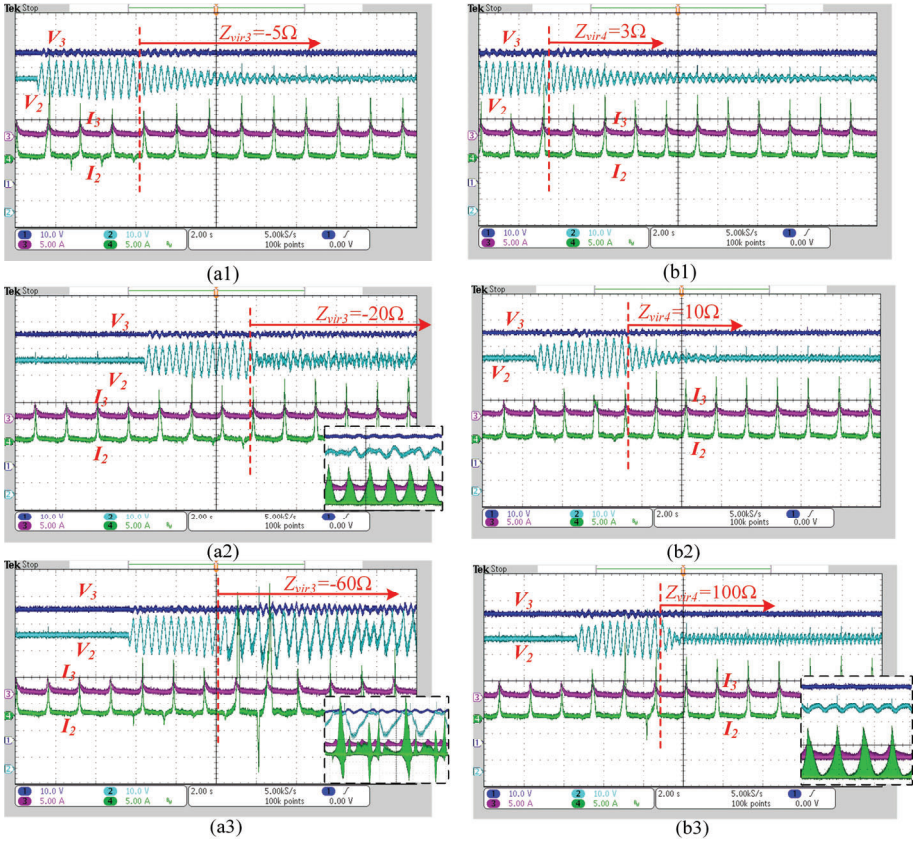

Figure 6-16 The voltage and current waveform of plan three and plan four. (a1) Z_{vir3}=-5Ω. (a2) Z_{vir3}=-20Ω. (a3) Z_{vir3}=-60Ω. (b1) Z_{vir4}=3Ω. (b2) Z_{vir4}=10Ω. (b3) Z_{vir4}=100Ω. [J3]

oscillate irregularly. When Z_{vir3} is decreased to -60Ω. The vibration amplitude will increase significantly. It consistent with the analysis in Fig. 6-12.

Fig. 6-16 (b1)-(b3) illustrate the voltage and current waveform of plan four. It is evident that the oscillation issue disappears when Z_{vir4} are set at 3Ω and 10Ω. While the Z_{vir4} is increased to 100Ω, the port2 voltage will oscillate again. It consistent with the analysis in Fig. 6-12.

6.6. CONCLUSION

In this Chapter, a virtual impedance control is presented to suppress the instability problem when TAB converter connects with two CPLs. The virtual impedance has four different positions at port2 capacitor. Derivation for the equivalent transfer function of different plans is elaborated. When the virtual impedance of different

plan is set within the reasonable region, the oscillation issue can be effectively eliminated. Plan one that the virtual impedance is added parallel to the port2 has the most advantage, since the port voltage would not be oscillate again as the virtual impedance increases. The proposed VI control provides an effective solution for oscillation suppression in application of multi-port converter.

CHAPTER 7. SUMMARY

This thesis proposes a multi-port converter-based DC traction power system to integrate renewable energy sources, DC traction power systems and other DC microgrids such as hydrogen stations. The operation, stability and active damping methods are investigated in this thesis.

In Chapter 2, a dual active bridge converter is adopted as an interlinking converter to connect with RESs and DCTPS. The operation strategies are proposed considering the intermittent feature of RESs and the RB energy from DCTPS. Then, the operation strategies are further developed for multi-port converter-based DCTPS in Chapter 3, where TAB converter is utilized to be the interlinking converter to connect with RESs, DCTPS sand hydrogen stations.

In Chapter 4, the stability of TAB converter-based DCTPS is investigated. The unterminated output impedance is calculated by the extra element theorem. The process using EET make the context more intuitive and concise. The DCTPS and hydrogen station are regarded as two CPLs. The systems exhibit the potential oscillation issue when the TAB converter supports two CPLs.

In Chapter 5, the stability of TAB converter connecting one CPL is investigated. Two situations are presented. One situation is that a resistor is connected to the port3. Another situation is that a battery is connected to the port3. The oscillation issue can be solved by changing the operation state of port3.

In Chapter 6, a virtual impedance control is presented to solve the instability issue which is discussed in Chapter 4. The VI control has four different plans corresponding to four different positions of virtual impedance. All of them can effectively reshape the output impedance to suppress the oscillation. The simulation and experiment test validate the effectiveness of VI control.

In summary, this thesis mainly presents a method based on the extra element theorem to obtain the terminal impedance of TAB converter. The stability of TAB converter with CPL is investigated in depth. Furthermore, a virtual impedance control is proposed to suppress the oscillation of TAB converter with two CPLs. The developed derivation method and control are not just applicable to DCTPS, but also to other multiple DC systems. It is also applicable for multi-port converters with more than three ports.

LITERATURE LIST

[1] Installed solar energy capacity-Cumulative installed solar capacity, measured in gigawatts (GW). https://ourworldindata.org/grapher/installed-solar-PV-capacity (accessed April 13th, 2023).

[2] Installed wind energy capacity-Cumulative installed wind energy capacity including both onshore and offshore wind sources, measured in gigawatts (GW). https://ourworldindata.org/grapher/cumulative-installed-wind-energy-capacity-gigawatts?country=OWID_WRL~CHN~USA~DNK (accessed April 13th, 2023).

[3] *IEEE Standard for Uncontrolled Traction Power rectifiers for Substation Applications up to 1500V DC Nominal Output*, IEEE Standard 1653.2, 2020.

[4] ABB. ABB traction rectifiers- Diode rectifiers for DC traction substations. https://library.e.abb.com/public/2c94715f41cc5e11c12577a0004872b6/ABB%20traction%20rectifiers_4128PL219-W2-en_09-2010.pdf (accessed April 25th, 2023).

[5] M. Wang, X. Yang, S. Li, M. Ni and T. Q. Zheng, "High Voltage DC Traction Power Supply for Urban Rail Transit," in *Prof. 2021 ITEC*, Chicago, IL, USA, 2021, pp. 893-897.

[6] M. Wang, et al, "A New 24-pluses Rectifier Transformer with Delta-extended Connection," in *Prof. Earth Environ. Sci*., 2019, pp. 1-6.

[7] W. Gunselmann, "Technologies for increased energy efficiency in railway systems," in *Proc. of 2005 European Conference on Power Electronics and Applications*, Dresden, Germany, 2005, pp. 10 pp.-P.10.

[8] X. Yang, X. Li, B. Ning and T. Tang, "A Survey on Energy-Efficient Train Operation for Urban Rail Transit," *IEEE Trans. Intell. Transp. Syst*., vol. 17, no. 1, pp. 2-13, Jan. 2016.

[9] M. Khodaparastan, A. A. Mohamed and W. Brandauer, "Recuperation of Regenerative Braking Energy in Electric Rail Transit Systems," *IEEE Trans. Intell. Transp. Syst*., vol. 20, no. 8, pp. 2831-2847, Aug. 2019.

[10] S. Su, T. Tang and C. Roberts, "A Cooperative Train Control Model for Energy Saving," *IEEE Trans. Intell. Transp. Syst.*, vol. 16, no. 2, pp. 622-631, April 2015.

[11] J. Yin, T. Tang, L. Yang, J. Xun, Y. Huang and Z. Gao, "Research and development of automatic train operation for railway transportation systems: A survey," *Transportation Research Part C*, vol. 85, pp. 548-572, 2017.

[12] Amie Albrecht, Phil Howlett, Peter Pudney, Xuan Vu, Peng Zhou, "The key principles of optimal train control—Part 1: Formulation of the model, strategies of optimal type, evolutionary lines, location of optimal switching points," Transportation Research Part B: Methodological, vol. 94, pp. 482-508, 2016.

[13] S. Lu, S. Hillmansen, T. K. Ho and C. Roberts, "Single-Train Trajectory Optimization," *IEEE Trans. Intell. Transp. Syst.*, vol. 14, no. 2, pp. 743-750, Jun. 2013.

[14] S. Su, X. Wang, Y. Cao and J. Yin, "An Energy-Efficient Train Operation Approach by Integrating the Metro Timetabling and Eco-Driving," *IEEE Trans. Intell. Transp. Syst.*, vol. 21, no. 10, pp. 4252-4268, Oct. 2020.

[15] X. Li and H. K. Lo, "An energy-efficient scheduling and speed control approach for metro rail operations," *Transp. Res. B, Methodol.*, vol. 64, pp. 73–89, Jun. 2014.

[16] S. Su, X. Wang, T. Tang, G. Wang and Y. Cao, "Energy-efficient operation by cooperative control among trains: A multi-agent reinforcement learning approach," *Control Engineering Practice*, Vol. 116, pp. 1-16, Nov. 2021.

[17] H. Ibaiondo and A. Romo, "Kinetic energy recovery on railway systems with feedback to the grid," in *Proc. 14th Int. Power Electron. Motion Control Conf. (EPE-PEMC)*, Sep. 2010, pp. 94–97.

[18] S. Lin et al., "Research on the Regeneration Braking Energy Feedback System of Urban Rail Transit," *IEEE Trans. Veh. Technol*., vol. 68, no. 8, pp. 7329-7339, Aug. 2019.

[19] A. Bitoleanu, M. Popescu and V. Suru, "Optimal controllers design in indirect current control system of active DC-Traction substation," in *Proc. PEMC*, Varna, Bulgaria, 2016, pp. 912-917.

[20] A. Gómez-Expósito, J. M. Mauricio, and J. M. Maza-Ortega, "VSC-Based MVDC Railway Electrification System," *IEEE Trans. Power Del..*, vol. 29, no. 1, pp. 422-431, Feb. 2014.

[21] X. Yang, H. Hu, Y. Ge, S. Aatif, Z. He, and S. Gao, "An Improved Droop Control Strategy for VSC-Based MVDC Traction Power Supply System," *IEEE Trans. Ind. Appl.*, vol. 54, no. 5, pp. 5173-5186, Sep.-Oct. 2018.

[22] X. Zhu, H. Hu, H. Tao, and Z. He, "Stability Analysis of PV Plant-Tied MVdc Railway Electrification System," *IEEE Trans. Transp. Electrific.*, vol. 5, no. 1, pp. 311-323, Mar. 2019.

[23] T. Liang and V. Dinavahi, "Real-Time Device-Level Simulation of MMC-Based MVDC Traction Power System on MPSoC," *IEEE Trans. Transp. Electrific.*, vol. 4, no. 2, pp. 626-641, June 2018.

[24] H. J. Ahmad and M. Hagiwara, "A Compact High-Power Noninverting Bidirectional Buck–Boost Chopper for Onboard Battery Energy Storage Systems," *IEEE Trans. Power Electron*., vol. 37, no. 2, pp. 1722-1735, Feb. 2022.

[25] M. A. Khan, A. Ahmed, I. Husain, Y. Sozer and M. Badawy, "Performance Analysis of Bidirectional DC–DC Converters for Electric Vehicles," *IEEE Trans. Ind. Appl.*, vol. 51, no. 4, pp. 3442-3452, July-Aug. 2015.

[26] Q. Tian, G. Zeng, W. Xu, Z. Huang and D. Ma, "Design of a Bi-directional DC-DC Converter for High-efficiency Emergency Self-traction of High-speed Railway Trains," in *Proc. SPIES*, Beijing, China, 2022, pp. 281-286.

[27] Xin Wang, Yingbing Luo, Bin Qin, Lingzhong Guo, "Power dynamic allocation strategy for urban rail hybrid energy storage system based on iterative learning control," *Energy*, vol. 245, pp. 1-12, Apr. 2022.

[28] L. S. Ashkezari, H. J. Kaleybar, M. Brenna and D. Zaninelli, “E-bus Opportunity Charging System Supplied by Tramway Line: A Real Case Study,” in *Proc. 2022 EEEIC/I&CPS Europe*, Prague, Czech Republic, 2022, pp. 1-6.

[29] N. Parida, C. -K. Cheung and Z. Gao, “Silicon Carbide based Bidirectional CLLC Converter for Modularized Metro Energy Storage Systems,” in *Proc. 2022 ICEPT*, Dalian, China, 2022, pp. 1-6.

[30] Z. Zhu, F. Xiao, Z. Huang, J. Liu, P. Chen and Q. Ren, “Bidirectional Power Control Strategy for Super Capacitor Energy Storage System Based on MMC DC-DC Converter,” *IEEE Access*, vol. 10, pp. 53225-53233, 2022.

[31] C. Wu, W. Zhang, S. Lu, Z. Tan, F. Xue and J. Yang, “Train Speed Trajectory Optimization With On-Board Energy Storage Device,” *IEEE Trans. Intell. Transp. Syst.*, vol. 20, no. 11, pp. 4092-4102, Nov. 2019.

[32] Y. Huang, L. Yang, T. Tang, Z.. Gao, F. Cao, K. Li, “Train speed profile optimization with on-board energy storage devices: A dynamic programming based approach,” *Computers & Industrial Engineering*, vol. 126, pp. 149-164, Oct. 2018.

[33] B. Zhang, C. Wu, G. Meng, F. Xue and S. Lu, “Optimal Sizing of Onboard Hybrid Energy Storage Devices Considering the Long-Term Train Operation,” *IEEE Access*, vol. 10, pp. 58360-58374, 2022.

[34] C. Wu, S. Lu, F. Xue, L. Jiang and M. Chen, “Optimal Sizing of Onboard Energy Storage Devices for Electrified Railway Systems,” *IEEE Trans. Transp. Electrific.*, vol. 6, no. 3, pp. 1301-1311, Sept. 2020.

[35] J. Mi, Z. Yang, Z. Zhong, F. Lin, C. Diao and T. You, “Optimal Sizing of On-board and Wayside Energy Storage Systems for Braking Energy Recovery,” *in Proc. 2022 ITEC Asia-Pacific*, Haining, China, 2022, pp. 1-6.

[36] D. Ramsey, T. Letrouve, A. Bouscayrol and P. Delarue, “Comparison of Energy Recovery Solutions on a Suburban DC Railway System,” *IEEE Trans. Transp. Electrific.*, vol. 7, no. 3, pp. 1849-1857, Sept. 2021.

[37] S. Yang, Y. Chen, Z. Dong, J. Wu, “A collaborative operation mode of energy storage system and train operation system in power supply network,” *Energy*, vol. 276, pp. 1-11, Aug. 2023.

[38] F. Zhu, Z. Yang, F. Lin and Y. Xin, “Decentralized Cooperative Control of Multiple Energy Storage Systems in Urban Railway Based on Multiagent Deep Reinforcement Learning,” *IEEE Trans. Power Electron*., vol. 35, no. 9, pp. 9368-9379, Sept. 2020.

[39] H. Hayashiya et al., “Potentials, peculiarities and prospects of solar power generation on the railway premises,” in *Proc. 2012 ICRERA*, Nagasaki, Japan, 2012, pp. 1-6.

[40] T. Miyagawa et al., “Cooperative control of reactive power of distributed PV systems to suppress voltage of distribution line along railroad track,” in *Proc. 2015 ECCE-Europe*, Geneva, Switzerland, 2015, pp. 1-7.

[41] 2022 Social Responsibility Report of Shenzhen metro company. https://www.szmc.net/SMARTC/upload/file/20230629/1688009723575072978.pdf (accessed August 17th, 2023).

[42] X. Shen, H. Wei, L. Wei, "Study of trackside photovoltaic power integration into the traction power system of suburban elevated urban rail transit line," *Applied Energy*, vol. 260, pp.1-9, Feb. 2020.

[43] S. Siad, G. Damm, L. G. Dol and A. d. Bernardinis, "Design and Control of a DC Grid for Railway Stations," in *Proc. PCIM Europe 2017*, Nuremberg, Germany, 2017, pp. 1-8.

[44] F. Perez, A. Iovine, G. Damm, L. Galai-Dol and P. F. Ribeiro, "Stability Analysis of a DC MicroGrid for a Smart Railway Station Integrating Renewable Sources," *IEEE Trans. on Control Syst. Technol.*, vol. 28, no. 5, pp. 1802-1816, Sept. 2020.

[45] Zhang G, Tian Z, Du H, Liu Z. "A Novel Hybrid DC Traction Power Supply System Integrating PV and Reversible Converters," *Energies*, vol. 11, no. 7, pp. 1-24, Jun. 2018.

[46] A. M. Gee and R. W. Dunn, "Analysis of Trackside Flywheel Energy Storage in Light Rail Systems," *IEEE Trans. Veh. Technol*, vol. 64, no. 9, pp. 3858-3869, Sept. 2015.

[47] H. J. Kaleybar, M. Brenna, F. Castelli-Dezza and D. Zaninelli, "Sustainable MVDC Railway System Integrated with Renewable Energy Sources and EV Charging Station," in *Proc. VPPC*, Merced, CA, USA, 2022, pp. 1-6.

[48] S. Nasr, M. Iordache and M. Petit, "Smart micro-grid integration in DC railway systems," in *Proc. IEEE PES Innovative Smart Grid Technologies*, Europe, Istanbul, Turkey, 2014, pp. 1-6.

[49] K. G. Logan, J. D. Nelson, B. C. McLellan, A. Hastings, "Electric and hydrogen rail: Potential contribution to net zero in the UK," *Transportation Research Part D: Transport and Environment*, vol. 87, pp. 1-16, Oct. 2020.

[50] Z. Xu, N. Zhao, S. Hillmansen, C. Roberts, and Y. Yan, "Techno-Economic Analysis of Hydrogen Storage Technologies for Railway Engineering: A Review," *Energies*, vol. 15, no. 17, pp. 1-22, Sept. 2022.

[51] G. D'Ovidio, A. Ometto, and O. Valentini, "A novel predictive power flow control strategy for hydrogen city rail train," *Int. J. Hydrogen Energy*, vol. 45, no. 7, pp. 4922-4931, Feb. 2020.

[52] Y. Yan, Q. Li, W. Huang and W. Chen, "Operation Optimization and Control Method Based on Optimal Energy and Hydrogen Consumption for the Fuel Cell/Supercapacitor Hybrid Tram," *IEEE Trans. Ind. Electron.*, vol. 68, no. 2, pp. 1342-1352, Feb. 2021.

[53] Y. Yan, Q. Li, W. Chen, B. Su, J. Liu and L. Ma, "Optimal Energy Management and Control in Multimode Equivalent Energy Consumption of Fuel Cell/Supercapacitor of Hybrid Electric Tram," IEEE Trans. Ind. Electron., vol. 66, no. 8, pp. 6065-6076, Aug. 2019.

[54] Q. Li, T. Wang, C. Dai, W. Chen and L. Ma, "Power Management Strategy Based on Adaptive Droop Control for a Fuel Cell-Battery-Supercapacitor

Hybrid Tramway," *IEEE Trans. Veh. Technol.*, vol. 67, no. 7, pp. 5658-5670, July 2018.

[55] F. Piraino, M. Genovese, P. Fragiacomo, "Towards a new mobility concept for regional trains and hydrogen infrastructure," *Energy Convers. Manage*., vol. 228, pp.113650, Jan. 2021

[56] Carlos Fúnez Guerra, et al., "Sustainability of hydrogen refuelling stations for trains using electrolysers," *Int. J. Hydrogen Energy*, early access, Oct. 2020, doi: 10.1016/j.ijhydene.2020.10.044.

[57] F. P. Wijaya, H. Kobayashi, K. Kondo, T. Iwasaki and A. Tsumura, "Damping control method of regenerative brake control under light load condition utilizing over voltage resistor," in *Proc. PEDS*, Honolulu, HI, USA, 2017, pp. 1,194-1,199.

[58] F. Yusivar, K. Uchida, T. Kihara, S. Wakao, K. Kondo and K. Matsuoka, "An anti oscillation strategy for the regenerative braking control of permanent magnet synchronous motor with insufficient load power consumption," in *Proc. 27th IECON*, Denver, CO, USA, 2001, pp. 1457-1462 vol. 2.

[59] V. M. Iyer, S. Gulur and S. Bhattacharya, "Small-Signal Stability Assessment and Active Stabilization of a Bidirectional Battery Charger," *IEEE Trans. Ind. Appli*., vol. 55, no. 1, pp. 563-574, Jan.-Feb. 2019.

[60] F. Feng, X. Zhang, J. Zhang and H. B. Gooi, "Stability Enhancement via Controller Optimization and Impedance Shaping for Dual Active Bridge-Based Energy Storage Systems," *IEEE Trans. Ind. Electron*., vol. 68, no. 7, pp. 5863-5874, July 2021.

[61] Y. Guan, Y. Xie, Y. Wang, Y. Liang, and X. Wang, "An Active Damping Strategy for Input Impedance of Bidirectional Dual Active Bridge DC–DC Converter: Modeling, Shaping, Design, and Experiment," *IEEE Trans. Ind. Electron*., vol. 68, no. 2, pp. 1263-1274, Feb. 2021.

[62] P. Pan et al., "An Impedance-Based Stability Assessment Methodology for DC Distribution Power System With Multivoltage Levels," *IEEE Trans. Power Electron*., vol. 35, no. 4, pp. 4033-4047, Apr. 2020.

[63] H. Mu et al., "Impedance-Based Stability Analysis Methods for DC Distribution Power System With Multivoltage Levels," *IEEE Trans. Power Electron*., vol. 36, no. 8, pp. 9193-9208, Aug. 2021.

[64] M. Leng, G. Zhou, H. Li, G. Xu, F. Blaabjerg and T. Dragičević, "Impedance-Based Stability Evaluation for Multibus DC Microgrid Without Constraints on Subsystems," *IEEE Trans. Power Electron*., vol. 37, no. 1, pp. 932-943, Jan. 2022.

[65] Robert W. Erickson, Dragan Maksimovic, *Fundamentals of Power electronics*, 3rd ed. Springer, 2020.

[66] J. A. Mueller and J. W. Kimball, "Model-based Determination of Closed-loop Input Impedance for Dual Active Bridge Converters," in *Proc. 2017 APEC*, Tampa, USA, 2017, pp. 1039-1046.

[67] Q. Ye, R. Mo, and H. Li, "Impedance Modeling and DC Bus Voltage Stability Assessment of a Solid-State-Transformer-Enabled Hybrid AC–DC

Grid Considering Bidirectional Power Flow," *IEEE Trans. Ind. Electron.*, vol. 67, no. 8, pp. 6531-6540, Aug. 2020.

[68] P. Purgat, S. Bandyopadhyay, Z. Qin and P. Bauer, "Continuous Full Order Model of Triple Active Bridge Converter," in *Proc.* 2019 ECCE Europe, Genova, Italy, 2019, pp. P.1-P.9.

[69] J. Yang, G. Buticchi, C. Gu, S. Günter, H. Yan and P. Wheeler, "Transfer Function Based Input Impedance Determination of Triple Active Bridge Converter," in *Proc.* 2019 IECON, Lisbon, Portugal, 2019, pp. 4917-4923.

[70] J. Yang, G. Buticchi, C. Gu, S. Günter, H. Zhang, and P. Wheeler, "A Generalized Input Impedance Model of Multiple Active Bridge Converter," *IEEE Trans. Transport. Electrific*., vol. 6, no. 4, pp. 1695-1706, Dec. 2020.

[71] I. Cvetkovic, D. Boroyevich, P. Mattavelli, F. C. Lee and D. Dong, "Unterminated Small-Signal Behavioral Model of DC–DC Converters," *IEEE Trans. Power Electron*., vol. 28, no. 4, pp. 1870-1879, April 2013,

[72] X. Zhang, X. Ruan and Q. -C. Zhong, "Improving the Stability of Cascaded DC/DC Converter Systems via Shaping the Input Impedance of the Load Converter With a Parallel or Series Virtual Impedance," *IEEE Trans. Ind. Electron.*, vol. 62, no. 12, pp. 7499-7512, Dec. 2015.

[73] X. Zhang, Q. -C. Zhong and W. -L. Ming, "Stabilization of Cascaded DC/DC Converters via Adaptive Series-Virtual-Impedance Control of the Load Converter," *IEEE Trans. Power Electron.*, vol. 31, no. 9, pp. 6057-6063, Sept. 2016.

[74] X. Zhang, Q. -C. Zhong and W. -L. Ming, "Stabilization of a Cascaded DC Converter System via Adding a Virtual Adaptive Parallel Impedance to the Input of the Load Converter," *IEEE Trans. Power Electron.*, vol. 31, no. 3, pp. 1826-1832, March 2016.

[75] B. He, W. Chen, X. Li, L. Shu and X. Ruan, "A Power Adaptive Impedance Reshaping Strategy for Cascaded DC System With Buck-Type Constant Power Load," *IEEE Trans. Power Electron.*, vol. 37, no. 8, pp. 8909-8920, Aug. 2022.

[76] Z. Shan, S. Fan, X. Liu, X. Ding and Z. Li, "Transient Mitigation Using an Auxiliary Circuit in Cascaded DC–DC Converter Systems With Virtual Impedance Control.

[77] F. Gao, S. Bozhko, A. Costabeber, G. Asher and P. Wheeler, "Control Design and Voltage Stability Analysis of a Droop-Controlled Electrical Power System for More Electric Aircraft," *IEEE Trans. Ind. Electron.*, vol. 64, no. 12, pp. 9271-9281, Dec. 2017.

[78] F. Gao et al., "Comparative Stability Analysis of Droop Control Approaches in Voltage-Source-Converter-Based DC Microgrids," *IEEE Trans. Power Electron.*, vol. 32, no. 3, pp. 2395-2415, March 2017.

[79] X. Zhang, Q. -C. Zhong, V. Kadirkamanathan, J. He and J. Huang, "Source-Side Series-Virtual-Impedance Control to Improve the Cascaded System Stability and the Dynamic Performance of Its Source Converter," *IEEE Trans. Power Electron.*, vol. 34, no. 6, pp. 5854-5866, June 2019.

[80] O. Lorzadeh, I. Lorzadeh, M. N. Soltani and A. Hajizadeh, "Source-Side Virtual RC Damper-Based Stabilization Technique for Cascaded Systems in DC Microgrids," *IEEE Trans. Energy Convers.*, vol. 36, no. 3, pp. 1883-1895, Sept. 2021.

[81] Q. Ye, R. Mo and H. Li, "Low-Frequency Resonance Suppression of a Dual-Active-Bridge DC/DC converter Enabled DC Microgrid," *IEEE J. Emerg. Sel. Topics Power Electron*., vol. 5, no. 3, pp. 982-994, Sept. 2017.

[82] Q. Ye, R. Mo and H. Li, "Stability analysis and improvement of a dual active bridge (DAB) converter enabled DC microgrid based on a reduced-order low frequency model," in *Proc. ECCE*, Milwaukee, WI, USA, 2016, pp. 1-7.

[83] IEEE Standard for Electrical and Electronic Control Apparatus on Rail Vehicles, *IEEE Standard 16-2020*, Apr.2020.

[84] Railway Applications—Supply Voltages of Traction System, IEC Standard 60850:2014, Nov. 2014.

[85] T. Dragičević, J. M. Guerrero, J. C. Vasquez and D. Škrlec, "Supervisory Control of an Adaptive-Droop Regulated DC Microgrid With Battery Management Capability," *IEEE Trans Power Electron*., vol. 29, no. 2, pp. 695-706, Feb. 2014.

[86] J. M. Guerrero, J. C. Vasquez, J. Matas, L. G. de Vicuna and M. Castilla, "Hierarchical Control of Droop-Controlled AC and DC Microgrids—A General Approach Toward Standardization," *IEEE Trans. Ind. Electron*., vol. 58, no. 1, pp. 158-172, Jan. 2011.

[87] H. Qin and J. W. Kimball, "Generalized Average Modeling of Dual Active Bridge DC–DC Converter," *IEEE Trans. Power Electron*., vol. 27, no. 4, pp. 2078-2084, April 2012.

[88] F. Krismer and J. W. Kolar, "Accurate Small-Signal Model for the Digital Control of an Automotive Bidirectional Dual Active Bridge," *IEEE Trans. Power Electron*., vol. 24, no. 12, pp. 2756-2768, Dec. 2009.

[89] K. Zhang, Z. Shan and J. Jatskevich, "Large- and Small-Signal Average-Value Modeling of Dual-Active-Bridge DC–DC Converter Considering Power Losses," *IEEE Trans. Power Electron*., vol. 32, no. 3, pp. 1964-1974, March 2017.

[90] J. Guacaneme, G. Garcerá, E. Figueres, I. Patrao, R. González-Medina, "Dynamic modeling of a dual active bridge DC to DC converter with average current control and load-current feed-forward," *Int. J. Circuit Theory Application*, vol. 43, no. 10, pp. 1311-1332.

[91] X. Li et al., "Flexible Interlinking and Coordinated Power Control of Multiple DC Microgrids Clusters," *IEEE Trans. Sustain. Energy*, vol. 9, no. 2, pp. 904-915, Apr. 2018.

[92] Z. Yang, Z. Yang, F. Lin, and H. Xia, "Improved Control Strategy of Energy Storage System Considering Train Operation States," in *Proc. 2017 IEEE 20th Int. Conf. Intell. Transp. Syst. (ITSC)*, Mar. 2018, pp. 1-6.

[93] M.Y. El-Sharkh er al, "A dynamic model for a stand-alone PEM fuel cell power plant for residential applications," *J. Power Source*, vol. 138, no. 1–2, pp. 199-204, 2004.

[94] R. K. Sharma and S. Mishra, "Dynamic Power Management and Control of a PV PEM Fuel-Cell-Based Standalone ac/dc Microgrid Using Hybrid Energy Storage," *IEEE Trans. Ind. Appl.*, vol. 54, no. 1, pp. 526-538, Jan.-Feb. 2018.

[95] A. Beainy, N. Karami and N. Moubayed, "Simulink model for a PEM electrolyzer based on an equivalent electrical circuit," *International Conference on Renewable Energies for Developing Countries 2014*, 2014, pp. 145-149.

[96] Byungcho Choi, *Pulsewidth Modulated DC-to-DC Power Conversion-Circuits, Dynamics, Control, and DC Power Distribution Systems*, 2nd ed. Wiley, 2021.

[97] Ozcan Atlam, and Mohan Kolhe, "Equivalent Electrical Model for a Proton Exchange Membrane (PEM) Electrolyser," *Energy Convers. Manage.*, vol. 52, no. 8-9, pp. 2952-2957, 2011.

[98] S. Falcones, R. Ayyanar, and X. Mao, "A DC–DC Multi-port-Converter-Based Solid-State Transformer Integrating Distributed Generation and Storage," *IEEE Trans. Power Electron*., vol. 28, no. 5, pp. 2192-2203, May 2013.

[99] C. Zhao, S. D. Round, and J. W. Kolar, "An Isolated Three-Port Bidirectional DC-DC Converter With Decoupled Power Flow Management," *IEEE Trans. Power Electron*., vol. 23, no. 5, pp. 2443-2453, Sept. 2008.

APPENDICES

The coefficient of (4.12) in Chapter 4 is given in Table A.I as follows.

Table A.I The coefficients of the small signal model of TAB converter

$$G_{11}=\frac{n_1\overline{V}_2}{2n_2f_sL_{12}}\left(1-2\left|\overline{d}_{12}\right|\right),G_{12}=\frac{n_1\overline{d}_{12}}{2n_2f_sL_{12}}\left(1-\left|\overline{d}_{12}\right|\right)$$

$$G_{13}=\frac{n_1\overline{V}_3}{2n_3f_sL_{13}}\left(1-2\left|\overline{d}_{13}\right|\right),G_{14}=\frac{n_1\overline{d}_{13}}{2n_3f_sL_{13}}\left(1-\left|\overline{d}_{13}\right|\right)$$

$$G_{22}=\frac{n_1\overline{d}_{12}}{2n_2f_sL_{12}}\left(1-\left|\overline{d}_{12}\right|\right),G_{23}=-\frac{n_1^2\overline{V}_3}{2n_2n_3f_sL_{23}}\left(1-2\left|\overline{d}_{13}-\overline{d}_{12}\right|\right)$$

$$G_{24}=-\frac{n_1^2\left(\overline{d}_{13}-\overline{d}_{12}\right)}{2n_2n_3f_sL_{23}}\left(1-\left|\overline{d}_{13}-\overline{d}_{12}\right|\right),G_{31}=-\frac{n_1^2\overline{V}_1}{2n_2n_3f_sL_{23}}\left(1-2\left|\overline{d}_{13}-\overline{d}_{12}\right|\right)$$

$$G_{32}=\frac{n_1\overline{d}_{13}}{2n_3f_sL_{13}}\left(1-\left|\overline{d}_{13}\right|\right),G_{34}=\frac{n_1^2\left(\overline{d}_{13}-\overline{d}_{12}\right)}{2n_2n_3f_sL_{23}}\left(1-\left|\overline{d}_{13}-\overline{d}_{12}\right|\right)$$

$$G_{21}=\frac{n_1\overline{V}_1}{2n_2f_sL_{12}}\left(1-2\left|\overline{d}_{12}\right|\right)+\frac{n_1^2\overline{V}_3}{2n_2n_3f_sL_{23}}\left(1-2\left|\overline{d}_{13}-\overline{d}_{12}\right|\right)$$

$$G_{33}=\frac{n_1\overline{V}_1}{2n_3f_sL_{13}}\left(1-2\left|\overline{d}_{13}\right|\right)+\frac{n_1^2\overline{V}_2}{2n_2n_3f_sL_{23}}\left(1-2\left|\overline{d}_{13}-\overline{d}_{12}\right|\right)$$

Part II. Selected Publications

Journal Publication 1

A Novel Renewable Microgrid-Enabled Metro Traction Power System-Concepts, Framework and Operation Strategy [J1]

Haoyuan Yu, Yanbo Wang, Zhe Chen

This paper is published in IEEE Transactions on Transportation Electrification

The layout has been revised.

Journal Publication 2

Impedance Modeling and Stability Analysis of Triple-Active-Bridge-Converter-Based Renewable-Electricity-Hydrogen-Integrated Metro DC Traction Power System [J2]

Haoyuan Yu, Yanbo Wang, Hanwen Zhang, Zhe Chen

This paper is published in IEEE Transactions on Industrial Electronics

The layout has been revised.

Journal Publication 3

A Virtual Impedance-based Active Damping Control Strategy for Triple Active Bridge Converter [J3]

Haoyuan Yu, Hanwen Zhang, Qi Zhang, Yanbo Wang, Zian Qin, Zhe Chen, Pavol Bauer

This paper is submitted to IEEE Transactions on Industrial Electronics

The layout has been revised.

Conference Publication 1

A Novel DC Microgrid-enabled Metro Traction Power System [C1]

Haoyuan Yu, Yanbo Wang, Zhe Chen

This paper is published in 2020 IEEE 11th International Symposium on Power Electronics for Distributed Generation Systems (PEDG), 2020, pp. 322-327.

The layout has been revised.

Conference Publication 2

A Renewable Electricity-Hydrogen-Integrated Hybrid DC Traction Power System [C2]

Haoyuan Yu, Yanbo Wang, Zhe Chen

This paper is published in 2021 IEEE Southern Power Electronics Conference (SPEC), 2021, pp. 1-6.

The layout has been revised.

Conference Publication 3

Stability Analysis of Triple Active Bridge Converter with Hybrid Loads and Different Control Strategies [C3]

Haoyuan Yu, Hanwen Zhang, Yanbo Wang, Zian Qin, Zhe Chen, Pavol Bauer

This paper is published in 2023 IEEE 14th International Symposium on Power Electronics for Distributed Generation Systems (PEDG), 2023, pp. 223-228.

The layout has been revised.

ISSN (online): 2446-1636
ISBN (online): 978-87-7573-579-2

AALBORG UNIVERSITY PRESS